2019

Numerical Investigation and Optimization of Pin Fins in Micro Heat Sinks

Fuad Ismayilov
University of Central Florida

INVESTIGATION OF NOVEL FIN STRUCTURES ENHANCING MICRO HEAT SINK THERMAL PERFORMANCE

by

FUAD ISMAYILOV

M.Sc., University of Central Florida, 2013

A dissertation submitted in partial fulfillment of the requirements

for the degree of Doctor of Philosophy

in the Department of Mechanical and Aerospace Engineering

in the College of Engineering and Computer Science

at the University of Central Florida

Orlando, Florida

Fall Term

2019

Major Professor: Yoav Peles

ABSTRACT

Operating temperature in electronics applications is continuously increasing. Therefore, for the past few decades, high heat flux removing micro heat sinks are investigated in terms of heat transfer effectiveness. This study generally concentrates on improving the passive heat transfer techniques. Micro heat sinks used in experiments are fabricated using *MEMS* techniques. Resistance temperature detectors, RTDs, were used for temperature measurements. The experimental data was obtained for single and two phase flow regions; however, only single phase flow results were considered in numerical simulations. Numerical validations were performed on the micro heat sinks, including cylinder and hydrofoil shaped pin fins. Following the validation phase, optimization has been performed to further improve the hydraulic and thermal performance. DOE study showed that the chord length and leading edge size of the hydrofoil pin fin are significant contributors to the thermal performance. The ranges of geometrical variables were identified and fed into multi-objective optimization cycles implementing the multi-objective genetic algorithm. The optimization objectives were to minimize pumping requirements while enhancing the local and global heat transfer effectiveness over the surface of the heater in single phase flow environment. A broad range of geometries were obtained with an acceptable tradeoff between thermal and hydraulic performance for low Reynolds number. Additionally, tandem geometries were investigated and showed that higher heat transfer effectiveness could be obtained with acceptable pumping power requirements. The importance of such optimization studies before the experimental testing is highlighted, and novel geometries are presented for further experimental investigations. Thermal performance improvement of 28% was obtained via implementing proposed geometries with only a 12% pressure drop increase. Local heat transfer optimization, aiming to decrease the local temperatures were also performed using doublet

pin fin configurations. Results showed that tandem hydrofoils could control the flow with minimum pressure drops while reaching the desired low local temperatures.

ACKNOWLEDGMENTS

This effort is dedicated to my beloved father and mother, Faiq Ismayilov and Zarqalam Ismayilova.

First and foremost, I would like express my deepest gratitude to my advisor Dr.Yoav Peles, for his continued support, trust, patience and enthusiasm that he showed throughout my PhD studies. It would be impossible to finish this research study without his enlightening wisdom and encouraging mentorship.

I would like to thank Dr. Ali Akturk, member of my doctoral committee, for his guidance and great contribution to my studies. His insights were very essential in performing numerical studies.

I appreciate the support I have received from my labmates at Multiphase Heat Transfer Laboratory. I would like to specifically mention Dr.Yingying Wang, from whom I learned a lot of experimental skills. Micro devices studied in this research are resultant of her excellent micro fabrication skills.

This work was funded by the Office of Naval Research (ONR) with Dr. Mark Spector as program manager (Grant #N00014-15-1-2071). I would like to acknowledge the Cornell NanoScale Science & Technology Facility (CNF) for staff support.

TABLE OF CONTENTS

LIST OF FIGURES

LIST OF TABLES

NOMENCLATURE

A	area, m^2, *unless otherwise specified*
a	face area vector, *unless otherwise specified*
Cμ	momentum coefficient
c	specific heat, J/kg/K
D	diameter, μm
E	total energy, J
En	enhancement factor
FFT	Fast Fourier Transform
f	body forces, N
H	total enthalpy, J/kg
h	heat transfer coefficient, W/m2 /K
$h_{average}$	average heat transfer coefficient over the heater area, W/m2 /K
I	identity matrix
Nu	Nusselt number
p	pressure, Pa
q”	heat flux, W/m2
R	viscous stress tensor
Re	Reynolds number based on the channel hydraulic diameter
Re_D	Reynolds number based on diameter of the cylinder
St	Strouhal number
s	source term
T	Temperature, K or 0C
V	volume, m3
RTD	Resistance Temperature Detector

Greek symbols

ρ	mass density (kg/m3)
v	velocity magnitude in y direction (m/s)

Subscripts

c	cross section
h	hydraulic
j	jet ratio
o	base case when there is no jet
p	constant pressure
s	surface
∞	free stream

CHAPTER 1. INTRODUCTION

1.1. Literature Review

A very large scale integration (VLSI) process combines thousands of transistors on a single chip. This process's roots link to semiconductor and communication technologies. For instance, microprocessors are developed via the VLSI process. Transistors are one of the essential components on the integrated chips and on are usually used for general switching, logic gates, radio transmission, signal processing, amplification, and sound reproduction. The number of transistors on the integrated chip increases with the increased complexity level of the duties. Back in the 1970s, Gordon Moore predicted based on his observations that the transistor number on a dense integrated circuit is doubled every two years, as seen in Figure 1. Moore's prediction, known as Moore's law, has been proved to be accurate by the semiconductor industry practices.

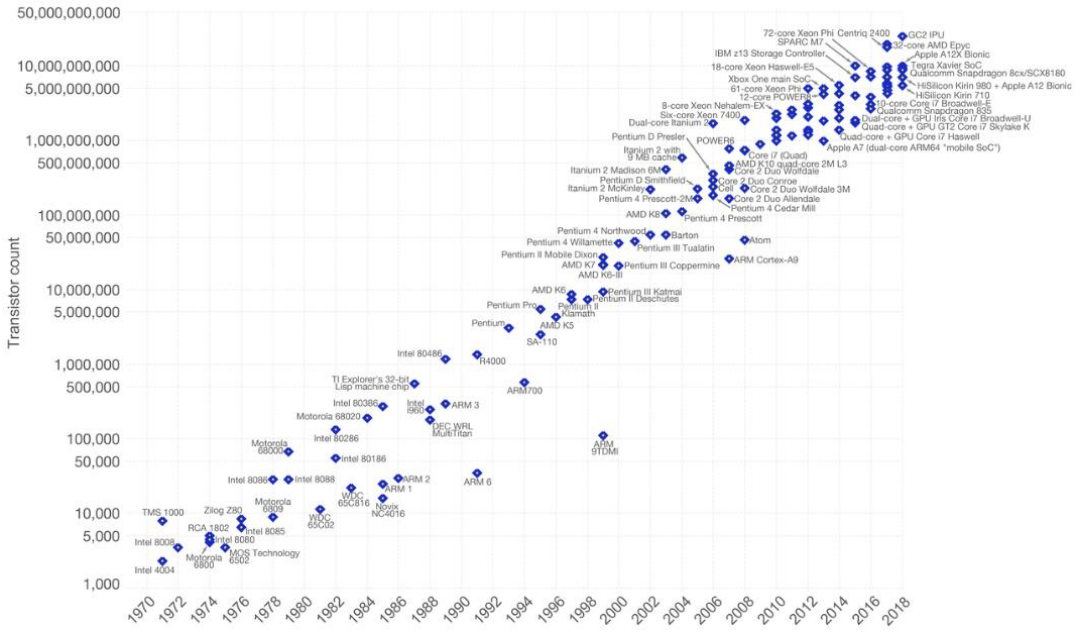

Figure 1 Representation of Moore's Law. (www.intel.com)

Transistors have ON and OFF states. It has to be noted that the transistor does not switch from ON to OFF state instantly. There is a period between these states where transistor acts as a resistor. Moreover, the transistor will still possess resistance during the ON state. The current passing through the transistor is leading to heat generation, which is explained with $P = I2R$ (1. As a result, increased transistor number creates more heat generation in the integrated chip circuit.

$$P = I^2R \tag{1}$$

Removing heat from the integrated circuits for efficient and durable operation is continuing to be one of the main challenges in the heat transfer and fluid mechanics arena. An in-depth literature review, which is elaborated in proceeding sections, reveals that the future generation ICs are expected to produce more than 1000 W/cm^2 heat. As a remedy, micro heat sinks revolutionized the electronic cooling research arena and became one of the most viable solutions for the industry.

Having a high surface to volume ratio, micro heat sinks allow for the desired heat transfer to take place. However, low volume flow passages suppress the natural flow instabilities and limit the flow to stay

laminar region. To overcome this limitation and create more flow mixing, active and passive heat transfer enhancement techniques were broadly investigated since the 1980s. Generally, passive methods include blunt-body structures embedded inside the microchannels obstructing the flow and creating flow mixing, whereas active techniques implement direct control of the flow instabilities such as jets introduced in the crossflow.

The main aim of the current study is to extend fundamental knowledge on the passive heat transfer techniques via investigating the effect of hydrofoil and piranha pin-fin shaped geometries on the micro heat sink/heat exchanger performance. Efforts will be concentrated on the experimental measurements and corresponding numerical modeling techniques, mitigating the challenges faced due to experimental setup limitations. Flow paths and patterns over the geometries mentioned above will be studied in a broad manner using numerical models verified with the experimental data. Multi-objective optimization of micro pin-fin arrays to provide maximum possible local and average heat transfer coefficient will be performed.

1.1.1. Advancements in micro heat sinks

Micro heat sinks were introduced to the electronics cooling area via a pioneering study done by Tuckerman and Pease [1] in 1981. The optimum compact water-cooled micro heat sink was designed with a depth of 365 μm. The cooling channels were 57 μm wide, as shown in Figure 2. The micro heat sink was intended to be integrated on the backside of the integrated circuit chip. As a result of the experiments, up to 790 W/cm^2 heat removal was achieved. Implemented micro heat sink fabrication techniques were another major outcome of this study. A literature review performed by Kandlikar [2] reveals that till 1988's the primary focus concentration of the researchers was attracted to improving and developing the design of microchannels under the light of work done by Tuckerman and Pease [1].

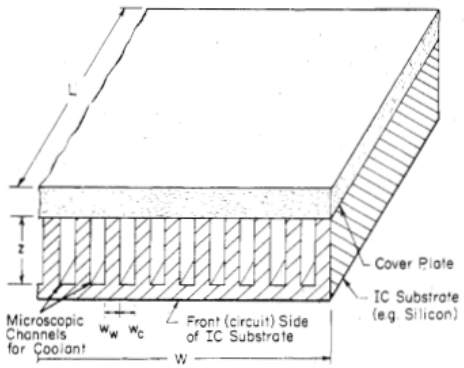

Figure 2 Micro cooling channels implemented in pioneering work [1]

The next big challenge was proving that the conventional continuum theory is applicable in the microchannels and could be used for interpreting the experimental studies. Peng et al. [3,4] conducted fluid flow and heat transfer experiments in 1994, utilizing microchannels having hydraulic diameters ranging from 0.133 to 0.367 mm. The height over the width ratio of the microchannels was kept between 0.333-1 mm. It was shown that the friction factor is proportional to $Re^{-1.98}$ for the laminar flow region, which is clearly different than conventional correlations where proportionality holds against Re. The same behavior was shown for turbulent flows. From a heat transfer perspective, Re and Nu number relationships were holding via distinct coefficients. These results created an urge to re-classify the microchannels based on their geometrical dimensions and to investigate this issue in depth. Mehendale et al. [5] divided heat exchangers into four groups, such as micro, meso, and compact heat exchangers, where hydraulic diameters change 1-100 μm, 100 μm -1 mm,1-6 mm, respectively. The need for clarification and additional data for the single and two-phase data visualization, heat transfer, and fluid flow models and quantification of the rarefaction in micro/meso heat exchangers was appealed.

The studies have shown that the scaling effects such as mismatched entrance boundary conditions, viscous heating, electrical double layer effects, temperature-dependent properties, surface

roughness, and conjugate heat effects lead to discrepancies between the data and conventional Navier-Stokes approach. Kandlikar and Steinke [6] not only showed that the continuum theory is applicable in micro-scale but also analyzed the previously published data in terms of entrance effects, exit losses, and experimental uncertainties. Lee et al. [7] revealed that the mismatch in the boundary conditions has a significant impact on the departure from continuum theory. Hegab et al. [8] also studied fluid flow in microchannels having a hydraulic diameter of 112-210 μm utilizing R134a as a working fluid. The results of the study supported previous studies' observations in terms of the agreement. Additional studies also proved that the continuum theory is applicable in microscale [9-20]. Based on the literature data Nu and Re relationship also follows the conventional correlations [18, 21-22]. However, due to miniature dimensions and limited measurands, numerical modeling was inevitable to prove the Nu and Re relationships, especially locally. The studies related to the applicability of continuum theories and numerical modeling advancements are discussed in depth in section 2.3.

1.1.2. Heat transfer augmentation

As mentioned before, micro heat sinks or heat exchangers are viable solutions for electronic cooling due to the high surface area to volume ratio. It is a well-known fact that the decrease in the hydraulic diameter of these microchannels results in a higher heat transfer coefficient. However, pumping power requirements, pressure drop limitations, and working fluid variations led the researchers to investigate different types of enhancement techniques to optimize the channels for better heat transfer performance. Mainly, forced convection phenomena were implemented, which was observed in terms of single-phase flow and flow boiling.

A lot of effort has been put on the classification of the augmentation techniques in micro heat sinks or heat exchangers. Balaras et al. [22] reported these techniques under four different groups, which are

surface, fluid, combined, and compound augmentation methods. While modified surface structures are included in the surface methods, direct fluid property and flow pattern controlling methods were under fluid methods. The latter two were a combination of the previous two groups. Bergles et al. [23] summarized such techniques into two groups such as passive and active techniques. Passive methods include surface roughness, flow disruptions, channel curvature, re-entrant obstructions, secondary flows, out-of-plane mixing, and fluid additives, whereas vibration, electrostatic fields, and flow pulsation are classified under active techniques. Kandlikar et al. [24] reviewed these methods in-depth in 2004. As mentioned by Tao et al. [25], the main aim should be to create a high-velocity gradient at the heater section, which could be achieved by introducing the flow obstructions to the channel and keep the thermal boundary layer thin or make it re-develop numerous times.

Most of the studies employing micro pin-fins, as a passive heat transfer augmentation approach, has reported promising heat transfer results. Colgan et al. [26] implemented microchannels with fins having a width of 65 to 75 mm and located at a constant pitch of 140 mm. The flow length was limited to 3 mm to achieve a relatively lower pressure drop, less than 35 kPa. Significant heat transfer performance was achieved with a factor of 3. Kandlikar et al. [27] also achieved a high heat transfer coefficient, as much as 500000W/m^{2}K values, via using the same geometrical configuration. Kosar and Peles [28] used micro pin-fin arrays and investigated heat transfer performance. Single-phase fluid flow heat transfer coefficient obtained from the study was comparable to two phase flow counterparts. It has been reported that due to end wall effects, Nu showed different dependence on Re than long tube correlations. Lee et al. [29] developed oblique fins inside the microchannel and experimentally observed fluid flow and heat transfer in the microchannels. As a result of the study, it has been observed that the oblique fins are disturbing the flow, which leads to thermal boundary leading edge to re-develop. Moreover, the secondary flow

between the oblique fins enhanced the mixing, contributing to the increased heat transfer coefficient by 80% relative to the conventional channel. Tsuzuki et al. [30] performed experiments on microchannel having S-shaped pin-fins. Wang et al. [31] conducted experiments with circular, triangular and diamond shape pin-fins where the air was a working medium. Heat transfer coefficient behind the triangular pin-fin wash higher than the circular counterpart. Overall, it was shown that two circular pin-fins in a row shows even better performance than the latter geometries. Recently, Yu and Woodcock et al. [32] proposed piranha pin-fin shape geometries. Significant heat transfer enhancement was achieved in single phase flow.

Vanapalli et al. [33] revealed that the aerodynamic shapes keep the flow unseparated and thus decreasing the thermal resistance at the interface. Kosar and Peles [34] investigated single and two-phase flow heat transfer characteristics in a micro heat sink having hydrofoil shaped pin-fins. The study used NACA 66-021 hydrofoil shape. Overall, there is a lack of single-phase heat transfer studies in terms of microchannels, including solitary aerodynamically and hydrodynamically effective pin-fins, such as hydrofoils and piranha pin fins. Perturbation of the flow by varying the inherent characteristics of the hydrofoil pin-fins such as the angle of attack, chord length, and camber and its effect on the heat transfer is still to be investigated. An in-depth review of previous parametric and optimization studies are presented in section 1.1.4.

The fluid absorbs a considerable amount of heat during the phase change process, which is quantified by the latent heat. This specific capability of fluids is creating a significant advantage in favor of the two-phase flows compared to single phase flows in terms of the heat transfer. Tuckerman and Pease et al. [1] were the first researchers to exploit the effects of flow boiling in the microchannels in 1981. The next study was published in 1992 by Moriyama et al. [35]. Their pressure drop results followed the available

two phase flow correlation. Also, the 3-20 times higher heat transfer coefficient was observed compared to single phase experiments. Expectedly, the heat transfer coefficient increased at the 0 quality point and leveled off in the mid-quality regions. Further increase in the quality resulted in the critical heat flux regime (CHF), and as a result, the heat transfer coefficient decreased. Adiabatic experiments via using steam-water and air-water combinations were conducted by Serizawa et al. [36], and a two-phase flow pattern map, mainly affected by surface roughness, was provided. However, later on, Hestroni et al. [37] showed that adiabatic two-phase flow patterns could not predict the flow boiling patterns due to the absence of bubble growth, rapid oscillations, and nucleation related instabilities.

The main challenge in the flow boiling heat transfer arena is developing the global correlations explaining the phenomena in the microchannels. Even though numerous correlations were developed [38-41] showing that the flow boiling heat transfer coefficient is a function of mass flux, vapor quality, and mass flux, Kandlikar et al. [2] revealed that none of the correlations were able to correlate global experimental data. Researchers linked this issue to the presence of the experimental uncertainties, various wall boundary conditions, different size nucleation sites and unknown severity of instability conditions. For instance, Kosar and Peles [42] implemented inlet restrictors to suppress the flow boiling oscillations. Including artificial nucleation sites and the addition of heated sections to initiate the nucleation are examples of remedies applied by the researchers [43, 44].

Studies applying the heat transfer augmentation techniques in the single phase flow were also extended to flow boiling, expecting even higher heat transfer coefficients [45-49]. Kosar and Peles [34, 50] used NACA 66-021 pin fins and re-entrant cavities to enhance the flow boiling. Woodcock et al. [51] implemented piranha pin shape geometries and studied the flow boiling under two different inlet and outlet configurations at the system level. Overall, the aerodynamically and hydrodynamically effective

pin-fins are not investigated thoroughly in terms of flow boiling phenomena. Implementation of such geometries may help not only further exploit the flow boiling heat transfer but also understand the inherent challenges of the phenomena.

1.1.3. Scaling effects mitigation via numerical modeling

Recent understanding suggests that conjugated conduction/convection effects at the micro-scale are much amplified at the small scale relative to a conventional scale [52-62]. Experimental studies at that scale often assumed a uniform heat flux boundary condition, which is now believed to be a gross oversimplification. A better appreciation of the coupled conduction and convection processes is vital to extend knowledge obtained from experiments. Without such awareness and guidance about practices to infer raw results, such as surface temperature, fundamental knowledge about convective heat transfer in microchannels will be hindered.

Performing experiments in microchannels require addressing multiple issues concurrently, and often only a limited set of variables can be measured. Besides, and as stated by Nakayama et al. [52], the geometric precision and tolerance control in the experimental assembly at the micro-scale can lead to significant uncertainties. Kandlikar et al. [2] mentioned the lack of numerical results in micro-domain, especially for entrance region effects, to be one of the main challenges in the microchannel heat transfer research area. Computational fluid dynamics (CFD) tools are used to supplement experimental studies by providing in-depth information that cannot be measured experimentally, clarifying the aspects mentioned above and uncertainty sources.

Many numerical studies about fluid flow and heat transfer in microdomains have been conducted over the years, and it was established that traditional continuum models are applicable in the majority of practical engineering problems. Kiran and Muhammad et al. [53] investigated the characteristics of

microchannel heat sinks using conjugate heat transfer simulation using the Navier-Stokes equations. Mainly, the turbulent flow was analyzed, and the maximum deviation from experimental data was about 9%. Lee et al. [7] have studied both experimentally and numerically the heat transfer and fluid flow in microchannels with 194-534 μm hydraulic diameters. Excellent agreement between experiments and numerical data within a 5% deviation was achieved. It was shown that conjugate numerical models could predict the heat transfer phenomena in microchannels well. Mudawar et al. [54] numerically solved the conjugate heat transfer problem by determining temperature both in liquid and solid regions. The authors compared pressure drop and temperature measurements with numerical predictions and observed good agreement while demonstrating that the Navier-Stokes equation, together with the energy equation, can predict heat transfer phenomena in microchannels. Li and Quan et al. [55] conducted 3D simulations to explore the heat transfer and fluid flow in silicon microchannels using the QUICK [56] scheme to discretize the convective term and CLEAR [56] scheme to couple the velocity and pressure terms. Numerical results showed good agreement with experimental data. The authors also showed that the conventional theories are still applicable in the microscale with 10-100 μm geometric dimensions. Chiu and Richards et al. [57] investigated conjugate effects in a horizontal channel heated from below. Experimental results were compared to a 2D conjugate heat transfer model where two different materials were implemented as solid regions. The authors used conventional Navier-Stokes equations and solved them via Semi-Implicit Method for Pressure-Linked Equations Revised (SIMPLER) and Tri-Diagonal Matrix algorithm (TDMA) [56], demonstrating that the implementation of the conventional equations is acceptable inside the microchannel. Additionally, it was reported that conjugate effects play a great role inside the channel and affect the convection heat transfer. Lelea and Nishio et al. [58] considered the heat transfer and fluid flow of distilled water in round tubes ranging from 0.1 to 0.5 mm in diameter. Their experimental and numerical analysis also showed that conventional theories are applicable to the conditions of their

experiments. Gamrat and Marinet et al. [59] investigated fluid flow and conduction effects inside a rectangular microchannel. The main aim of the study was to obtain a relationship between the entrance effects, conduction effects, and Nusselt number. Results obtained via 2D and 3D modeling showed good agreement with experimental data available in the literature and showed that conventional momentum, continuity, and energy equations are applicable in microscale. The authors confirmed that numerical predictions are important in terms of analyzing the heat fluxes and temperature profiles, which are difficult to observe experimentally. Karayiannis and Collins et al. [60] did an extensive review of experimental and numerical results about single phase heat transfer in the microchannels. They found that scaling effects, such as conjugate heat transfer, viscous heating, entrance effects, electric double layer effects, temperature-dependent properties, and surface roughness effects, should be considered as they are dominant processes at that scale. Another conclusion was that the numerical simulations are only alternatives to reveal and thoroughly examine the above-mentioned scaling effects. It was stated that the Hausen and Shah London correlations are reliable in predicting Nusselt numbers in microchannels. Mansoor et al. [61] used the 3D conjugate model to numerically investigate the fluid flow and heat transfer under high heat flux conditions in microchannels for Reynolds numbers in the range of 500-2000. The numerical results were compared to Shah and London correlation [62] and showed good agreement. Fluent solver was used, and less than 4.2% deviation was observed between numerical and experimental results. Knupp et al. [63] reported that the few studies had resulted in a significant discrepancy between numerical and experimental results due to the neglecting scaling effects. Unlike the other studies, authors have performed 2D analytical analysis implementing generalized integral transform technique. Hybrid numerical-analytical solution to the unified partial differential energy equation was obtained, and it was shown that the inlet preheating (precooling) resulted from wall conjugate heat transfer has a great effect on the local Nusselt numbers on that actual heat transfer area, i.e., heater

embedded in the channel. Authors extended applied the same modeling technique to unsteady conjugate heat transfer problems also [64]. In more recent studies, conjugate heat transfer models are being applied to investigate the heat transfer phenomena in microchannels with porous media [65-67].

As mentioned above, thermodynamic properties of the working fluids and their change based on the temperature also have a considerable impact on the heat transfer and fluid flow phenomena inside the microchannel. Fedorov and Viskanta et al. [68] confirmed that Navier-Stokes equations are capable of capturing and predicting the hydrodynamics phenomena inside the channels. They utilized the SIMPLER algorithm to solve the coupled continuum equations and temperature-dependent properties for the working fluid. Li and Cheng [69] investigated the conjugated heat transfer in microchannels having dimensions of 10 mm long silicon substrate and with rectangular microchannels of 57 μm and 180 μm in width and depth, respectively. 2D fluid flow and 3D heat transfer were implemented during these studies. TDMA was employed to solve the governing equations. Not only geometrical parameters of the channel but also the thermophysical properties of the fluid were examined thoroughly. It was found that the thermophysical properties of the liquid have a substantial effect on the heat transfer parameters inside the microchannel [70-73]. Liu et al. [74] conducted 2D theoretical analysis by implementing varying fluid properties such as thermal conductivity and the viscosity of the fluid. The investigation concluded that the effect of property dependence reveals itself near heating channel walls and should not be neglected. Zhigang et al. [75] applied the so-called, “inlet property,” “average property,” and “varying property” models in 3D conjugate numerical modeling of the microchannel heat sink. The study compared models based on the apparent friction factors inside the channel and its relationship to the local Nusselt number. It was concluded that the “varying property” method is superior to the former techniques as it predicts the physical phenomena more accurately.

It is worth to mention that the viscous dissipation is one of the leading secondary effects in microchannels. Morini et al. [76] conducted a numerical study simulating the flow through the adiabatic microchannel to analyze viscous heating. For pipes with an inner diameter of 1 cm, when Re=1000, the temperature rise of the fluid due to viscous dissipation is 10^{-8} K, whereas it is 10 K for a pipe with an inner diameter of 100 μm. It was also shown that for Re=300 and higher, viscous dissipation could be neglected for hydraulic diameters larger than 300 μm. This fact provides enough grounds to neglect the viscous dissipation as a secondary effect for the numerical simulations that are in the scope of the current work.

1.1.4. Optimization of micro heat exchangers

Optimization and parametrization studies are critical in the design and improvement process of the microchannel heat sinks. As discussed in the preceding sections, obtaining experimental data, confirming the applicability of macro-scale physics laws and correlations, and revealing scaling effects via various numerical modeling techniques were major research concentration areas. However, during the last decade, the interest of the investigators has already started to shift implementing and improving optimization techniques that could be applied to design more effective micro heat sinks. A broad spectrum of the available experimental data was attracted to these studies for verification of the numerical models used.

In 2004, Liu and Garimalle [77] used CFD methods and obtained baseline results in a microchannel, which was designed during the pioneering work [1]. Only one channel was employed during the study results were compared against four different analytical methods, which are 1D resistance model, a fin approach, two fin-liquid coupled model, and a porous medium approach. It has been reported that the models do provide accurate predictions. The optimization results of Sung [78] supported these

results except the fin approach. It was found out that at higher aspect ratios fin model could not provide the design variables. Khan et al. [79] used the entropy minimization method to optimize the micro heat sinks in 2006. In 2010, Bello et al. [80] showed that the via employing numerical simulations and mathematical optimization, one can provide unique optimal microchannel design configurations for given pressure drop through the channel that will provide minimized peak wall temperature. Xie et al. [81] applied optimization methods to design double-layered microchannels for chip liquid cooling. Mohd et al. [82] used the genetic algorithm to compare square, and circular ammonia cooled micro heat sinks under optimized thermal performance conditions. Circular geometry was better in terms of hydrodynamics and heat transfer. Gorji et al. [83] investigated different nano-fluids and optimized the performance based on statistical methods. The favorable effect of nano-particles on thermal performance was reported. Reddy et al. [84] performed multi-objective optimization of micro pin-fin arrays in micro heat sinks in 2017. The study majorly concentrated on the hot spots, which is very common in electronic chip operations. Circular and symmetrical airfoil shapes were examined while having water as a working medium. Heat flux was 2000 W/cm^2 in the hot spot region, and maximum surface temperature was constrained at 85^0C. Even though the study was lacking experimental verification of the numerical results, it did conclude that the symmetric airfoils create less pressure drop than circular fins for a specified maximum temperature.

Recently, Hadad et al. [85] studied water-cooled multi-die heat sink with parallel rectangular micro-channels aiming at the heat transfer requirements of the multi-die processor. The microchannel shape was optimized using NSGA II (non-dominated sorting genetic algorithm) and the weighted sum method. It has been concluded that short fins provide optimal thermal performance, whereas optimal fin thickness is within the range of 0.14-0.2 mm. Yogesh et al. [86] also studied the effect of fin height on heat sink performance and concluded that in a channel whose height is 1.0 mm, maximum fin height should

optimally be 0.8 mm. It was numerically calculated that the above this value, thermal performance decreases. When the latter two studies investigated carefully, it is apparent that the optimal fin height in a microchannel heat sink is varying based on the application and applied boundary conditions. This fact also creates an urge for further micro heat sink optimization studies. Haziq et al. [87] optimized segmented micro heat sink with rectangular channels using the Taguchi-grey method and concluded that fin width of 1mm, length of 2mm together with transverse direction of 2mm provided maximum heat transfer performance at minimum pressure drop. Consequent analysis of such micro heat sink was able to cool the chip with a heat flux of 800 W at 56.6^0C. Dokken et al. [88] conceptualized parts made by additive manufacturing as a 2D bit array in their simulations. Discretizing rectangular area of 500 mm^2 and applying representative heat flux calculated from flux dependent probability function based on two different chip powers, a map of such bit arrays was optimized. It was found out that even though the entropy generation rate is decreased by 25%, the pumping power requirement reached an order of magnitude higher percentage increase relative to thermal effectiveness gain. The authors concluded that further research is necessary for finding solutions with lower pressure drops while keeping thermal performance higher. Yan [89] studied Y-shaped fractal networks using single and multi-objective optimizations coupled with 3D fluid-solid conjugate numerical simulations. It was reported the single-objective optimization lacks the capability to provide thermally effective designs. Subsequent multi-objective optimization resulted in a solution that has higher thermal performance at 25% lower pumping power requirements confirming that multi-objective optimizations are necessary. Xiaojun et al. [90] optimized micro heat sinks with plane channels where triangular void areas were created within the channel walls introducing secondary flow, and as a result, thermal resistance and pumping power of the optimized channel are reported to decrease 28.7% an 22.9 %, respectively. Tan et al. [91] studied four different channel configurations including ternate veiny, lateral veiny, snowflake-shaped, and spider-

netted. The study concluded that spider-netted shape is the best, and further optimization was performed on its geometrical parameters. The resultant heat sink provided 9.9^0C lower heat source temperature operating at 100 W/cm^2. Ma et al. [92] studied the heat transfer enhancement characteristics in a micro heat sink, including ten parallel microchannels with 49 identical jetting and throttling structures. Even though both structures resulted in substantially higher pressure drops, jetting structures showed better thermal performance than throttling ones.

Overall, it could be mentioned that optimization studies around micro heat sinks with solitary and array of pin fins are still evolving. Most of the optimization studies concentrate on traditional multi-channel heat sinks with a focus on decreasing thermal resistance with minimal pumping power requirements. However, research on the optimization of the pin fin shapes and consequent local and average heat transfer enhancement is absent. Based on the recent literature, there is a severe urge to control the fluid flow in the channels implementing hydrodynamically practical shapes that favor higher convective heat transfer coupled with minimal pressure drops. Single and array of pin fins such as hydrofoils are yet to be studied and optimized to provide better thermal performance.

1.2. Research Objectives

Based on the literature review, it could be stated that there are unresolved heat transfer and fluid flow issues in the micro-scale, including hydrofoil shaped pin-fin geometries. Therefore, below are the main objectives of this study:

- Evaluate the applicability and effectiveness of cylindrical pin fin (embodying jet slots) on the heat transfer enhancement in the microchannels.
- Evaluate the applicability and effectiveness of hydrofoil pin fins on the heat transfer enhancement in the microchannels.

- Optimize the micro heat exchanger designs, including hydrofoil pin fins in terms of hydrodynamics and heat transfer.
- Create novel, hydrofoil-like pin fin geometries maximizing local and average heat transfer coefficient

1.3. Research Plan

To achieve the objectives, the following tasks are proposed for the research study

1. Build single phase numerical (conjugate) models and verify against the data obtained during the experiments, including microchannels with cylindrical pin fin (embodying jet slots). Elaborate on the local and average heat transfer and hydrodynamic parameters.
2. Build single phase numerical (conjugate) models and verify against the data obtained during the experiments, including microchannels with hydrofoil pin fin. Elaborate on the local and average heat transfer and hydrodynamic parameters.
3. Perform flexible parametrization of hydrofoil geometry
4. Perform optimization on single hydrofoil with an objective of maximized average heat transfer coefficient
5. Perform optimization on hydrofoil with a satellite with an objective of maximized average heat transfer coefficient.
6. Perform optimization with multiple hydrofoils with an objective of maximized local heat transfer coefficient.

CHAPTER 2. VALIDATION OF COMPUTATIONAL METHODS

2.1 Cylinder with jets in a crossflow

2.1.1. Experimental Setup and Numerical Model

To explore the heat transfer enhancement potential in a microchannel, Wang and Peles [93] experimentally studied an active flow control technique by introducing liquid jets to the main channel flow. The experiments are briefly introduced below; for more details regarding the experimental procedures, please refer to [93].

The microchannel was 18.5 mm long, 1.5 mm wide, and 225 µm high (hydraulic diameter of D_h 391 µm). Inside the channel, a single 150 µm diameter pin fin was placed 13.5 mm away from the fluid inlet. A thin-film, 1 mm × 1 mm serpentine heater was positioned 225 µm away from the pin fin's center. A secondary jet flow was introduced from a 50 µm diameter orifice at the bottom of the pin fin and then issued from two 25 µm wide slits, located at an angle of 110° with respect to the stagnation point Figure 3, into the main flow. The jet-to-crossflow momentum coefficient, a non-dimensional parameter, was used to quantify the jet respected to the main channel flow:

$$C_{\mu} = \frac{\rho_j v_j^2 A_j}{\rho_{\infty} U_{\infty}^2 A_c} \tag{2}$$

where ρ_{∞} and U_{∞} are the density and mean velocity in the main flow; ρ_j and U_j are the density and mean velocities of the jet flow, respectively. A_j is the slits open area along with the height of the channel, and A_c is the cross-section area of the microchannel. In the experimental study, the same liquid was used for both the main flow and the jet flow ($\rho_{\infty} = \rho_j$). Therefore, the momentum ratio was reduced to:

$$C_{\mu} = \frac{v_j^2 A_j}{v_\infty^2 A_c} \tag{3}$$

Simulations were performed using a commercial code, Star CCM+®. Fluid, solid, and heater regions were defined using the 3-D geometry prepared by SolidWorks CAD software. The dimensions of the experimental device were reproduced in the numerical model, as shown in Figure 4. The polyhedral mesh was used for all the regions as shown in Figure 5.

Conjugate effects were introduced to the model using the interfaces, and thin geometries termed shells. Since the thickness of the heater, 100 nm, was six orders of magnitude smaller than the 1-mm thickness of the solid part, this specific region was defined as a shell with two interfaces, which were in contact with the fluid and the solid regions covering only the heater area. Another interface between the solid and fluid regions covering all the areas except the heater was created. All the interfaces were specified as in-place contact interfaces.

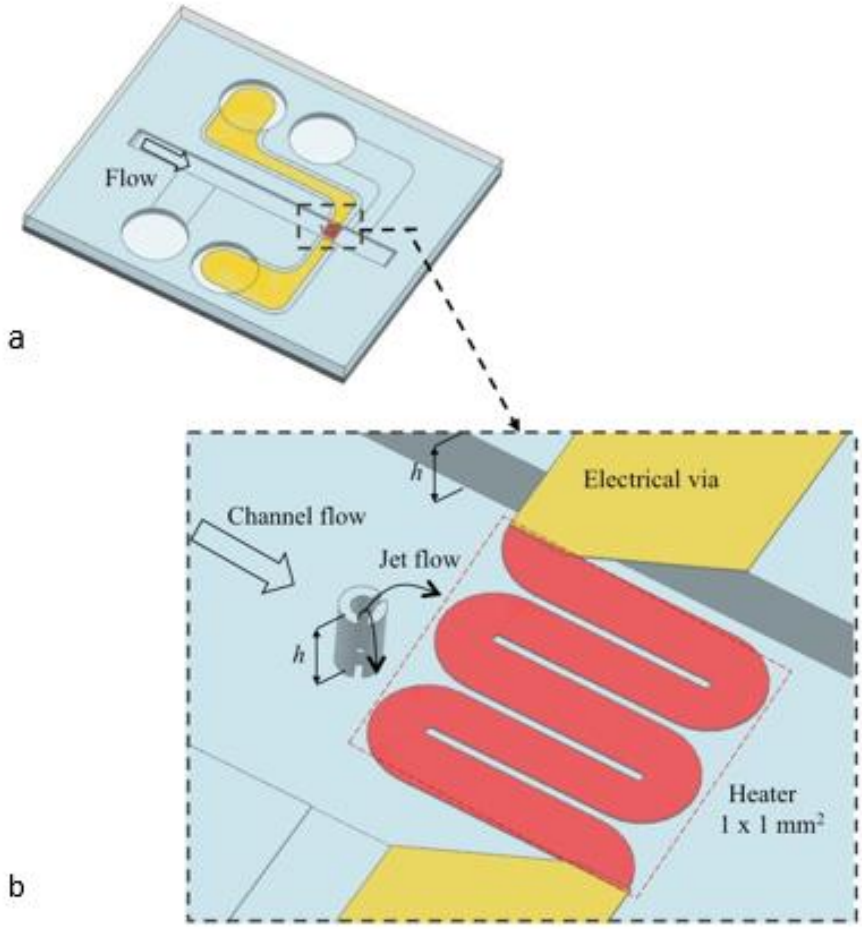

Figure 3 a) CAD model of the micro-device, and b) zoom-in view of the pin fin and the heater. The pin fin has the same height as the channel. A secondary jet flow was introduced from an orifice at the bottom of the pin fin and then issued from two slits and mixed with the main channel [93].

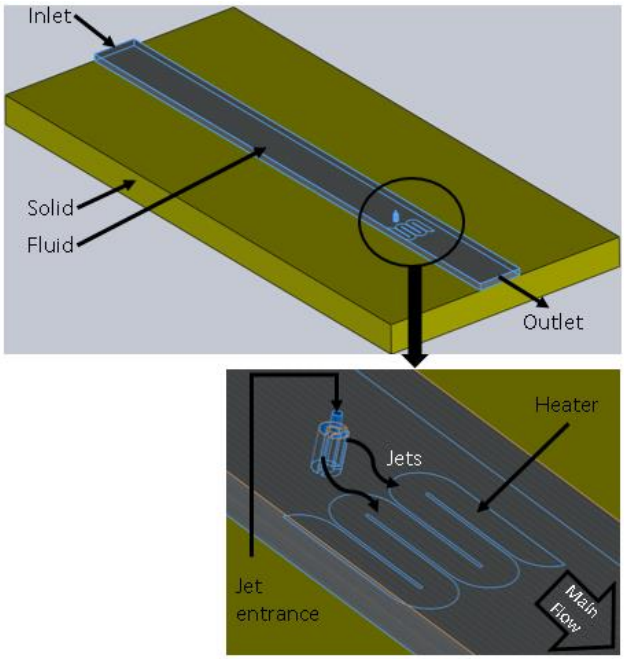

Figure 4 Geometry of the model based on the experimental device used by Wang et al. [93].

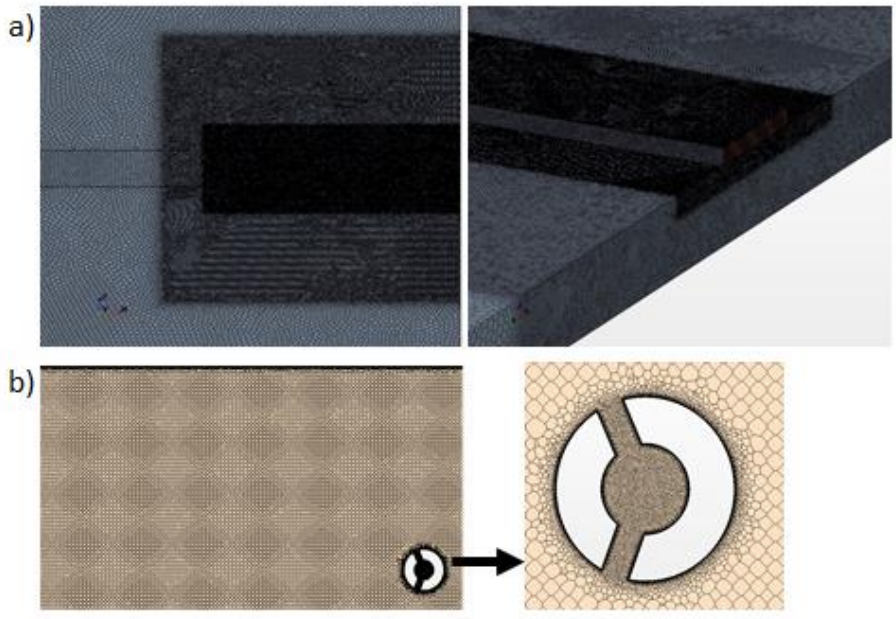

Figure 5 Computational mesh details for a) fluid and solid regions b) region around the cylinder

The simulations were performed using available models and related equations of the commercial code. General governing equations are depicted in equations 4-7. Custom specified values were used where necessary. HFE 7300 was used as a working fluid during experiments and numerical modeling. In general, for the laminar cases without jets, steady-state segregated fluid and energy equations were solved using the SIMPLE and Gauss-Seidel algorithm. For the cases including jets, the Gamma ReTheta transition model, together with an implicit unsteady solver, was used. Gamma ReTheta transition model provided insight to the laminar to turbulent transition in the vicinity and downstream of the cylinder walls where nearly turbulent behavior of the flow is dominant. The correlation used within the model is available in the theory guide of the software [94]. The parameters defining the model performance was calculated based on the expected boundary layer thickness and the Turbulent Kinetic Energy (TKE) values calculated via micro-particle image velocimetry (µPIV) measurements. Further details of the boundary conditions of this model are discussed in the conjugate heat transfer section.

The correlation developed by Williamson et al. [95] describing the relationship between St and Re number was utilized in determining the time step size for unsteady simulations. Base case simulations were performed to verify the applicability of the correlation for the flow around micro pin fins. The results and further discussion is presented in the conjugate heat transfer section.

Governing Equations of Flow (Integral Forms):

Continuity:

$$\frac{\partial}{\partial t}\int_V(\rho)dV + \oint_A \rho(v).da = 0 \tag{4}$$

Navier Stokes:

$$\frac{\partial}{\partial t}\int_V(\rho)dV + \oint_A \rho v \times (v).da = -\oint_A pI.da + \oint_A R.da + \int_V f.dV \tag{5}$$

Energy Equation:

$$\frac{\partial}{\partial t}\int_V(\rho E)dV + \oint_A[\rho H(v)].da = -\oint_A \dot{q}''.da + \oint_A R.vda + \int_V(f.v)dV + \int_V sdV \quad (6)$$

Governing Equations of the Solid (Integral Forms):

Energy Equation:

$$\frac{d}{dt}\int_V \rho c_p T dV = \oint_A \ddot{q}.da + \int_V sdV \quad (7)$$

Boundary Conditions and Sensitivity Analysis

A thorough investigation was performed on the boundary conditions and their effects on the simulation outcomes. A Reynolds number value of Re_D=123 and a momentum coefficient of C_μ=3% were chosen to perform the analysis. Especially, the Pyrex wall boundary conditions were examined due to a lack of prior information. During experiments, the bottom surface of the Pyrex substrate was exposed to the room environment, the temperature of which was not measured and recorded due to experimental setup limitations. However, while setting up the simulations, boundaries must be exposed to values close to real conditions to make sure that the desirable physics is captured. Thus, sensitivity analysis on the effects of different boundary conditions on the Pyrex walls was conducted. As a result, it was found that the Rayleigh number was less than 103, suggesting that heat is transferred to the air only through conduction and natural convection is suppressed. Also, conduction through air medium was assumed to be negligible because of its low thermal conductivity. Therefore, varying boundary condition based on the external temperature at the bottom of the Pyrex was implemented. The expression for calculation of the local radiation heat transfer coefficient at the bottom side of the Pyrex/solid region was utilized and is shown below;

$$h_{local,rad} = 0.92 * 5.671 * 10^{-8} * (T_s^2 + T_\infty^2) * (T_s + T_\infty) \quad (8)$$

where T_s is the external surface temperature, T_∞ is the ambient temperature, 0.92 is the emissivity for the Pyrex and $5.671*10^{-8}$ is the Stefan-Boltzmann constant. Under these conditions, the average value of the heat transfer coefficient was 5.3 W/m^2K.

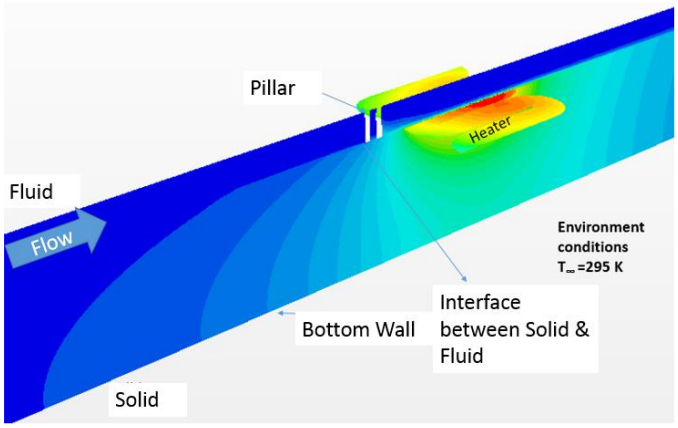

Figure 4 Description of the boundary conditions in the 2D plane.

Grid Independence Study

Grid independence of this numerical study was established based on the model developed by Roache et al. [96]. The model was implemented by choosing three different grids with refining ratios of 1.25 and 1.33, which represents coarse to medium and medium to fine, respectively. Temperature values were taken as the key variable to validate the implementation of the model. The global order of convergence value, p, and ratio values, B, for asymptotic convergence validation, are presented in Table 1. As shown, the calculated p values are very close to the theoretical order of convergence, which is $p_{theoretical}$=2.0. Moreover, the B values are close to 1.0, indicating that the use of Roache's model is valid. From Table 1, it can also be inferred that p does not change substantially with

increasing momentum coefficient while keeping Reynolds number and average mesh element volume size constant. This information could be used for future parametric studies to help decrease computational cost.

Table 1 Grid Convergence Index (GCI) Parameters

Re_D , Cμ	B	p	GCI_{fine}
123, 3%	0.98	2.026	2.40%
123, 5%	0.98	1.926	2.47%
123,10%	0.97	2.12	2.26%
200,10%	1.07	2.06	2.35%
280,10%	1.02	2.25	2.21%

2.1.2. Validation Results

The numerical model was validated against the experimental data from Wang et al. [93]. Assumptions made during experiments to calculate heat transfer parameters, such as the average heat transfer coefficient and Nu number was reevaluated through the numerical model and to provide further insight into the conjugate conduction/convection heat transfer processes.

Validation of the numerical model

Validation of the fluid dynamics, temperature distribution, and the heat transfer coefficient are required to support the findings established by the numerical results. An effort to provide such validation is presented below.

Hydrodynamics validation

Velocity distribution results extracted from the numerical simulations were compared to the previously obtained experimental μPIV measurements of Wang et al. [93]. The reference study calculated the ratio of the longitudinal velocity component to the mean velocity in the fluid region. Figure 6 and Figure 7 depict a comparison between experimental and numerical results. The difference between the velocity ratio values is less than 5%. The jet introduction to the main flow region is captured reasonably well by the numerical model. The secondary flow mechanisms close to the sides of the cylinder starts to develop with the increasing momentum coefficient. While the jets are introduced to the main flow, downstream of the cylinder, secondary circulation regions appear and create unsteadiness that depends on the Reynolds number. The velocity fields immediately behind the cylinder are very similar. As the momentum coefficient increases, the re-circulation region immediately behind the cylinder intensifies. Further insight into the steady and unsteady behavior of these flows is given in the conjugate heat transfer section.

The differences between the numerical and experimental results are attributed to dimensions used in these simulations being slightly different than the actual design dimensions of the microdevice, and to numerical diffusion and experimental uncertainties. However, the agreement between the experimental and numerical results is good.

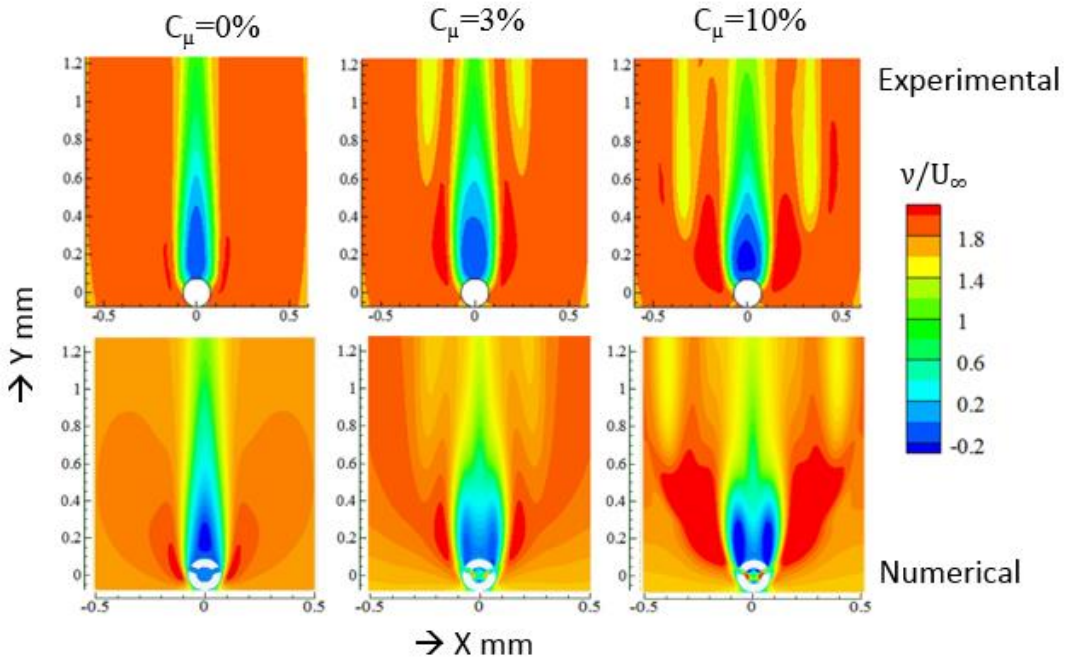

Figure 6 Experimental and numerical normalized velocity contours for Re_D=123 at 1/2 plane.

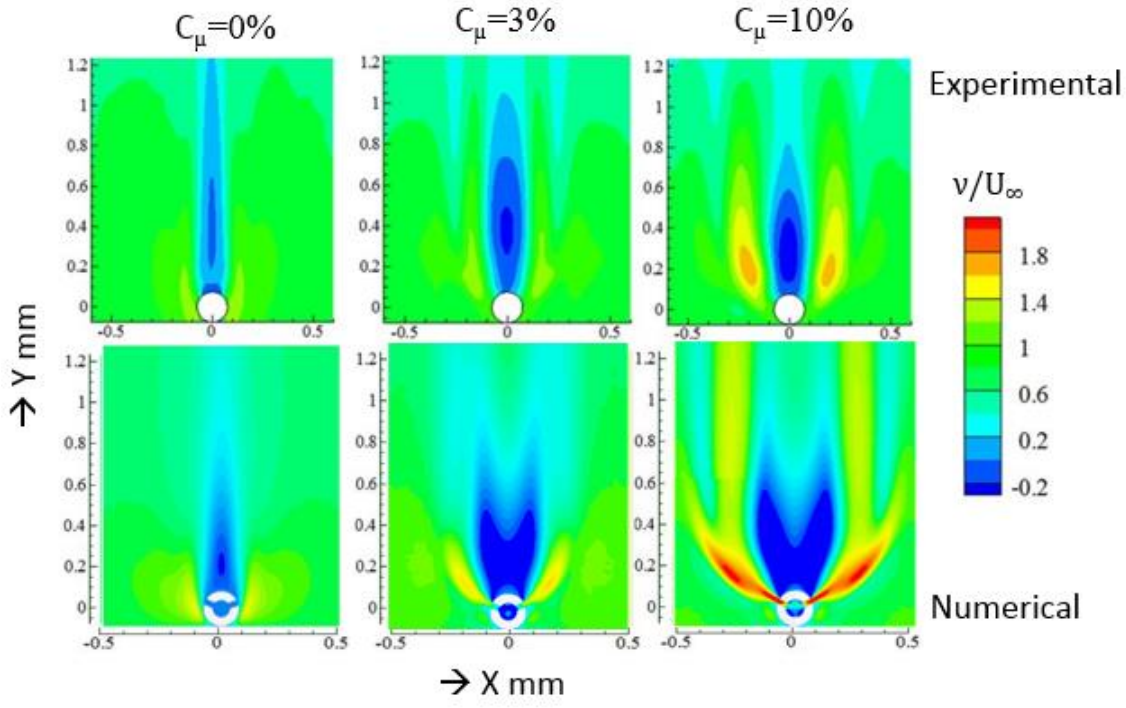

Figure 7 Experimental and numerical normalized velocity contours for Re_D=123 at 1/8 plane.

Temperature Validation

The surface temperature within the heater area was measured experimentally through resistance temperature detectors (RTDs). The measurement method is explained in the experimental work of Wang et al. [93]. Limited by the microdevice capability, only area-averaged temperatures were obtained by experiments.

Figure 8 depicts the comparison between experimental and numerical average surface temperature results for different jet ratios and Reynolds numbers. The error bars on the numerical data were calculated based on the previously discussed GCI analysis. Overall the difference between the numerical and experimental values is within ±10%. The most considerable difference is occurring in Re_D=123, Cμ=3% case which is 9.8%. The minimum percentage difference is 5 %, which shows itself in the Re_D=280, Cμ=10% case.

Even though the current numerical model represents most of the real experimental boundary conditions, there still could be small discrepancies. Another source of differences is due to the inability to measure or observe certain boundary values.

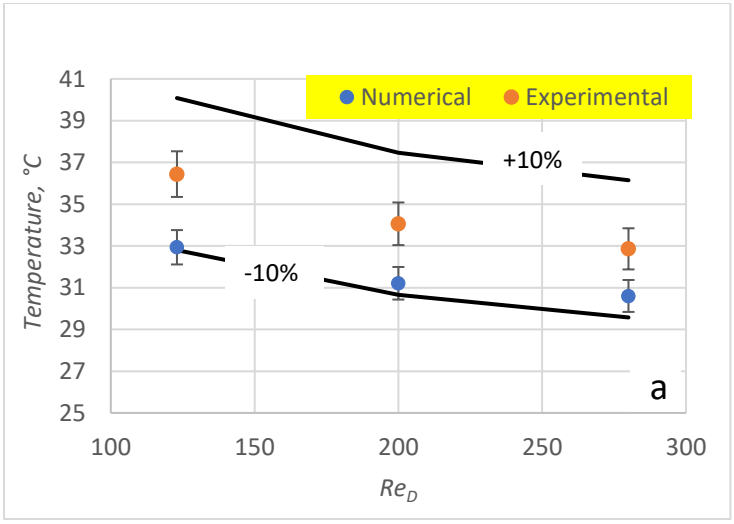

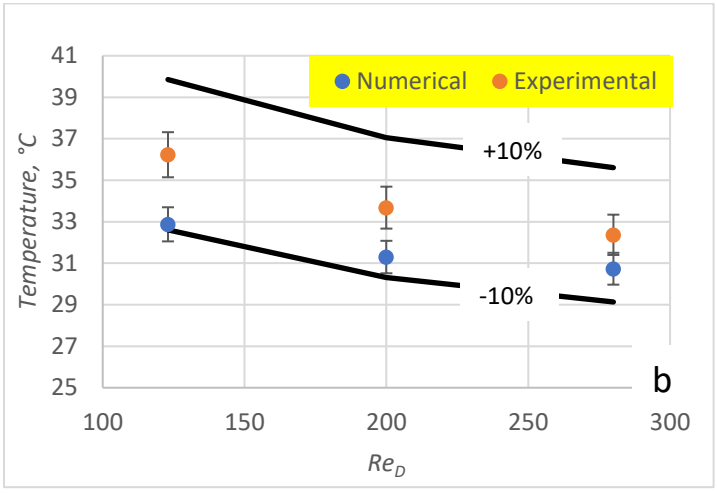

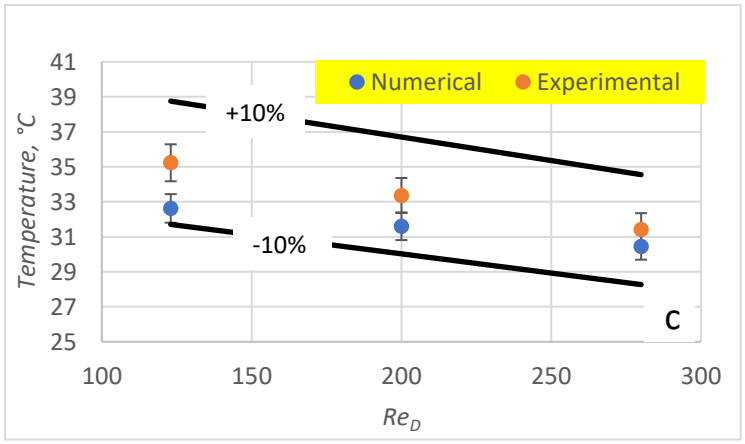

Figure 8 Temperature comparison between experiments and numerical model for a) Cμ=3%, b) Cμ=5%, and c) Cμ=10%.

Heat transfer coefficient and enhancement factor validation.

Heat transfer coefficients were calculated using the equation set presented by Wang [93]. The parameters such as heat flux and surface temperature were obtained from the numerical simulations. The heat transfer coefficient was calculated based on the total heat transferred to the fluid region through the heater area. It has to be noted that the method mentioned above will be discussed in depth in the proceeding sections and is used here for comparison purposes only. The maximum difference between experimental and numerical values is about 30%. There is a slight increase in the gap between experimental and numerical heat transfer coefficient values as the Reynolds number or momentum ratio increases. The same pattern was observed during the numerical studies done by Kiran et al. [97]. The authors showed that the discrepancy in pressure loss magnitude between experimental and numerical results is rising with increasing Re number. This, in turn, shows that for the same Re number, friction factors for numerical and experimental results will be different and keep increasing with Re number. Based on the Re analogy, this effect could be one of the sources of the observed discrepancies between numerical and experimental heat transfer coefficients. The distribution and increasing pattern of the average heat transfer coefficients are captured by the numerical model and is shown in Figure 9. The enhancement factor was calculated based on the experimental and numerical data according to equation 9 used by Wang et al. [1].

$$En = \frac{\overline{Nu_J} - \overline{Nu_0}}{\overline{Nu_0}} \tag{9}$$

The respective results are shown in Figure 10 for j=10, corresponding to the average Nu number calculated at Cμ=10%. The difference between enhancement factors calculated based on numerical and experimental data is less than 10 %.

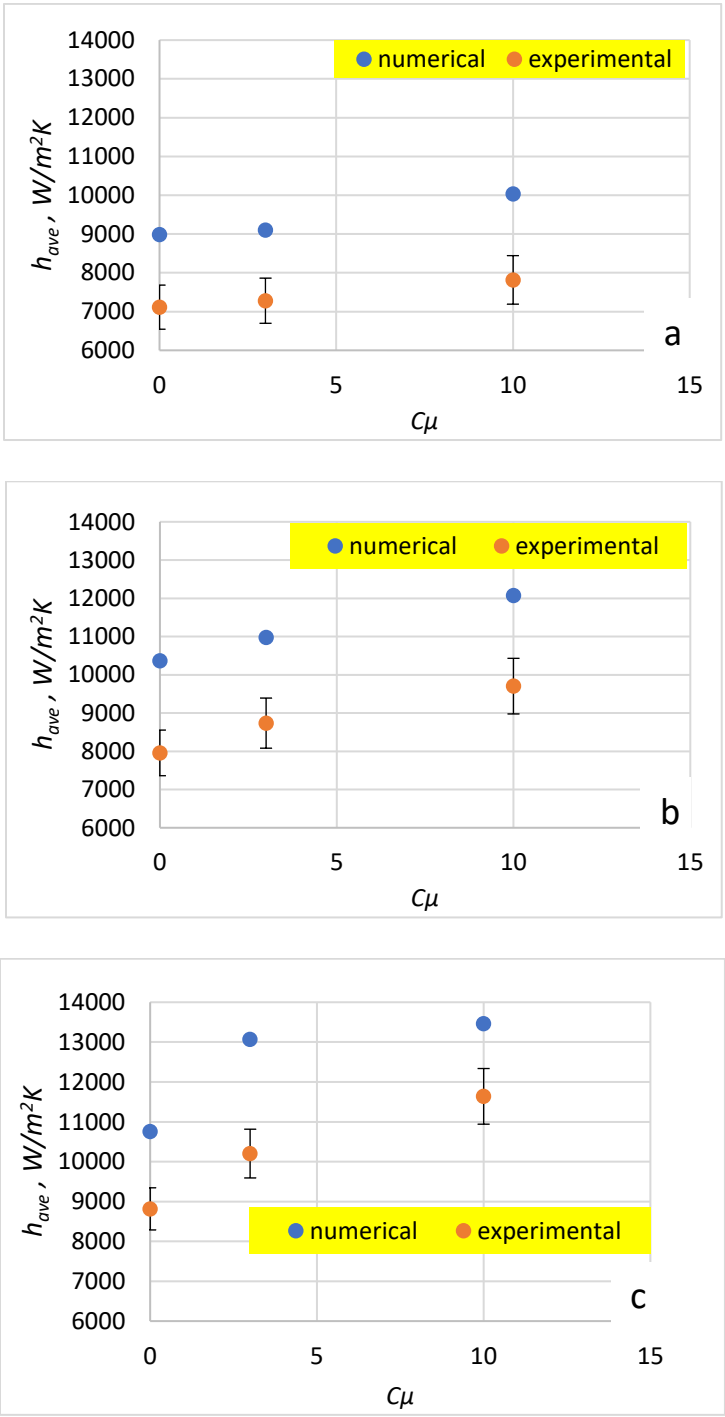

Figure 9 Average heat transfer coefficients comparison between experiments and numerical model for a) Re_D=123, b) Re_D=200, and c) Re_D=280

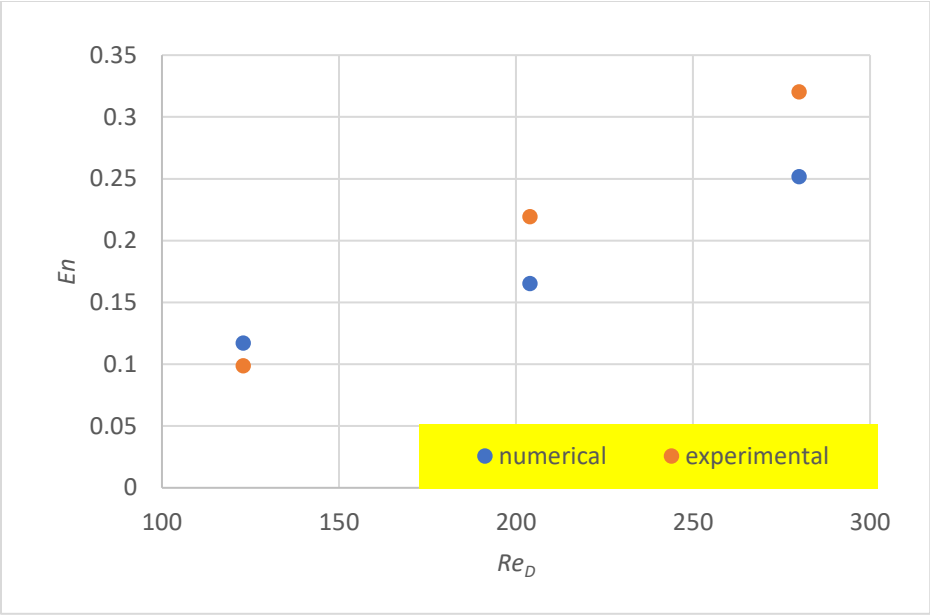

Figure 10 Enhancement factor comparison between experiments and numerical model.

Conjugate Heat Transfer

The interaction between the solid structure and the fluid can lead to significant local heat losses, which can result in erroneous interpretation of the local heat transfer coefficient, and the effective heat flux dissipated directly to the fluid.

Importance of numerical modeling for microchannel heat transfer measurements

One of the main objectives of this study is to reveal the complexities related to the interpretation of the results of the experiments and how numerical modeling can be used to resolve them. The heat transfer experiments, which were used by this numerical study as a validation, measured only average temperatures of the heater for a range of hydrodynamic cases. This is due to the difficulties that resulted from the miniature dimensions and available instrumentation techniques, which are overcome by numerical modeling.

Figure 11 shows the heat transfer coefficients calculated via numerical simulations and experimental post-processing techniques. Only Re_D=280 was presented for brevity. The main discrepancy is due to the difference between heat flux calculations from the heater to the fluid region. Experimentally, once the heat loss was estimated, it was assumed that the heat generated by the heater was directly dissipated into the adjacent fluid region. However, the conjugate heat transfer simulations revealed that the heat paths inside the solid, heater and fluid regions are much more involved. Figure 12 depicts the main heat transfer paths inside the three regions. Heat leaving the heater region is distributed to the fluid and solid region unevenly and is directly related to the fluid mainstream Reynolds number. As the heat advances inside the solid region, the surface of the solid that interfaces the fluid corresponds to the lowest thermal resistance path. Due to this fact, even though more the 90 % of the heat is transferred to the fluid in every case analyzed, not all of the convective heat transfer is occurring at the heater surface. This affects only the value range of the heat transfer coefficient and does not change the enhancement ratio mentioned above, as shown in Figure 11.

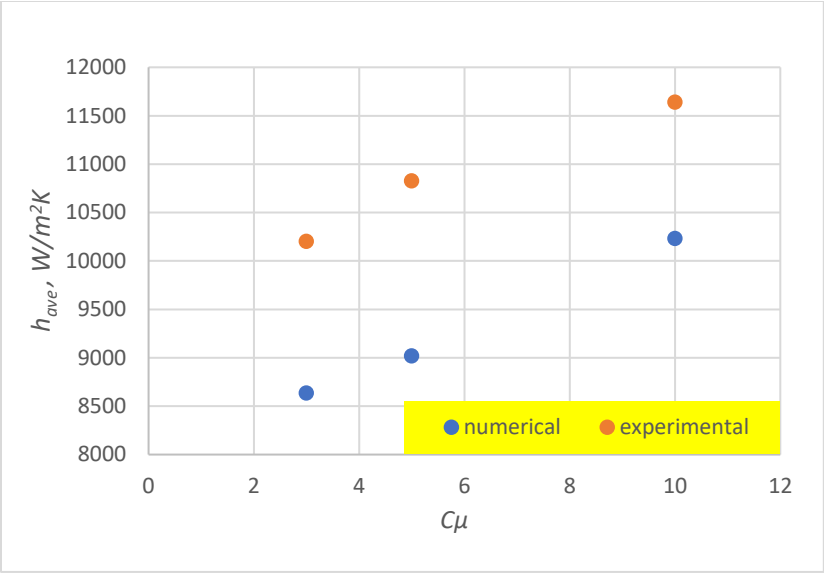

Figure 11 Heat transfer coefficient comparison based on experimental and direct numerical results for Re_D=280.

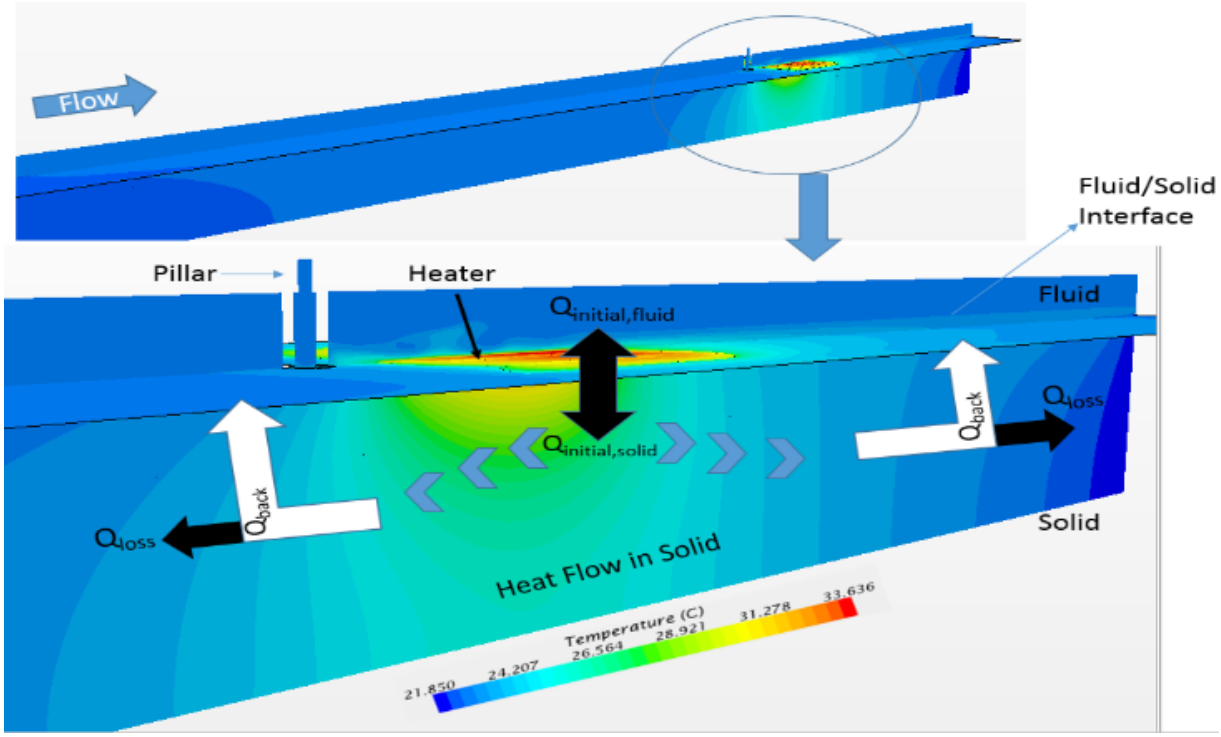

Figure 12 Heat paths inside the solid and fluid regions.

Unsteady Conjugate Heat Transfer Simulations

To be able to capture the unsteadiness created in the flow due to the introduction of the jet, an implicit unsteady model was implemented. The current physical problem includes solid and fluid regions, which have very different physical characteristics and different geometrical dimensions. These discrepancies lead to the requirement of vastly different time steps that should be used for the unsteady solution. He and Oldfield et al. [98] reported the time step size for solid to be 10000 times greater than for the fluid for a convection/conduction coupled problem of flow over the turbine blades, which was resolved using co-simulation procedure. As the unsteady region of the flow is capturing a very small region compared to the overall solid dimensions, the solid region was solved using steady-state solver, whereas the fluid region solution was obtained via implicit unsteady solver. The two simulations were coupled by transferring data at the contact surface. For the cases where a periodic solution was obtained, the contact surface of the solid region was updated at every period, while for the steady cases, the update of the interface was done every 1000 iterations. The co-simulation procedure was continued until the convergence criterion was met in both regions.

Unsteady Hydrodynamics

This section mainly concerns the hydrodynamic behavior of the flow behind the pin fin as the Reynolds number and jet ratios are changing. The classification of the unsteady and steady flows is presented. The velocity variation was recorded at the point taken on the half-plane of the fluid region, as shown in Figure 13.

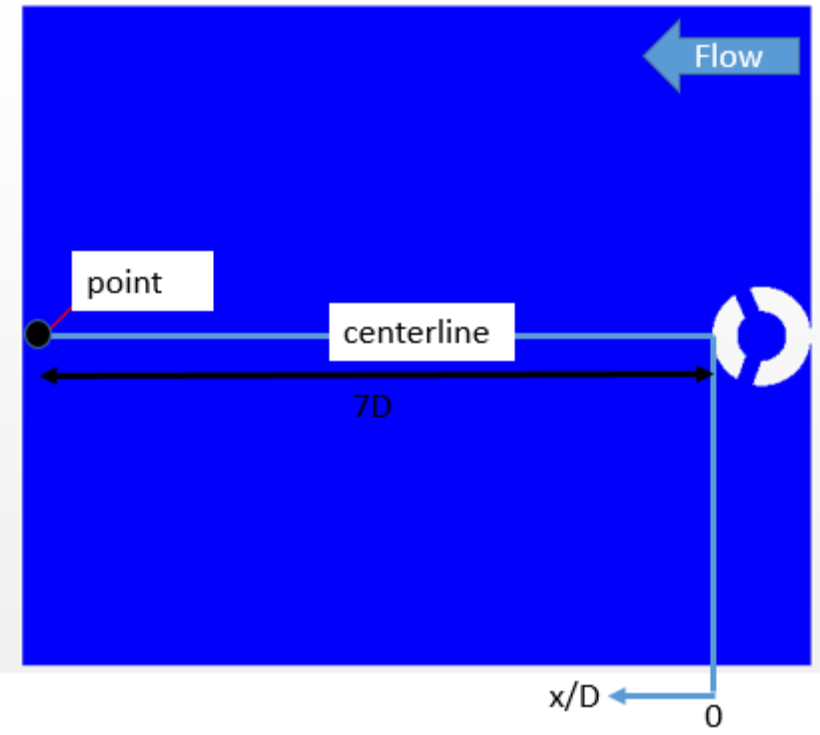

Figure 13 Location of the point where the velocity data is recorded.

Base Case for unsteady flow simulations

Williamson et al. [95] studied the Strouhal/Reynolds relations for flow over a cylinder in 3-D laminar and turbulent regimes. Two different correlations were proposed ,which are given in $St = 0.2665 - \frac{1.018}{\sqrt{Re}}$ (10 and $St = 0.2234 - \frac{0.3490}{\sqrt{Re}}$ (11 for $190<Re_D<230$ and $Re_D>230$, respectively.

$$St = 0.2665 - \frac{1.018}{\sqrt{Re}} \quad (10)$$

$$St = 0.2234 - \frac{0.3490}{\sqrt{Re}} \quad (11)$$

The base case of Re_D=500 was executed to examine the validity and applicability of the above-mentioned correlation to the current study. The predicted frequency by $St = 0.2234 - \frac{0.3490}{\sqrt{Re}}$

(11 is calculated to be 4046 Hz. The appropriate time step was calculated to be 2.5×10^{-5} s, which is $1/10^{th}$ of the predicted period.

Figure 14 depicts the respective velocity variation and related fast Fourier transform (FFT). The simulated vortex shedding frequency is 4176 Hz, which is 3.2% higher than the predicted value of 4046 Hz. As the simulated and predicted vortex shedding frequencies are in good agreement (<5%), the above-mentioned correlations are used to calculate the time step of the subsequent simulation.

Flow Behind the cylinder with jet introduction, steady and unsteady flow

To classify and quantify the unsteadiness of the flow and to reveal the effect of the unsteadiness on the heat transfer, three jet introduction cases for three different Re numbers are studied. As mentioned in the above section discussing numerical models Gamma ReTheta model was used to solve the flow equations to capture the possible laminar to turbulent transitions inside the region. Since the turbulent boundary conditions affect the solution, especially for the current model, the experimental results for the turbulent kinetic energies of the reference study [93] were used to estimate the turbulence intensities at the jet boundaries. For example, Re_D=123 and Cμ=10% turbulence intensity values of 9% were used at the inlet of jets. The resulting turbulent kinetic energy (TKE) distribution was calculated using the approach taken by Wang et al. [93], and very close values to experimental observations were achieved and shown in Figure 15. All of the cases with a jet introduction were run using an implicit unsteady model. As a result, some of the cases turned out to become steady while others stayed unsteady.

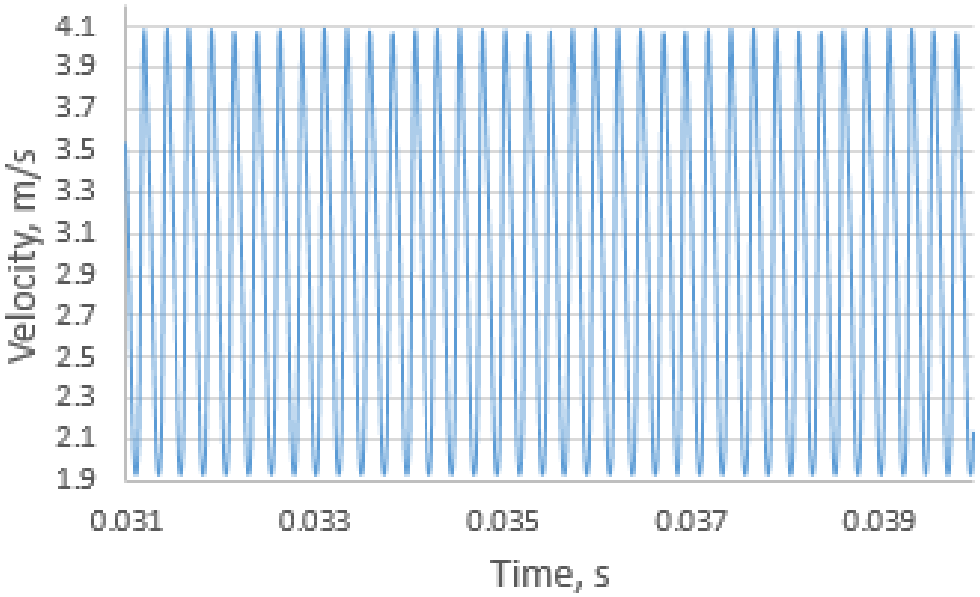

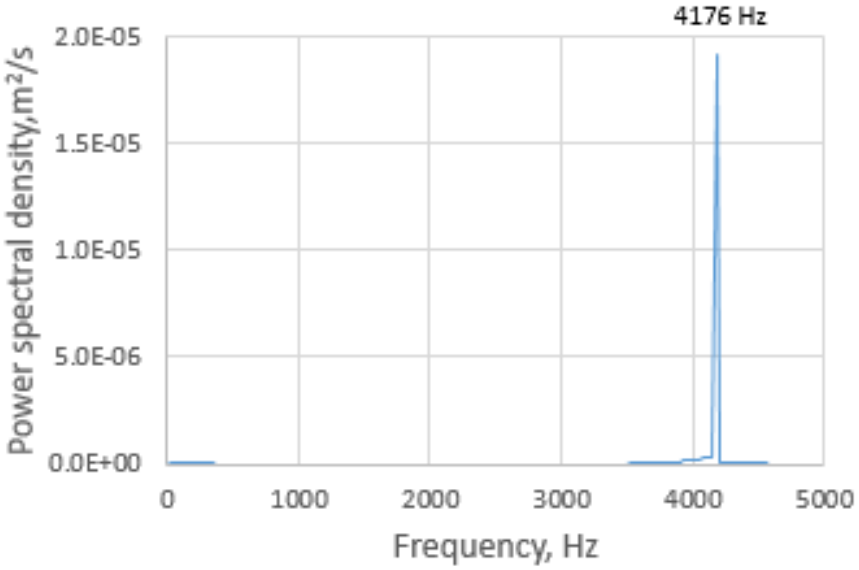

Figure 14 Baseline case simulation velocity and FFT results for Re_D =500

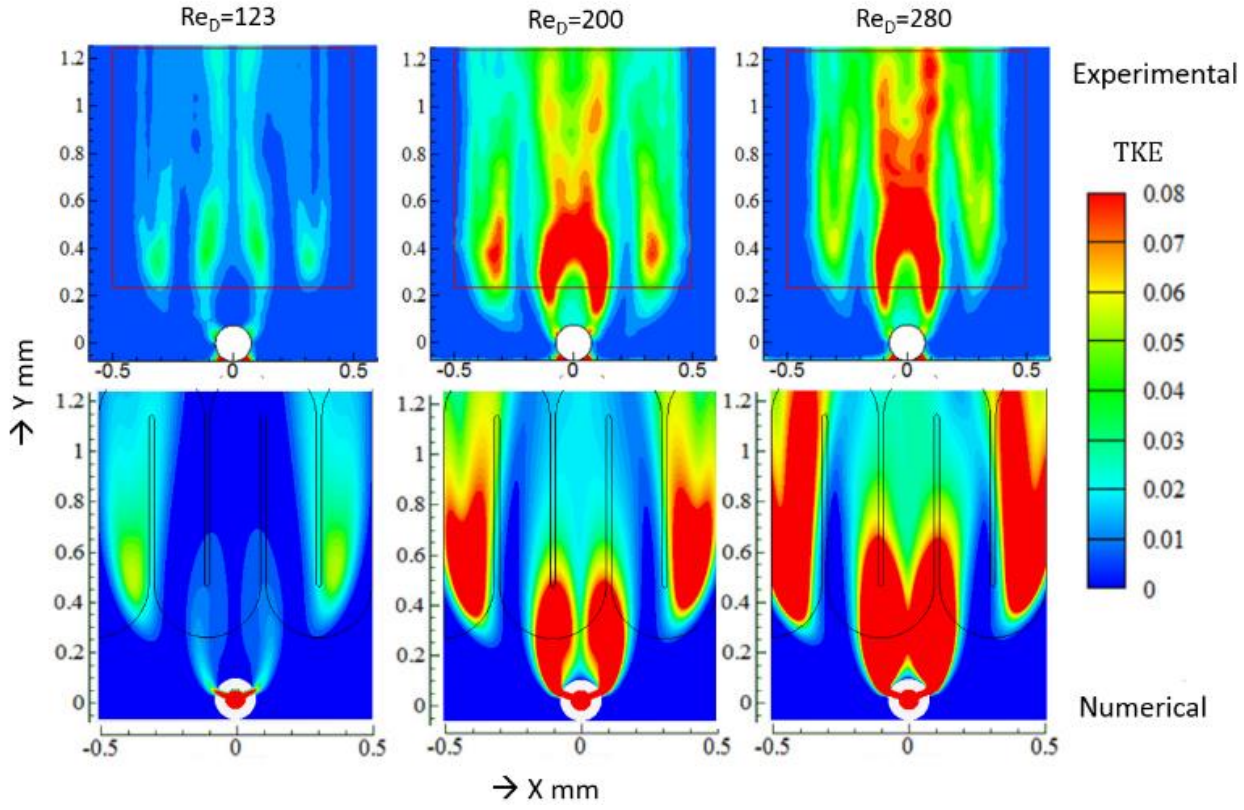

Figure 15 Turbulent kinetic energy comparison between experimental and numerical results at half-plane.

Figure 16 depicts the velocity oscillations at the point shown in Figure 13. The decaying unsteadiness and eventually steady flow was observed for the cases of a, b, and d in Figure 16. For the cases c, e, and f in the same figure, sustained unsteadiness is apparent. It has to be noted that jets are acting like blockage mechanism to the main flow. As a result, a decrease in the average velocity magnitude behind the cylinder occurs, which is very visible among the cases d and e. The sustained unsteadiness was obtained in lower momentum ratios as the Reynolds number was increased.

The FFT results are seen in Figure 17. For each unsteady flow case, main vortex shedding frequency and its harmonics at the point of interest were shown. The main frequency value and its amplitude increases as the Reynolds number increases for the same momentum ratio. However, for the same

Reynolds number, as the momentum ratio increases, the main frequency is unchanged while the amplitude is increasing. For instance, the main frequency and amplitude increased by 40% and 67 %, respectively, for the same momentum ratio and increased Reynolds number. This results in higher velocity fluctuations and higher average turbulent kinetic energy values, which are the major mechanisms responsible for the heat transfer enhancement with momentum ratio.

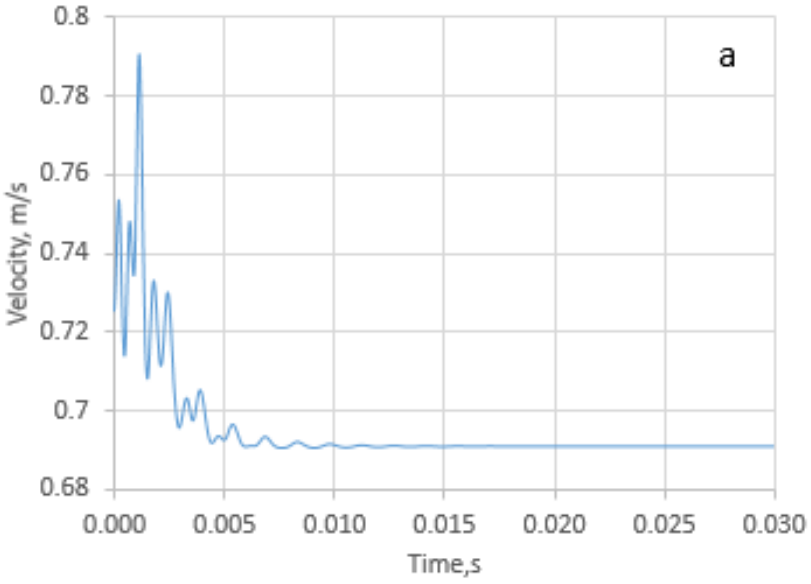

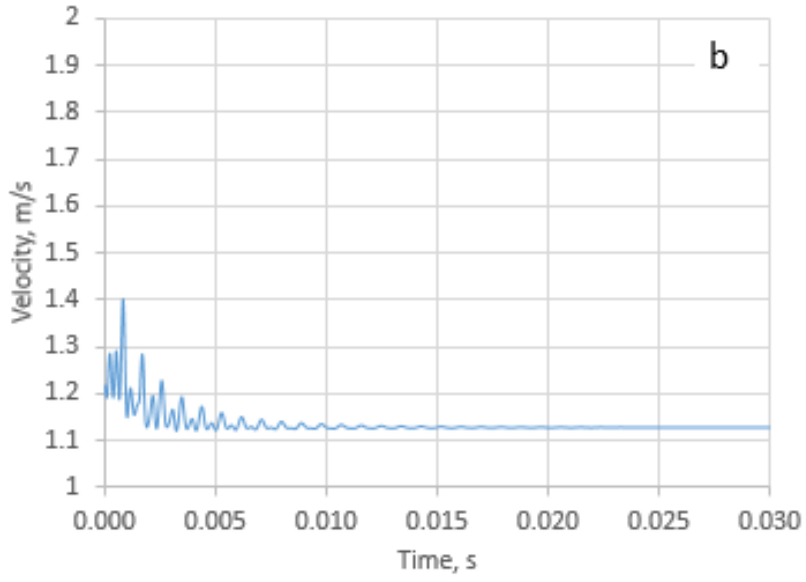

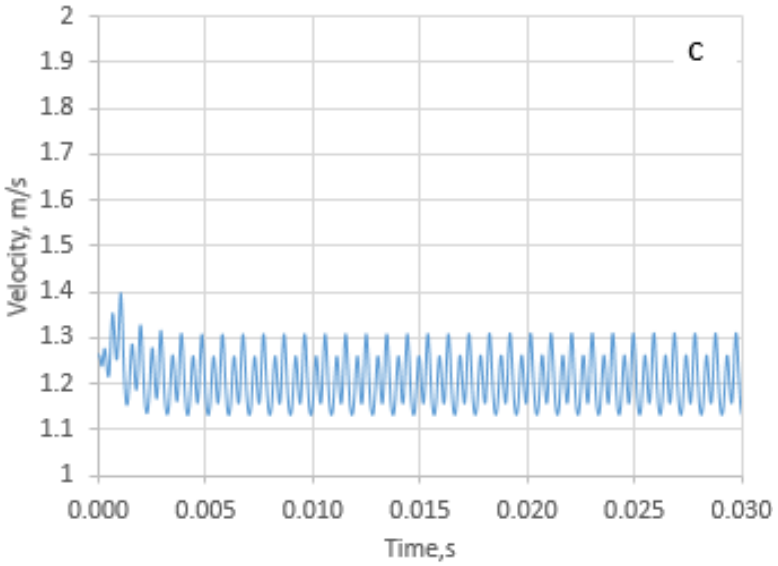
c
Velocity, m/s
2
1.9
1.8
1.7
1.6
1.5
1.4
1.3
1.2
1.1
1
0.000
0.005
0.010
0.015
0.020
0.025
0.030
Time,s

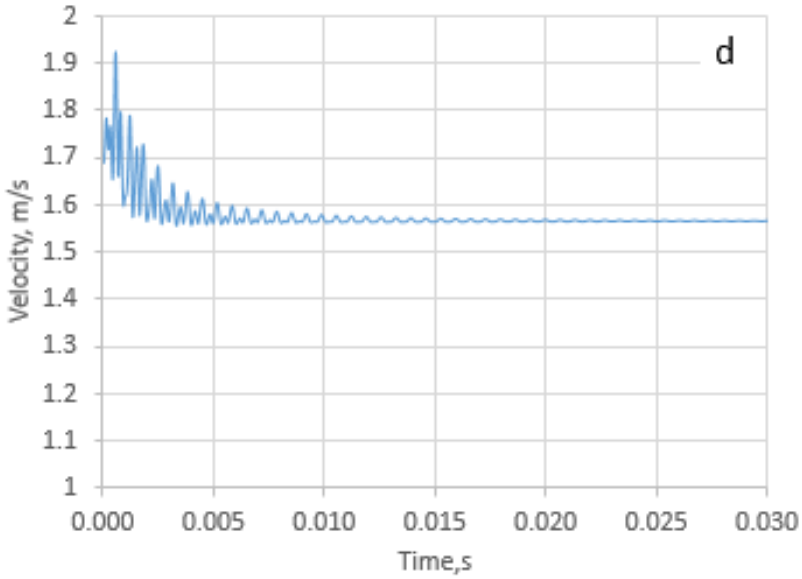
d
Velocity, m/s
2
1.9
1.8
1.7
1.6
1.5
1.4
1.3
1.2
1.1
1
0.000
0.005
0.010
0.015
0.020
0.025
0.030
Time,s

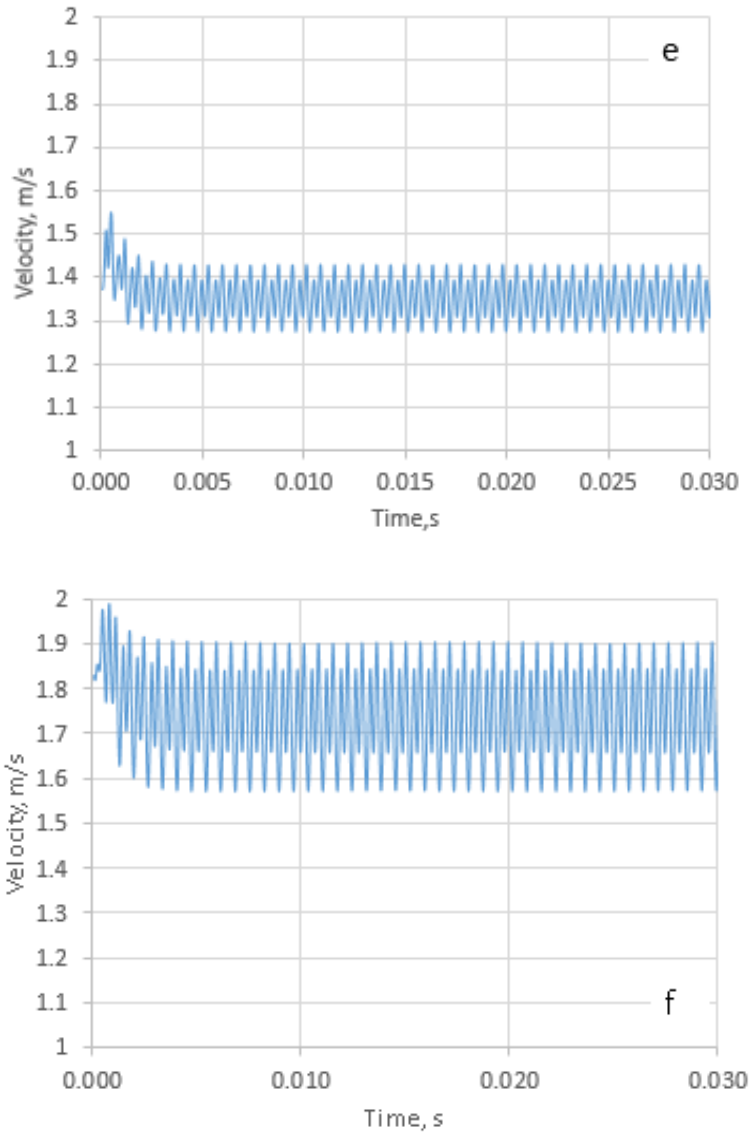

Figure 16 Velocity oscillations; a) Re_D=123, Cμ=10% b) Re_D =200, Cμ=5% c) Re_D =200, Cμ=10% d) Re_D =280, Cμ=3% e) Re_D =280, Cμ=5% f) Re_D =280, Cμ=10%

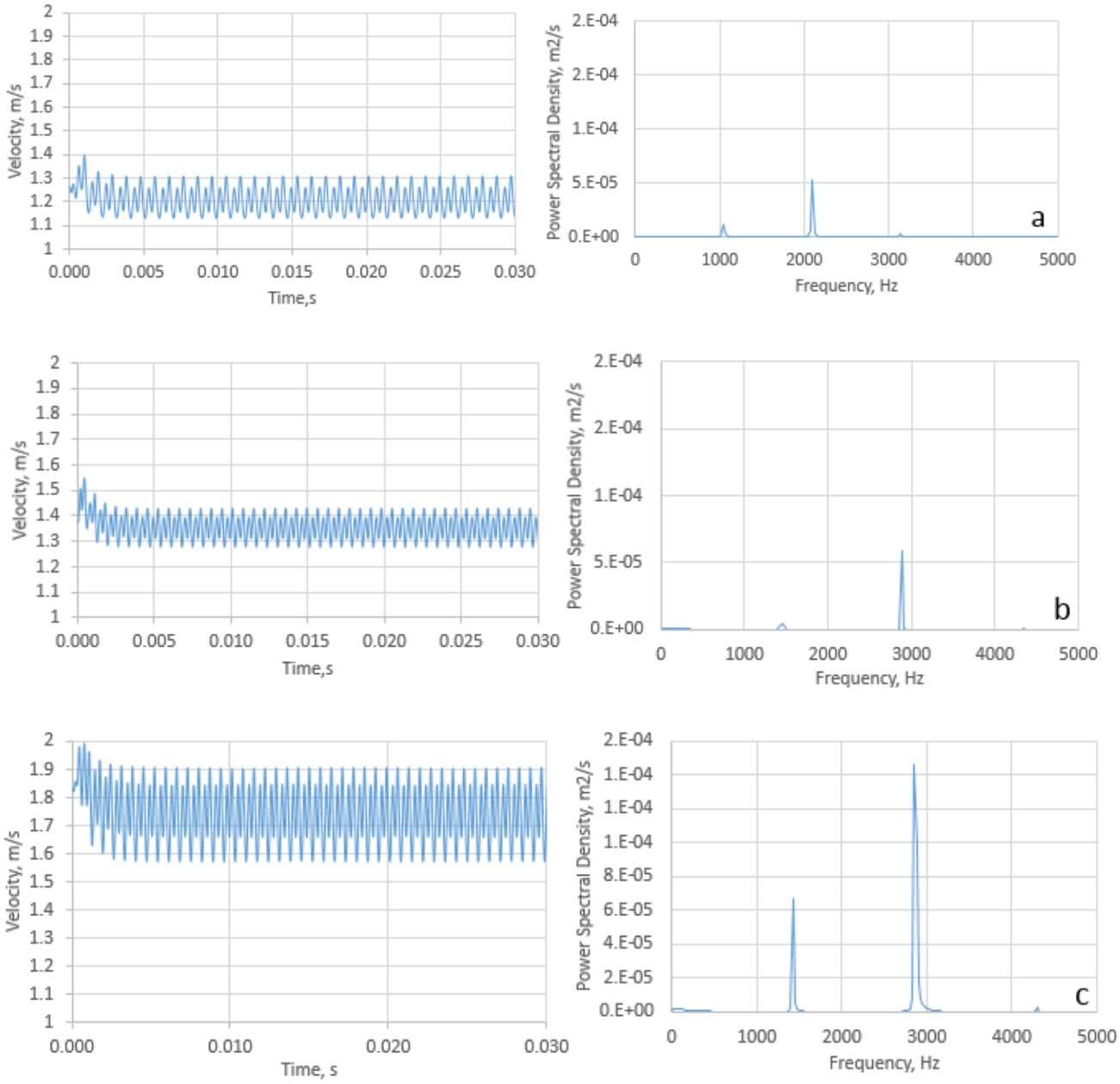

Figure 17 FFT results based on velocity variations for a) Re_D=203, Cμ=10 % b) Re_D=280, Cμ=5 %

c) Re_D=280, Cμ=10 %

Heat Transfer

The distribution of the local Nusselt number along the various lines on the heater is discussed below. The locations of the line probes are shown in Figure 18.

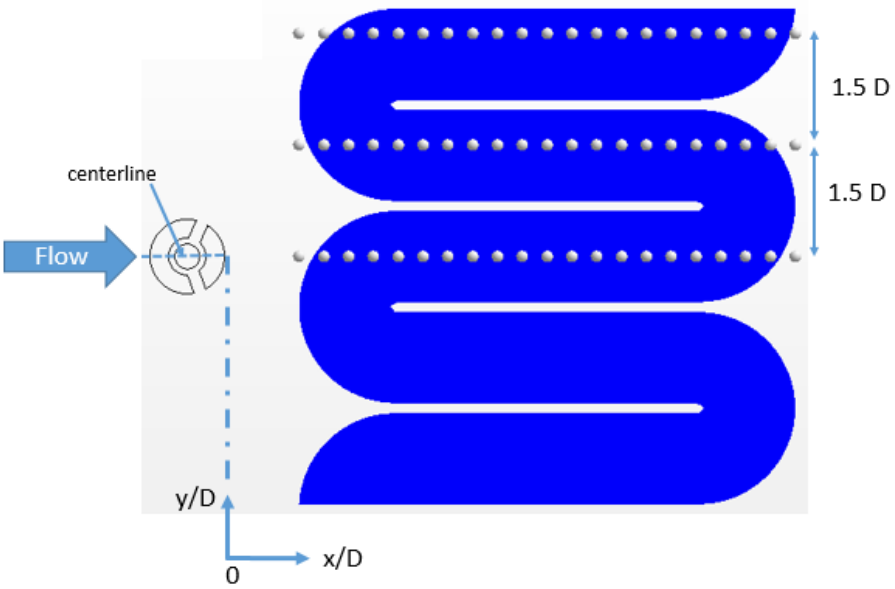

Figure 18 Line probes located on the heater

The behavior of the local Nusselt number downstream of the pillar along its centerline is depicted in Figure 19 for different Reynolds numbers and momentum ratios. For Re_D=123 as the Nusselt number increased with the momentum ratio. The Nusselt number profiles converge after about x/D=5. For higher Reynolds numbers, this heat transfer trend is different. As the momentum ratio increases from 3% to 5% the magnitude of the Nusselt number profile is also increasing. However, after x/d=4.5, it falls below the profile of a 3% case. The same decline occurs at a closer distance, x/d=3.8, for the case with a 10% jet introduction. To further increase in the Reynolds number to 280 results in a steeper

decline at a closer distance of x/D=3.2. This behavior of the local Nusselt number is dictated by the TKE distribution, as shown in Figure 20, which gives the local Nusselt number and TKE behaviors along the centerline for Re_D=280. As the momentum ratio increases, the maximum TKE increases and gradually moves upstream closer to the pillar, after which steeper drop follows. Thus, the TKE profiles can be directly used to estimate the Nusselt number.

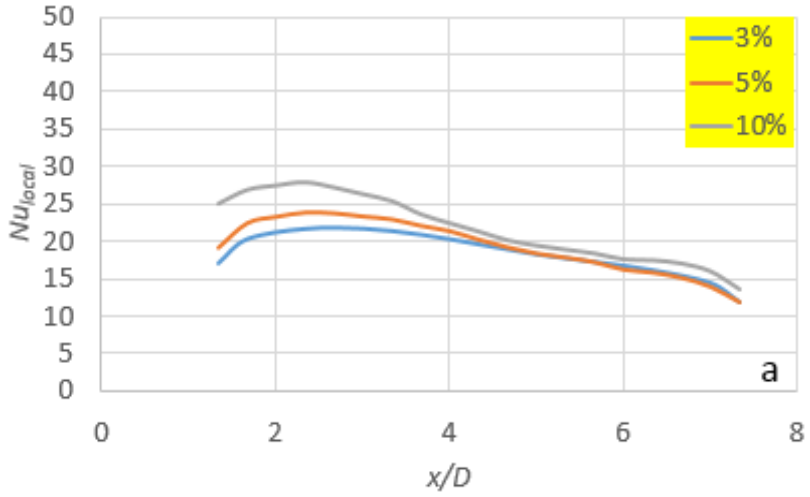

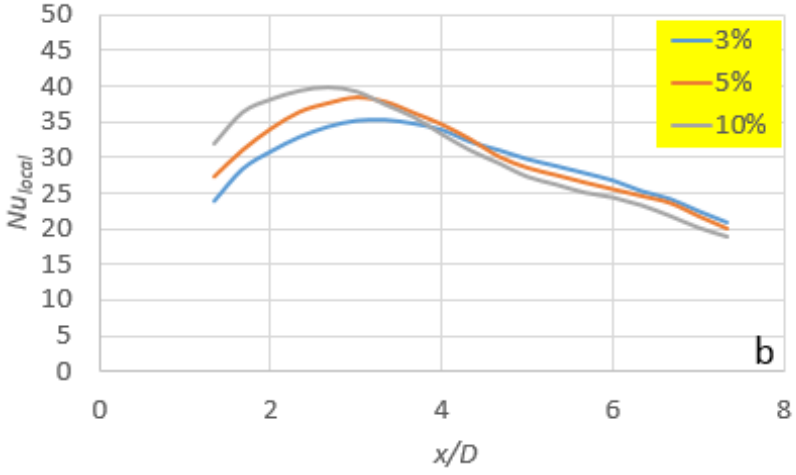

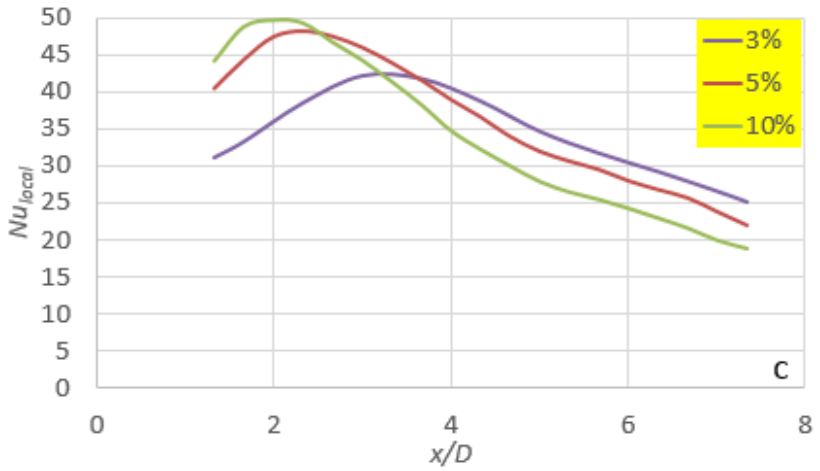

Figure 19 Local Nusselt number distribution along the centerline for a) Re_D=123, b) Re_D=200, c) Re_D=280.

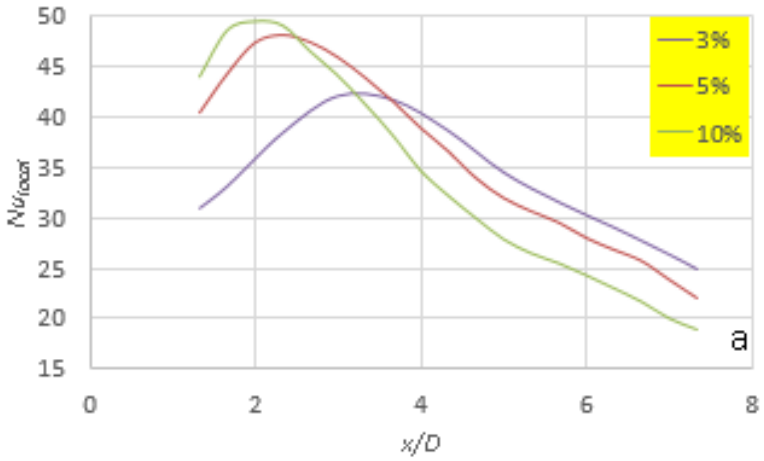

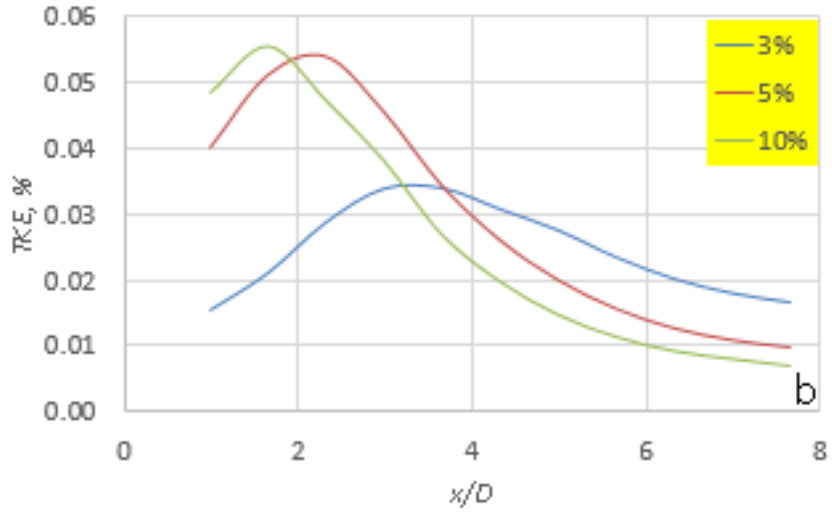

Figure 20 Local Nusselt number (a) and TKE distribution (b) along the centerline for Re_D =280.

The Re_D =280, Cμ=10% case was selected to examine the local Nusselt number variation at different probe lines on the heater. Figure 21 shows the local Nusselt number distribution along the lines located at the centerline, which corresponds to y/D=0, y/D=1.5, and y/D=3. As y/D increases, the profiles are developing in the lower heat transfer coefficient range relative to the centerline. It is believed that the blocking mechanism created against the mainstream flow via jet introduction is responsible for this effect. Moreover, the jets are responsible for the stationary vortex regions on the sides of the heater region, where the heat transfer coefficient decreases. These stationary vortex regions move away from the centerline in the transverse direction as the momentum ratio increases for the constant Reynolds number seen in Figure 6 and Figure 7.

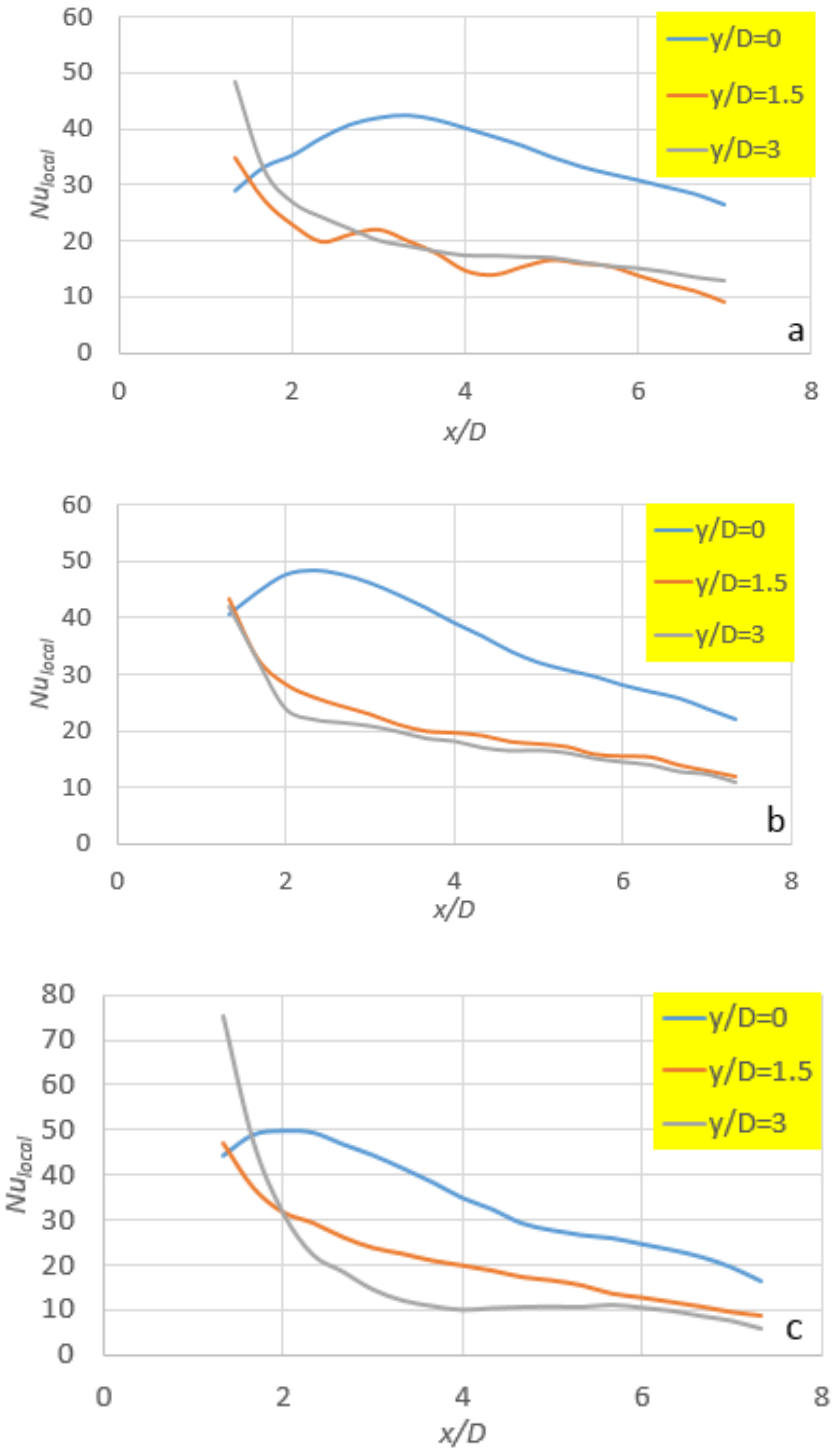

Figure 21 Local Nusselt number distribution at various lines for ReD =280, Cμ=10%

2.1.3. Summary

This study provides insight into the hydrodynamics and heat transfer processes inside microchannels with a pin fin, which are not observable during the experiments. Conjugate heat transfer model approach employed and Star CCM commercial CFD software was used to simulate previously obtained experiments. Laminar and Gamma ReTheta transition models were used to predict the flow behavior over the pillar together with a jet introduction. It was concluded that the model used in this study is capable of predicting both phenomena. The main outcomes of the study are summarized below:

- Jet's introduction to the mainstream might cause the flow to be unsteady, depending on the mainstream Reynolds number. It was found that as the Reynolds number increased for the same momentum ratio, the main vortex shedding frequency, and its amplitude increases, whereas only amplitude gain was observed when the momentum ratio was increased for constant Reynolds number. For higher Reynolds numbers, less momentum ratio is needed to obtain sustained unsteadiness.
- Turbulent kinetic energy profiles provided by the experimental µPIV procedures are important to estimate the turbulence intensity values at the boundary conditions for the transition model. Moreover, TKE values directly dictate the local Nusselt number profiles on the heater. Thus, with only the TKE results, the local variation/profile of the heat transfer parameters can be predicted.
- Jet's introduction to the flow creates a blockage mechanism against the mainstream flow. This, in turn, creates a stationary vortex region leading to hot spots on the heater. As the

momentum ratio increased the stationary vortex regions, essentially hot spots were moved away from the centerline of the heater transversely to the direction to the flow.

This study demonstrates that numerical simulations can provide insight into the hydrodynamics and heat transfer phenomena inside miniature devices, where measuring techniques are very limited. Therefore, future work will include performing numerical studies with different geometries.

2.2. Hydrofoil in crossflow

2.2.1. Experimental Setup and Numerical Model

A microdevice used in experiments of Parahovnik [99] consists of a flow channel that is made of SU-8 and sandwiched between two Pyrex layers, as seen in Figure 22. Fluid conduit has a depth of 0.2 mm, whereas Pyrex layers are 0.5 mm. The width of the flow channel is 1.5 mm, whereas the length is 22 mm. Symmetrical hydrofoil has a 0.15 mm leading edge diameter. Also, as seen in Figure 22, the shape of the hydrofoil is defined by the intersection of the two tangential lines at the point on the centerline of the leading edge circle and 0.25 mm away from the center, hence making the overall chord length 0.38 mm. There are four working RTDs located in the downstream wake region of the fin, of which RTD 2, 3 & 5 are aligned with the center of the fin, and the RTD 6 is located at 0.15 mm offset from the centerline. There is an artifact created during the fabrication at the upstream location of the pin fin, which is ~3.5 times larger than pin-fin in diameter. Geometrical dimensions of the artifact were deducted via image processing of the pictures taken during the experiments, as shown in Figure 23.

Simulations were performed using a commercial code, Star CCM+®. Fluid and solid regions were reproduced in CAD software using original microdevice design dimensions. The polyhedral mesh

was used throughout the whole domain as it is the most efficient element type to be implemented in conjugate heat transfer studies [94,100]. The model consists of three solid and one fluid region as seen in Figure 23.

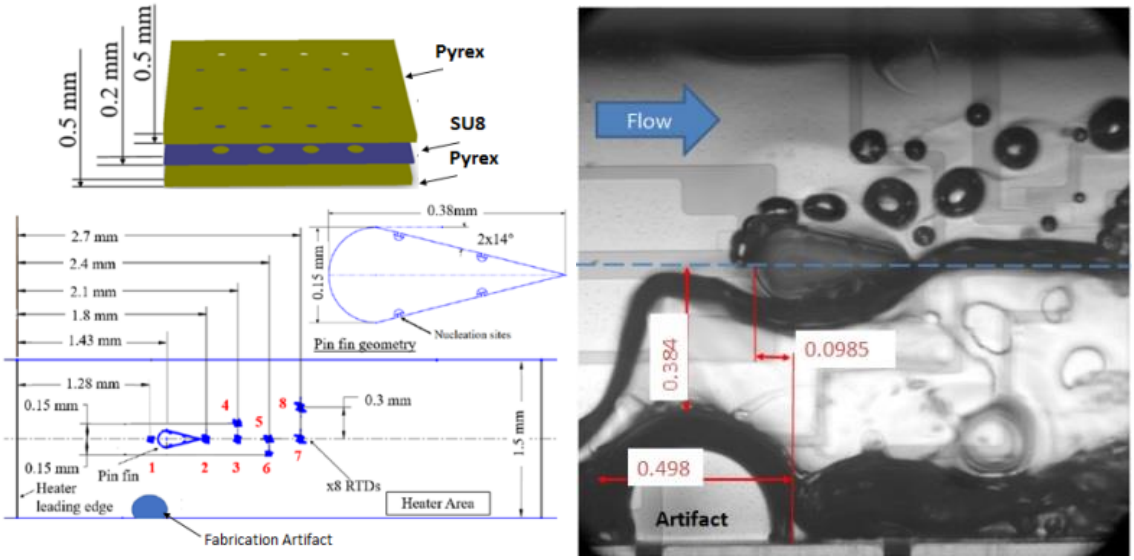

Figure 22 Device and channel details [99]

Twelve in-place interfaces connect all the regions having 99% mesh conformity across them. The refined mesh was created downstream of pin fin and artifact. As seen in Figure 24, it was expected due to the presence of the artifact the flow will not be symmetric which is why additional mesh refinement was performed to connect the two wake regions.

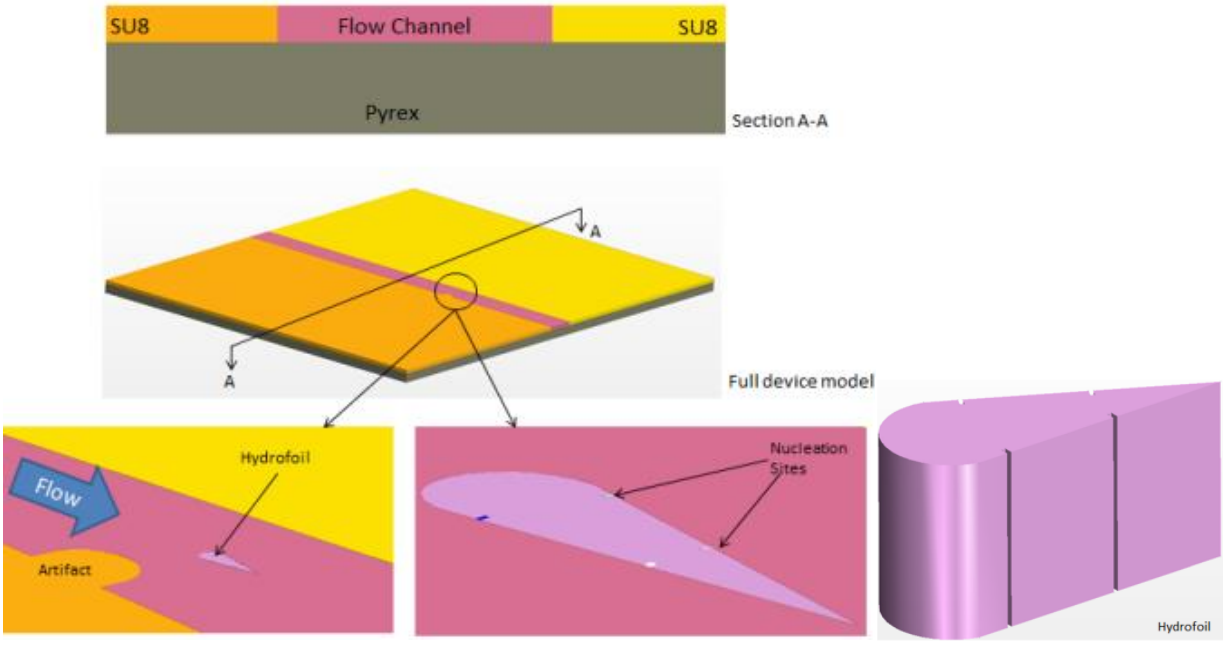

Figure 23 Details of numerical domain

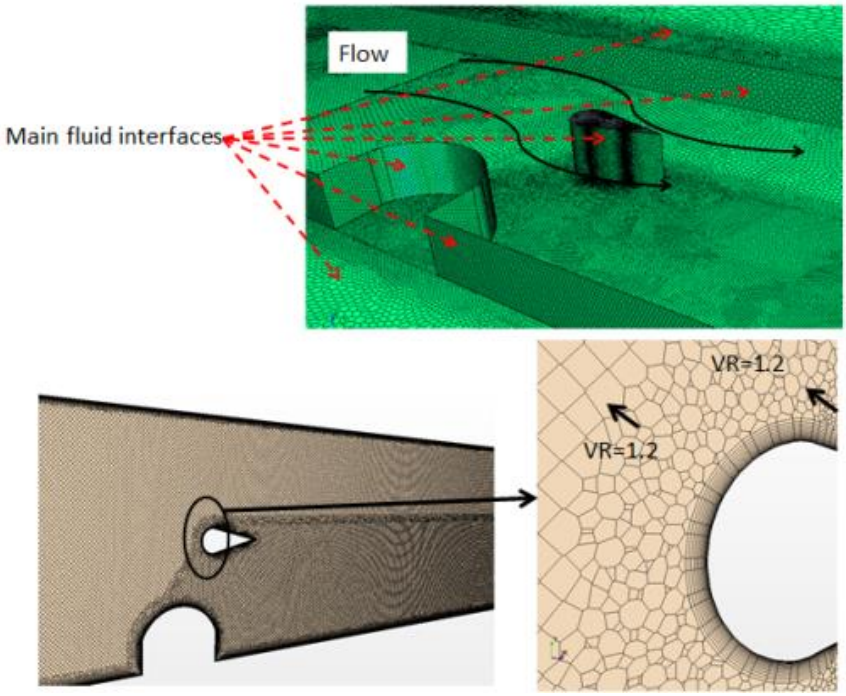

Figure 24 Mesh Details. Volume Ratio (VR) is 1.2

HFE 7000 was used as a working fluid with temperature-dependent properties. The available models from Star CCM+® were used implementing the governing equations 4-7.

Turbulence Model

An appropriate turbulence model has been selected via the iterative approach. Lag Elliptic Blending (EB) k-epsilon turbulence has been proved to predict the flow field well for separated and unsteady flows via overcoming the over-prediction of k [94]. Before applying the above-mentioned turbulence model, a sensitivity study has been conducted for comparison purposes. For the mass flux of G=1778 kg/m^{2}s, the highest mass flux for which experimental data is available, temperature values of RTD2, and RTD3 have been compared against experimental value. As shown in Table 2, out four turbulence models applied, the Lag EB k-epsilon turbulence model performed the best. Therefore, in all the simulations Lag EB k-epsilon model has been implemented. As RTD2 & RTD3 are right behind the pin-fin encountering the trailing edge stagnation region, which is one of the flow types that turbulence models have a hard time predicting, only their temperatures are compared for brevity. The relatively coarser grid has been used in the study which is why differences between the experimental and numerical temperatures are high.

Grid Independence

As seen in Table 3, three different grid sizes have been used in the grid independence study. The baseline element size of 0.05 mm resulted in approximately 1.5 million cells. Further refinement has been performed by decreasing the cell size in half at each step, together with optimized wake region cell count. Even though the case with 11 million cells performed better, 3.2 million cell counts

have been selected for the simulations presented in this paper considering a very slight change in temperature values and 3.4 times faster computation time relative to 11 million cell count.

Unsteady and steady simulations have been performed, and RTD temperature values were compared for a mass flux of G=1778 kg/m^{2}s. It turned out that there is only 3% difference between the temperature readings between unsteady and steady cases. Therefore, steady simulations were used for the purpose of verification.

Table 2 RTD values with different turbulence models

	RTD2, ^{0}C			
	v2f	lowRe k-ε	lagEB-k-ε	AKN
Numerical	39.32	39.05	38.95	39.41
Experimental	31.39			
Δ	7.93	7.66	**7.56**	8.02
	RTD3, ^{0}C			
	v2f	lowRe k-ε	lagEB-k-ε	AKN
Numerical	34.78	35.32	33.07	34.97
Experimental	30.9			
Δ	3.88	4.42	**2.165477**	4.063

Table 3 RTD values with different grid structure

		RTD2, ^{0}C	RTD3, ^{0}C	RTD5, ^{0}C	RTD6, ^{0}C	CPU time, s
	Experimental	51.23	52.57	53.70	54.87	0
Cell count	10987311	52.32	53.34	54.25	53.35	671195
	3161433	52.44	53.48	54.4	53.78	199416
	1427101	55.23	56.57	57.70	57.37	96145

2.2.2. Validation Results

CFD Verification

RTD temperatures were the only parameter measured during the experiments. Therefore, to be able to explore the heat transfer phenomena in the device reliably, RTD temperatures were read from a numerical model and compared to experimental ones, Figure 25. All the temperature measurements were verified successfully. The largest differences were observed in RTD 6 as it resides at the section of the flow channel where two wake regions interact with each other. Steady simulations were not able to capture all the details of this interaction leading to relatively higher temperature differences. Interestingly for RTD 6, for lower mass fluxes, the numerical model under predicts the experiments, whereas vice versa is true for higher mass flux values. The effect of interaction between two wake regions, at higher velocities, on local temperatures could be studied via detailed unsteady study.

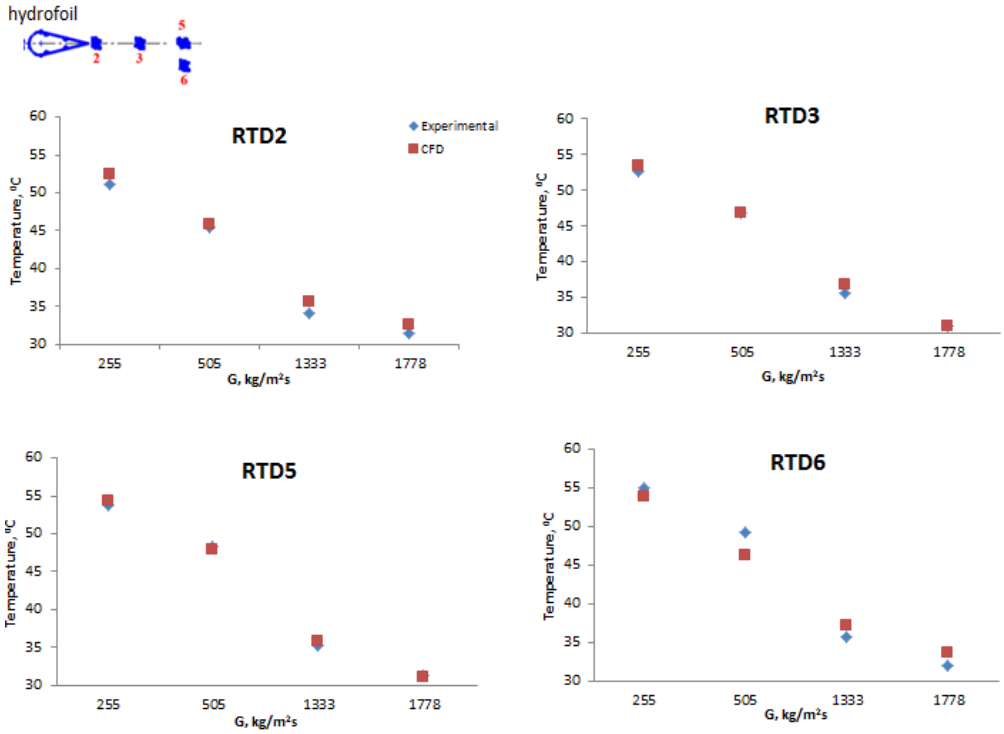

Figure 25 RTD temperature comparison

Solid Thermal Conductivity Effect

One of the main aspects affecting the characteristics of the heat transfer in microdevice is the thermal conductivity of the solid it is made of, specifically the solid part that is attached to the heater. Therefore, to reveal this effect, additional simulations have been performed with exchanging Pyrex and SU-8 solids with silicon counterparts. Silicon was chosen because of its usual usage during device microfabrication processes and O (2) relatively higher conductivity. Figure 25 depicts RTD temperatures for additional cases of silicon for the corresponding mass fluxes. It is obvious that for the same operating conditions, local temperatures are lower than the values obtained using original device solid type. To further investigate this behavior, the difference between temperatures obtained from two different solid structures was calculated as $\Delta T = T_{RTD,\ pyrex} - T_{RTD,\ silicon}$ and has been shown in Figure 26. The difference in temperature tends to decrease as the mass flux increases. This

is directly because of increasing fluid heat transfer capacity which results in weaker conjugate effects. Also, it should be noted that the ΔT asymptotically reaches ~2^0C after G=7112 kg/m2s, claiming that the local temperatures are independent of the solid type at this level of the mass fluxes. As an additional scope to this study, mass flux ranges could be extended, and appropriate correlations could be deducted to assist the design processes of devices operating at high mass fluxes.

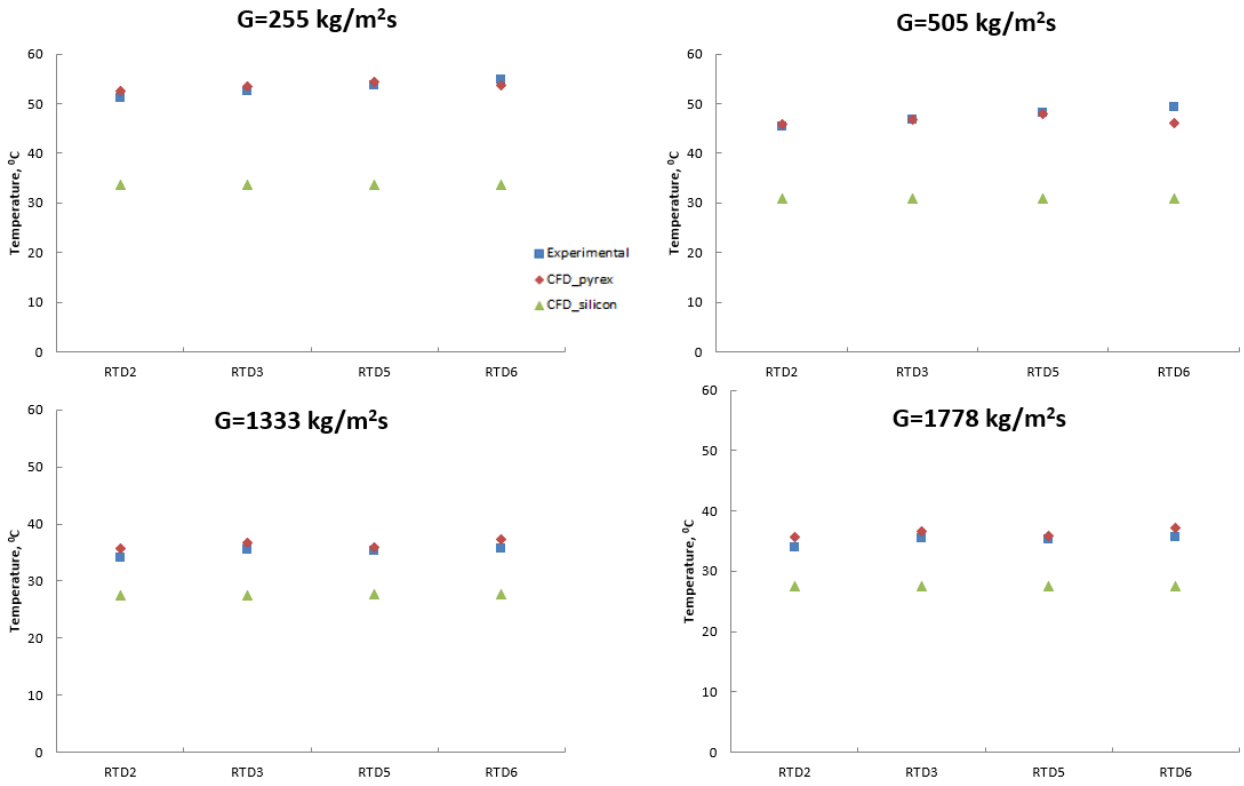

Figure 26 RTD Temperature comparison for different solids

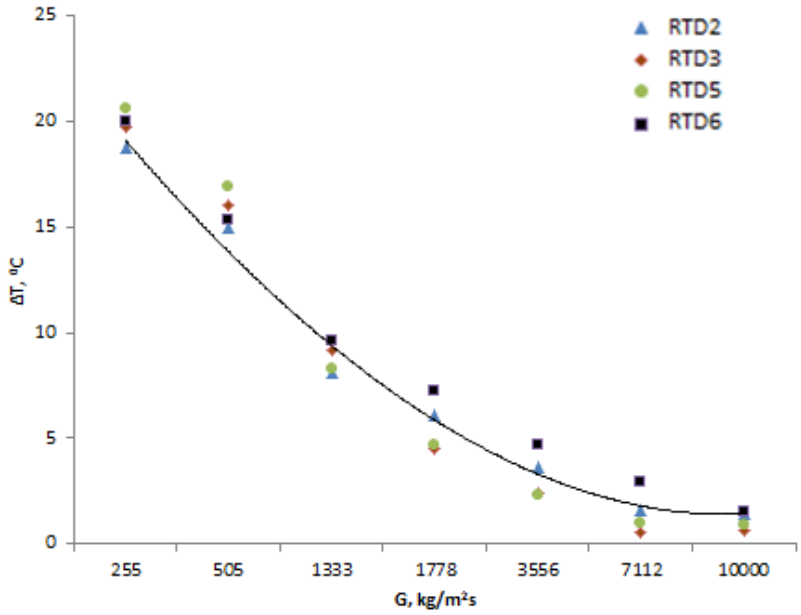

Figure 27 ΔT of RTDs between different solid types

Figure 28 shows how the trade-off between solid and fluid layers is being affected by solid thermal conductivity for the same mass flux. Specifically, in the example of Pyrex-SU-8 and silicon configurations, this trade-off is almost symmetrical. For instance, the amount of heat transferred to the fluid region in Pyrex & SU-8 case is almost equal to the heat absorbed by silicon type solid, for G=255 and 505 kg/m^{2}s. For the latest two mass flux values, the symmetricity between heat transfer magnitudes is disappearing which is due to increased instability in the flow structure, which could be revealed out via unsteady simulations. This behavior is also because the heater is sandwiched between the solid and fluid regions in this microdevice design. For instance, this kind of behavior would not be expected in the microdevice design used in experiments of Woodcock [101], where the heater is at the bottom of the device, and the conjugate effects are more pronounced.

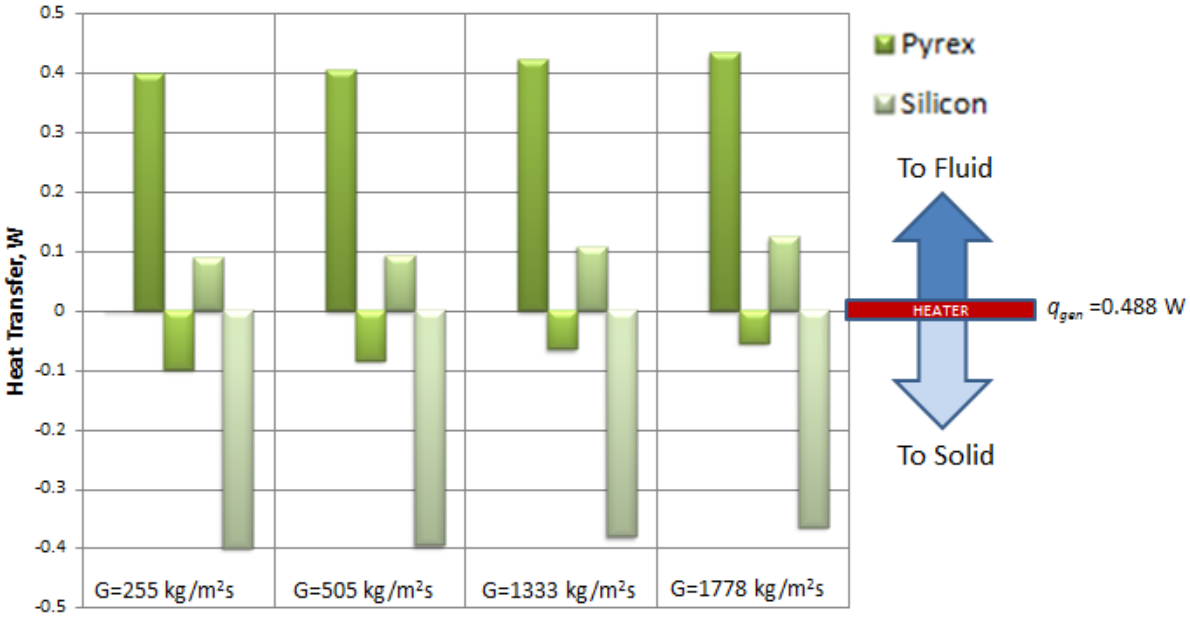

Figure 28 Heat transfer distribution from the heater surface for different solid types

Figure 29 shows the thermal boundary layer development differences. The numerical data was taken at the centerline of the flow conduit. For the case with silicon base solid, the centerline temperature of the fluid is pretty much uniform, with a very slight increase at the leading of the heater, over the whole length of the channel for all the mass fluxes. For the case with Pyrex base solid, higher thermal gradients are visible over the length of the heater resulting in higher average heat transfer coefficients. Also, for higher mass fluxes, the instability of the wake region is translated to valleys on the temperature profile which also gets stronger as the mass flux increases. This is due to the longer length of the stagnation region at the trailing edge at higher mass fluxes. Figure 29 is specifically crucial for the optimization of the heat transfer coefficient and fluid operating temperature in microdevices.

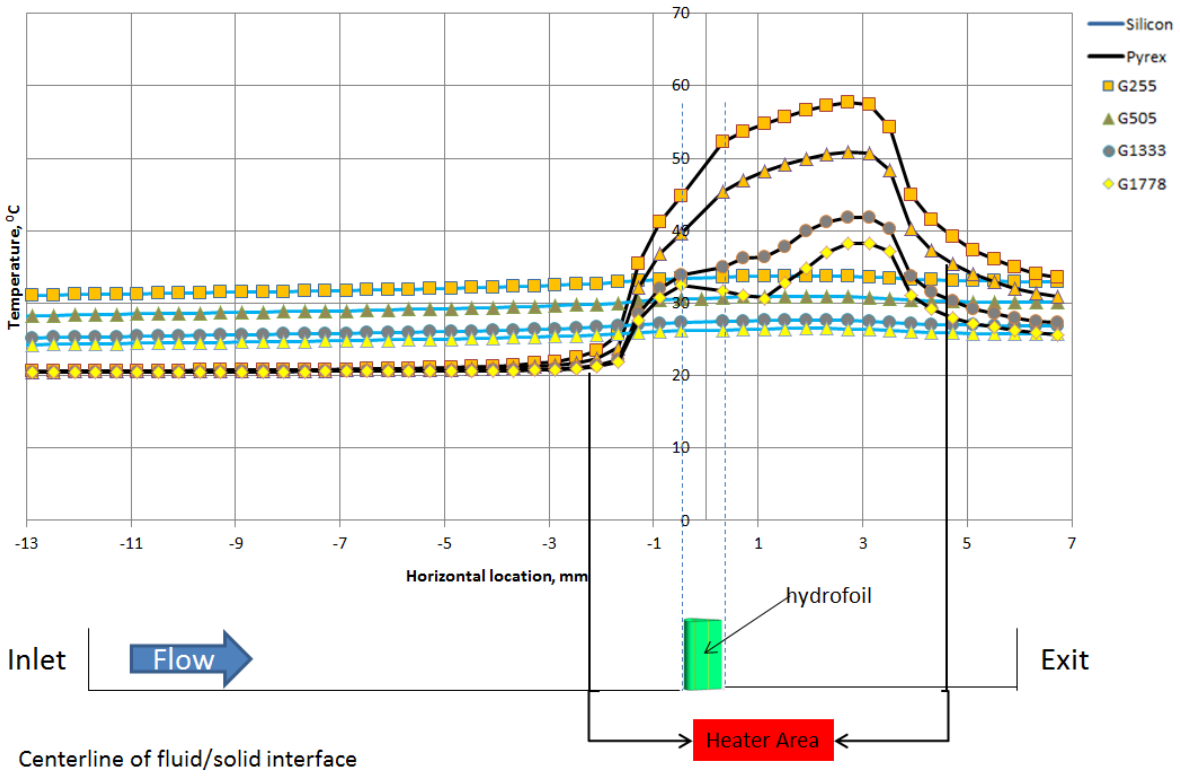

Figure 29 Thermal boundary layer development for two different solid types corresponding to 4 mass fluxes.

2.2.3. Summary

Numerical simulations have been performed to further investigate the heat transfer phenomena in a microdevice tested by Parahovnik [99]. The used CFD model predicts the RTD temperature measurements very good. Simulations were extended to different solid types and differences were discussed. The main outcomes of the study are below:

- The Lag EB k-epsilon turbulence model is in agreement with experiments.
- The conjugate dependency of local surface temperature tends to decay as the mass flux increases, making the solid thermal conductivity less important in microdevice designs

- Thermal boundary layer development and heated entrance length are strongly dependent on the solid thermal conductivity.

Ongoing studies are concentrated on the unsteady simulations to reveal the heat transfer coefficient variation depending on the wake instabilities. Also, this verification study will serve as a baseline for future microdevice optimization studies.

CHAPTER 3. OPTIMIZATION METHODS AND GEOMETRY PARAMETRIZATION

3.1. Geometry Parametrization

3.1.1. Single Hydrofoil Parametrization

This section mainly discusses how the hydrofoil geometry that has been used in experimental studies is parametrized to serve the optimization efforts. As mentioned in chapter 2, the hydrofoil that is studied experimentally consisted of half-circle as leading-edge geometry and two straight lines used for closure to obtain the desired chord length, which was 375 µm. To provide enough freedom during optimization efforts, the hydrofoil geometry was divided into three parts, as seen in Figure 30. Ellipse was fitted to leading of the hydrofoil, whereas closure is obtained through two identical 3rd-degree polynomials. The parameterization method applied to each section is discussed below. The Python code has been developed providing the parametrized geometries.

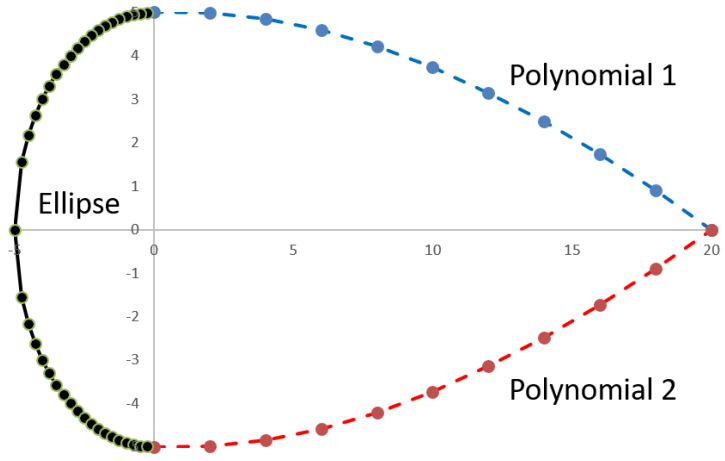

Figure 30. Hydrofoil shape in terms of polynomials and an ellipse

Ellipse:

The governing equation of ellipse was taken as a starting point for the parametrization, (12. To be able to build desired leading-edge ellipse, user inputs;

- ✓ the center of the ellipse relative to the cartesian coordinate system,
- ✓ the number of points defining the resolution of the ellipse curve,
- ✓ the angle of attack, α, which measured from y=0 line in the same coordinate system,
- ✓ A and B values as in (12.

Based on the origin location relative to the coordinate system, the number of points desired, and A value as in (12, each x point has been calculated. Afterward, each y point corresponding to x point was determined using (12. As the aim of the parametrization was to create hydrofoil geometries with different angle of attacks, each x and y point was related to the α via (13 and (14.

$$\frac{x^2}{A^2} + \frac{y^2}{B^2} = 1 \tag{12}$$

$$X = x\cos\alpha - y\sin\alpha \tag{13}$$

$$Y = y\cos\alpha + x\sin\alpha \tag{14}$$

As a result, different sized and oriented ellipses were created, as shown in Figure 31. It should be noted that 50 points have been used to create the ellipse curves shown in Figure 31.

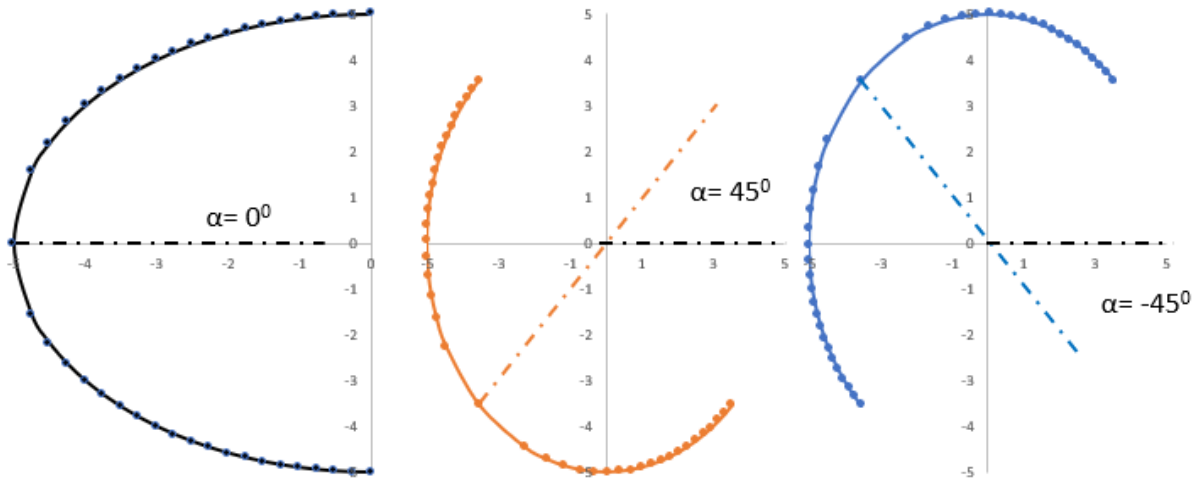

Figure 31. Ellipse configurations corresponding to the different angle of attacks

Polynomials:

As shown in Figure 30, the 3rd-degree polynomial has been fitted to the hydrofoil geometry and governed by (15. The coefficients a1, a2 and a3 were calculated based on the boundary conditions listed below and shown in Figure 32.

<u>Boundary conditions calculated within the code:</u>

- ✓ The last two points of the ellipse curve, where the polynomials and ellipse intersected, were used to calculate the slope, k1. This slope serves as the first boundary condition to the polynomial and ensures the perfect match between ellipse and polynomial curves.
- ✓ The coordinates of the last ellipse point from which the k1 slope has been calculated coincide with the first point of polynomial, as x1 and y1.

Boundary conditions based on user input:

- ✓ A user inputs the desired chord length, and the code calculates the x2 point of the polynomial curve based on that length, origin coordinates, and A from equation 1.
- ✓ Y_{end} parameter is another input from the user that defines the y2 of the polynomial. This is one of the main parameters that define the orientation of the hydrofoil.
- ✓ Lastly, k_2 slope is user input defining the slope at the closure point of the hydrofoil.

It should be noted that the above-mentioned parametrization procedure is repeated for each polynomial curve separately, within the code.

Using the above-mentioned parameters, (16, (17, (18 and (19, coefficients a1, a2, and a3 have been calculated, and polynomial equation became ready for the hydrofoil geometry parametrization.

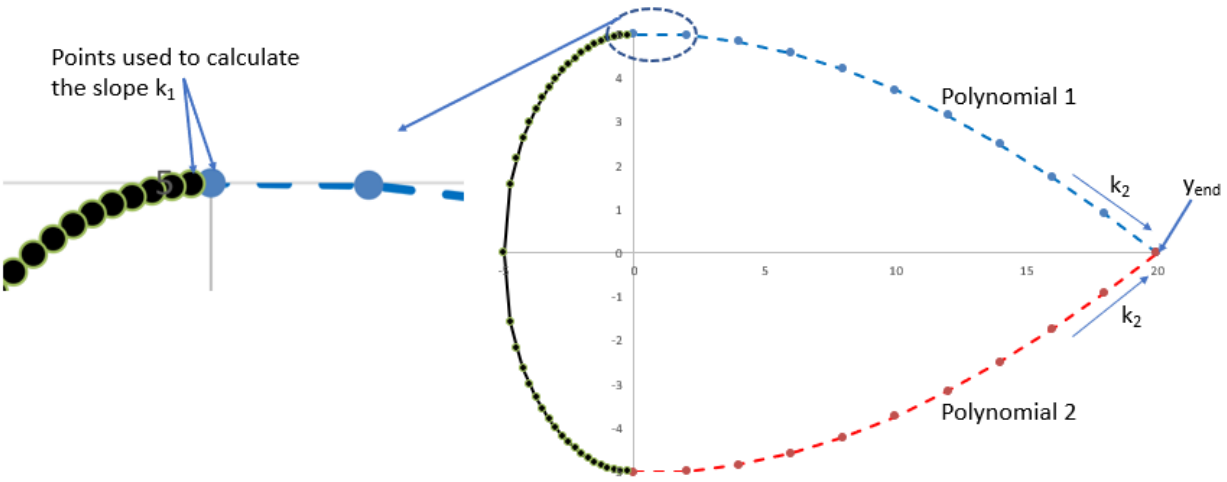

Figure 32 Details of constraints between ellipse and polynomials

$$y = a_3x^3 + a_2x^2 + a_1x + a_0 \tag{15}$$

$$a_3 = \frac{(k_1 + k_2)(x_1 - x_2) - 2y_1 + 2y_2}{(x_1 - x_2)^3} \tag{16}$$

$$a_2 = \frac{-k_1(x_1 - x_2)(x_1 + 2x_2) + k_2(-2{x_1}^2 + x_1x_2 + {x_2}^2) + 3(x_1 + x_2)(y_1 - y_2)}{(x_1 - x_2)^3} \quad (17)$$

$$a_1 = \frac{-k_1(x_1 - x_2)(x_1 + 2x_2) + k_2(-2{x_1}^2 + x_1x_2 + {x_2}^2) + 3(x_1 + x_2)(y_1 - y_2)}{(x_1 - x_2)^3} \quad (18)$$

$$a_0 = \frac{x_2(x_1(-x_1 + x_2)(k_2x_1 + x_2k_1) - x_2(-3x_1 + x_2)y_1) + x_1^2(x_1 - 3x_2)y_2}{(x_1 - x_2)^3} \quad (19)$$

Figure 33 depicts the reaction of the hydrofoil geometry to change in various main parameters where section a is the baseline geometry with the same dimensions as in experimental setup. Section b of the same figure shows hydrofoil with $+30^0$ angle of attack. Hydrofoil geometry generated with relatively higher k2 value for one of the polynomials is shown in c section of Figure 33 whereas d section of the same figure depicts hydrofoil geometry with y_{end} being not equal to 0. It should be noted that these are not the only parameters that changed during optimization, but the main ones that drive geometry boundaries together with the dimensions of the ellipse.

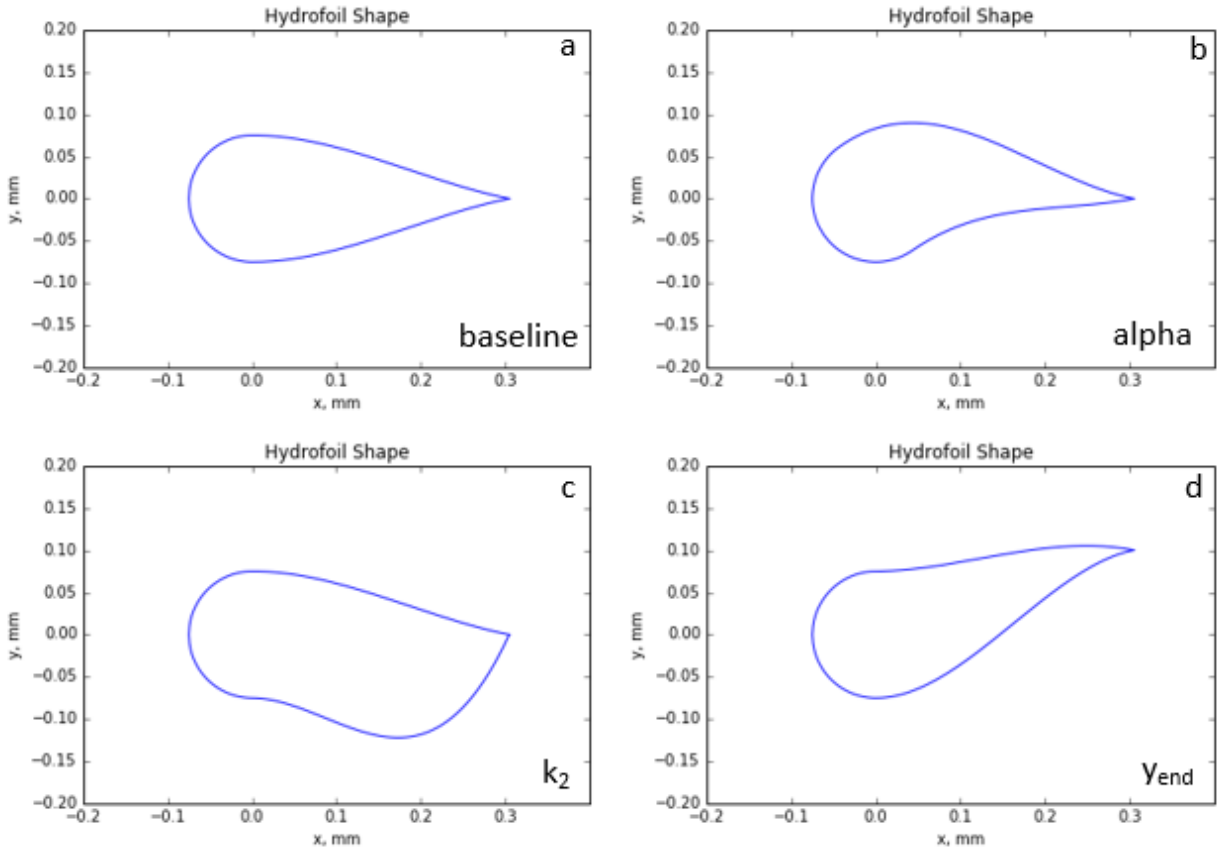

Figure 33 Hydrofoil shapes with different geometric parameters

3.1.2. Single Hydrofoil with Satellites Parametrization

To extend the scope of the optimization, additional satellites were added to channel around the main hydrofoil. These satellites are designed to have smaller dimensions than the main hydrofoil, while parameters are calculated in the same manner as the main hydrofoil. The algorithm for creating these satellites is clarified in the below steps and depicted in Figure 34.

Parameters based on user inputs:

- ✓ Main input is the offset dimension, which defines how far away the satellite is desired to be located relative to the main hydrofoil.

- ✓ The dimensions of the satellite hydrofoil must be input as for the main hydrofoil, see Section 3.1.1.
- ✓ The orientation of the satellite hydrofoil will be defined by the angle γ, which defines the deviation of the chord of hydrofoil from the satellite orbit.
- ✓ The number of the desired satellites which is limited to two in this application, but the code could be updated to provide more satellites

Parameters calculated within the code:

- ✓ Firstly, the incremental slopes between each point, as seen in Figure 30, of the hydrofoil are calculated
- ✓ The offset dimension entered by the user is used as the magnitude of the vector along which each point is transferred to create the satellite orbit. Also, slopes used in the calculation, ensuring parallelism. Satellite orbit only serves to locate the centers of the satellite's ellipse.

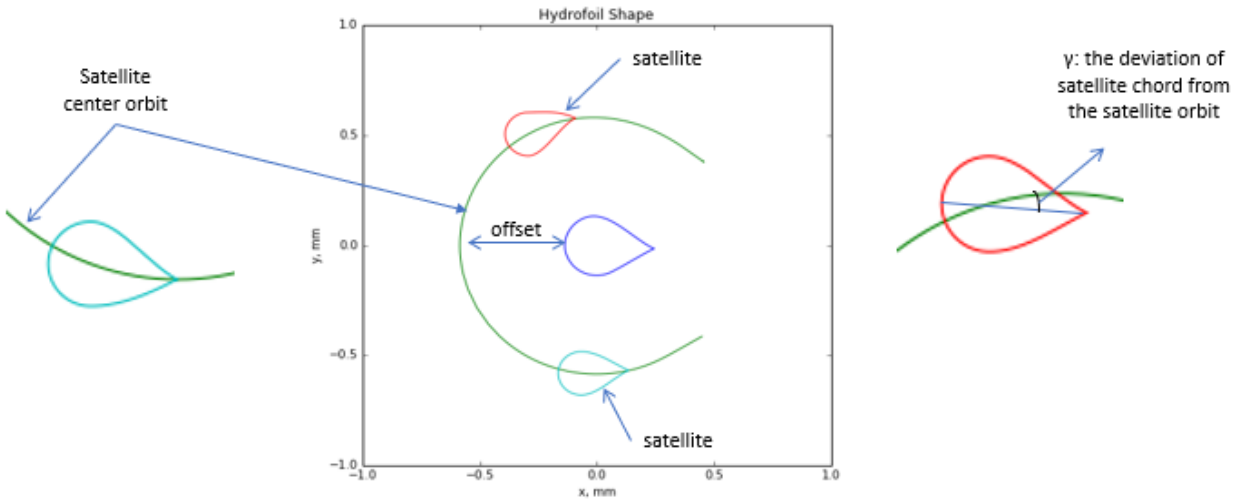

Figure 34 Description of satellites and their center orbits.

Random geometries provided by the codes is shown in Figure 35. The code is capable of parametrizing main hydrofoil and satellites at the same time, increasing the range of the geometries available for analysis, as shown in the first three configurations. However, if desired, the main hydrofoil could be kept constant whereas satellite hydrofoil could be updated to have various shapes. Note that the combination of the changes should be decided based on the available computational resources.

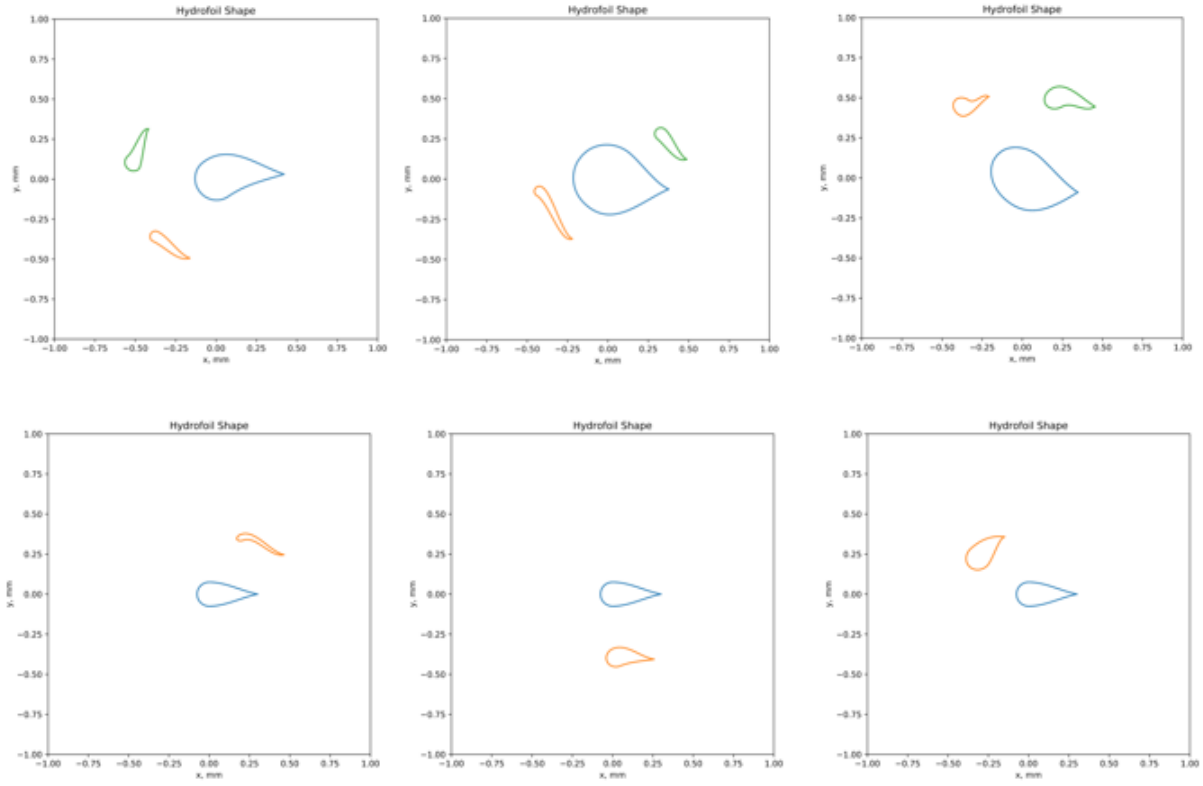

Figure 35 Random satellite hydrofoil geometries

3.2. Optimization and Sampling Methods

3.2.1. Latin Hypercube Sampling

Uncertainty and sensitivity studies are conducted to determine the behavior of numerical models and provide sufficient information about the response characteristics objective function subject to certain input variables. These studies become relevant in recent years due to the increase in the complexity of the numerical models and physical problems represented by them. A sampling of the input variables or internal parameters is performed by implementing Latin Hypercube Sampling (LHS) in this study.

Latin Hypercube Sampling, which is also called Stratified Monte Carlo Sampling, has advantages over other sampling methods when dealing with large sample sizes. For instance, Monte Carlo sampling may require huge computational resources since it utilizes a random sampling approach. Through random sampling approach, for each variable, values are selected aleatory from the cumulated distribution function corresponding to that variable. Hence, to get the reliable response surface of the objective function, the number of sample sizes should be large enough, especially when multivariable problems are considered. Developed by Mckay et al. [104]., the Latin Hypercube sampling method bypasses this issue by forcing each variable selection to be from each interval, defined by the sample size, of the cumulated distribution function. This ensures that the whole range of the probability distribution is represented in the obtained response surfaces.

Consider $f(x)$ which is a function of variables $(X_1, X_2, X_3, \dots . X_k)$, and the aim is to determine how $f(x)$ varies when $X's$ vary according to some probability distribution. LHS method divides each variable's range into n nonoverlapping intervals, and one value from each interval is selected based on the probability density function. To be more specific, consider that X_k has a normal distribution with the available mean and standard deviation. The method first selects n random numbers, $(U_1, U_2, U_3, \dots . U_j)$

from the uniform distribution, i.e., between 0 and 1. Afterward, the cumulative probability P_j is calculated through scaling each random number U_n based on equation 20

$$P_j = \left(\frac{1}{n}\right) U_j + \frac{j-1}{n} \tag{20}$$

Equation 20 ensures that each P_j is located in n^{th} interval. It should be noted that random sampling methods do not implement scaling as mentioned above, it is the benefit of LHS. Once scaled probabilities are obtained, the corresponding z-score values form inverse distribution is obtained. Having mean and standard deviation each X_j value is calculated from the z-score formulation. This procedure is repeated independently for all the input variables of $(X_1, X_2, X_3, \ldots . X_k)$. At the end of the procedure n different values for each variable X_k will be available. The values will be grouped in the clusters such that each variable X_k has its own cluster of size n. This is followed by the pairing process, which constitutes value drawing from each cluster once, resulting in distinct vectors of size k. Therefore, the overall input variable matrix will have a size of n x k [105].

Open source Dakota code has been implemented to perform DOE on the problem of interest. Distributed Design and Analysis of Computer Experiments (DDACE) module, together with LHS, was used through DAKOTA. DDACE DAKOTA allows only uniform distribution of the variables, and no input of correlations between variables are allowed, which fits the requirements of the studies performed in the scope of this document [105]. The representative Latin Hypercube created by the software in the double variable domain is shown in Figure 36. Notice how the variables are selected from nonoverlapping bins.

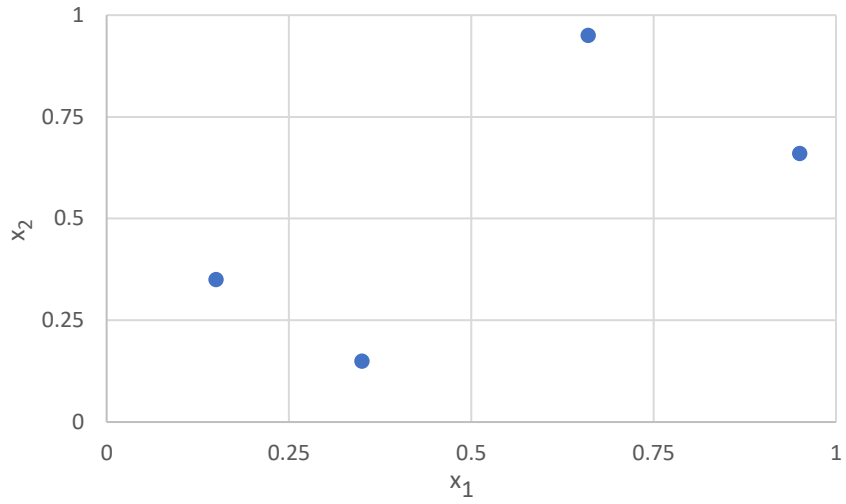

Figure 36 Representative Latin Hypercube

The setup used to perform the design of experiments is below is shown in Appendix A.

3.2.2. Genetic Algorithm

This section discusses the optimization methods used in creating the results presented in Chapter 4.

Optimization algorithms are applied to minimize the defined objective function(s) within the defined design constraints. They could be classified based on methods implemented in searching and finding the global or local optima of the objective function(s). Gradient-based, derivative-free, and surrogate-based minimization are examples of such methods. The optimization problem types, search goal, and search methods usually provide enough information leading to the most appropriate optimization methods selection.

The types of objective functions and constraints used in the optimization problems could have linearity or non-linearity, could be bounded or unbounded, etc., which is used to classify the problem

itself. For instance, the unconstrained problem has no constraints where a bound-constrained problem has lower and upper bounds. The linear-constrained problem may have additional linearity constraints where non-linear constraints may have all the above characteristics in them. The problem that is solved in the scope of this study is the bound-constrained.

The search goal defines the desire of local optima to be found as a result of the optimization, which could be local or global. In global optimization point of interest is the minimum objective function value of the whole design space that is within constraints, whereas local optimization looks for neighboring minimum values. The main difference in applying these methods is arising from the computational cost point of view, as global optimization could be more expensive than local ones. This study will implement global optimization searching for global minima within the provided design space.

The method followed while searching for such minima could be gradient-based or non-gradient based. In gradient-based methods, optimization looks for gradient along which the improvement in the calculated members is available. The drawback of such an algorithm is not only that sometimes computing such gradient could be computationally expensive but also might not be existent. Some local optimization methods utilize the gradient-based approach in searching for local optima. Non-gradient based optimization methods bypass this drawback whose examples are non-gradient based local optimization and non-gradient based global optimization methods. There also surrogate-based optimizations that implement priori defined sample size. This sample is used to train the surrogate model which then drives optimization. The computational run time in surrogate-based optimization modeling could be reduced compared to the latter two methods. Non-gradient based global minima methods will be implemented in this study.

Evolutionary algorithms, such as genetic algorithms, are the type of non-gradient based global optimization methods. Its logic is analogous to the natural selection process in a biological system, e.g., DNA. Each design value is considered in a genetic string (input variable), which then used to create chromosomes (objective function value). Fitness function is then used to decide if the specific value will be used further in the optimization in predicting future members. A genetic algorithm could be single-objective or multi-objective. This study takes advantage of the multi-objective genetic algorithm, and its searching methods are discussed below. The main parameters that define the genetic algorithm are presented below;

- Fitness function for optimization
- A population of chromosomes
- Fitness function criteria that decided which chromosomes will reproduce
- Crossover criteria that identify the next generation chromosomes
- Random mutation of chromosomes in the next generation.

Notice that the terminology is very similar to biological counterparts.

Chromosomes are identical to the input vectors discussed in section 3.2.1. For instance, given input vector;

$$chromosome = V_I = (X_{1i}, X_{2j}, X_{3t}, \ldots . X_{kk}).$$

Each variable value, such as X_{2j}, corresponds to a single *gene.* These genes are creating chromosomes. Input vectors are converted to chromosomes via bit strings, which are sequences of 0's and 1's. The sample chromosome of used in solution with six parameters would be like this;

$$chromosome = [110110]$$

The genetic algorithm creates an *initial population* via randomly selected chromosomes. *Fitness function* act as a decider for reproduction. For each member of the initial population, the corresponding fitness function is calculated based on the given direction by the user. Afterward, based on the *selection criteria, the* member would be selected for reproduction. Reproduction happens through two processes whose rates are input by the user.

Crossover operation creates two *offspring* chromosomes from two *parent* chromosomes. Given two chromosomes c_1 and c_2;

$$c_1 = [110110]$$

$$c_2 = [011010]$$

To apply the crossover operation, the user needs to input the *crossover location.* Assuming crossover from 3rd location new offspring chromosomes would look like below;

$$c_{1\_offspring} = [110010]$$

$$c_{2\_offspring} = [011110]$$

Mutation operation flips the individual genes, from 0 to 1 and vice versa, located in the new chromosomes. Noting that, selection and crossover operations sustain the information of the fitter chromosomes relative to generation they are taken from, which might lead to quick convergence, and potentially optimized results would be local optima instead of global. The mutation operator prevents it as it randomly changes the characteristics of the chromosomes subject to rate input by the user. Optimization converges when the changes done to chromosomes do not change outcome within provided convergence level.

The details and inputs to the sample optimization performed and discussed in chapter 4 are presented in Appendix A [105].

CHAPTER 4. OPTIMIZATION RESULTS

4.1. Design of Experiments (DOE)

DOE needed to be performed before the optimization cycle to identify the proper ranges of the geometrical parameters and dependency against the average heat transfer coefficient. The expected outcome from the study is to adjust the parameter ranges such that the whole available design space is covering the global minimum and determine the need for additional parameters. Figure 37 shows the baseline hydrofoil geometry used during experiments and discussed in section 2.2. The parameters that were changed during DOE are as below:

- ✓ Origin=0
- ✓ Chord length as measured from the origin
- ✓ A/chord, A as measured from the origin
- ✓ A/B, B as measured from the origin
- ✓ α, as measured from y=0 line
- ✓ Y_{end}/chord, Y_{end} as measured from y=0 line
- ✓ k_2, equal for each polynomial

Notice that all the parameters, except hydrofoil leading edge angle, was non-dimensionalized against the chord length. The origin, x=0 & y=0, was kept constant. On the of the left of Figure 37 baseline hydrofoil parameters are given. Ellipse parameters, A and B, are equal leading to circular leading edge where α, origin and Y_{end} are aligned on the horizontal x-axis. The second slope of polynomials are equal at 57.3 degrees.

To decrease the computational time and still have enough numerical domain for robust optimization results, the portion of the fluid channel that is right above the heater area is selected, as shown in Figure 38. Note that the hydrofoil area in the baseline case covers only 0.5% of the whole heater area. The ranges of the parameters are set such that the coverage by the newly generated fins is not more 1.5% of the heater. Hence heat flux boundary condition is used, as the heater area is constant among the DOE cases with deviation equal or less than 1%, and the average heat transfer coefficient is calculated over the whole heater area.

The mesh settings discussed in section 2.2 also were replicated here. Fully developed inflow conditions, which are taken from the validated CFD simulations performed in section 2.2., were prescribed at the inlet boundary. This ensured that the hydrodynamically fully developed conditions are available at the leading edge of the heater. The boundary conditions are the same as the baseline in terms of the heat flux. However, from this section on Re number will be calculated based on the channel hydraulic diameter of 0.353 mm as the pin-fin width is expected to change in each DOE simulation.

Parameters:

a=0.075 mm (ellipse)

b=0.075 mm (ellipse)

alpha=0

Origin=0

Chord=0.375 mm

k_2=11.165 rad

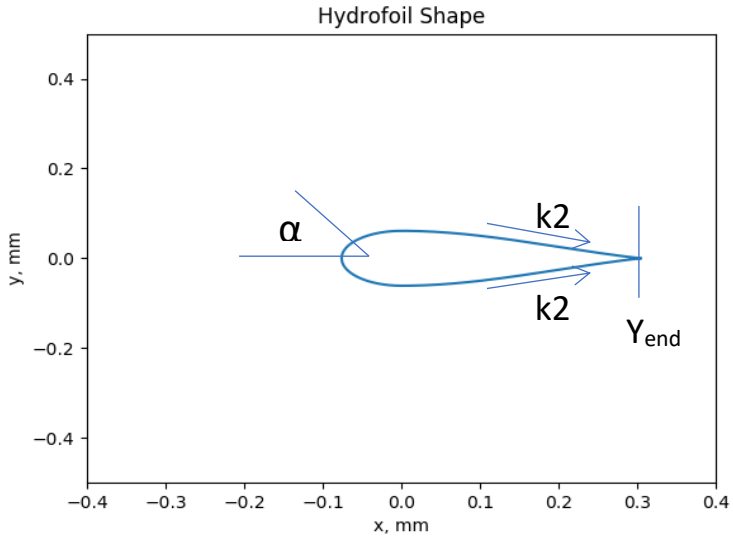

Figure 37 Baseline hydrofoil geometry and parameters

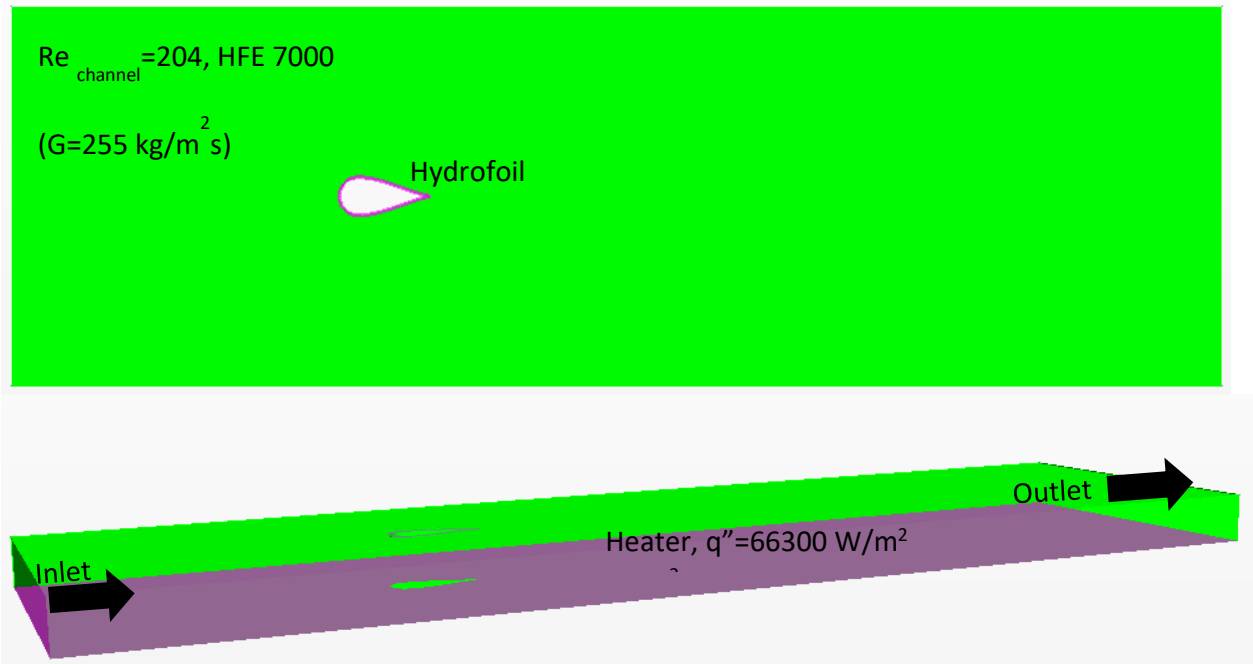

Figure 38 CFD Domain

As discussed in section 3.2., the Latin Hypercube Sampling method has been applied, and out of 150 CFD runs, 135 were converged creating the sample size. It should be noted that there is still a challenge in defining the appropriate sample size prior to the LHS. The effectiveness of the selected sample size could be decided statistically only after the simulations are over, in which case if the results are not satisfactory, a completely new run with an updated sample size needs to be performed [103]. Therefore, as there is rare information in the literature about the sample size to be used in such problems, the sample size was input as 150 for the study. Data acquired after LHS was studied statistically to determine if the sample size was enough to provide satisfactory information on the relationship between average heat transfer coefficient and hydrofoil geometrical variables. The least-squares regression line is fitted on the data obtained from LHS, which is extracted from 135 converged CFD cases.

Figure 39 shows how the average heat transfer coefficient predicted by the regression model correlates with the actual LHS data. Overall, R^2= 84%, implying that the dependencies obtained from this sample could be used in defining the ranges of the optimization cycles.

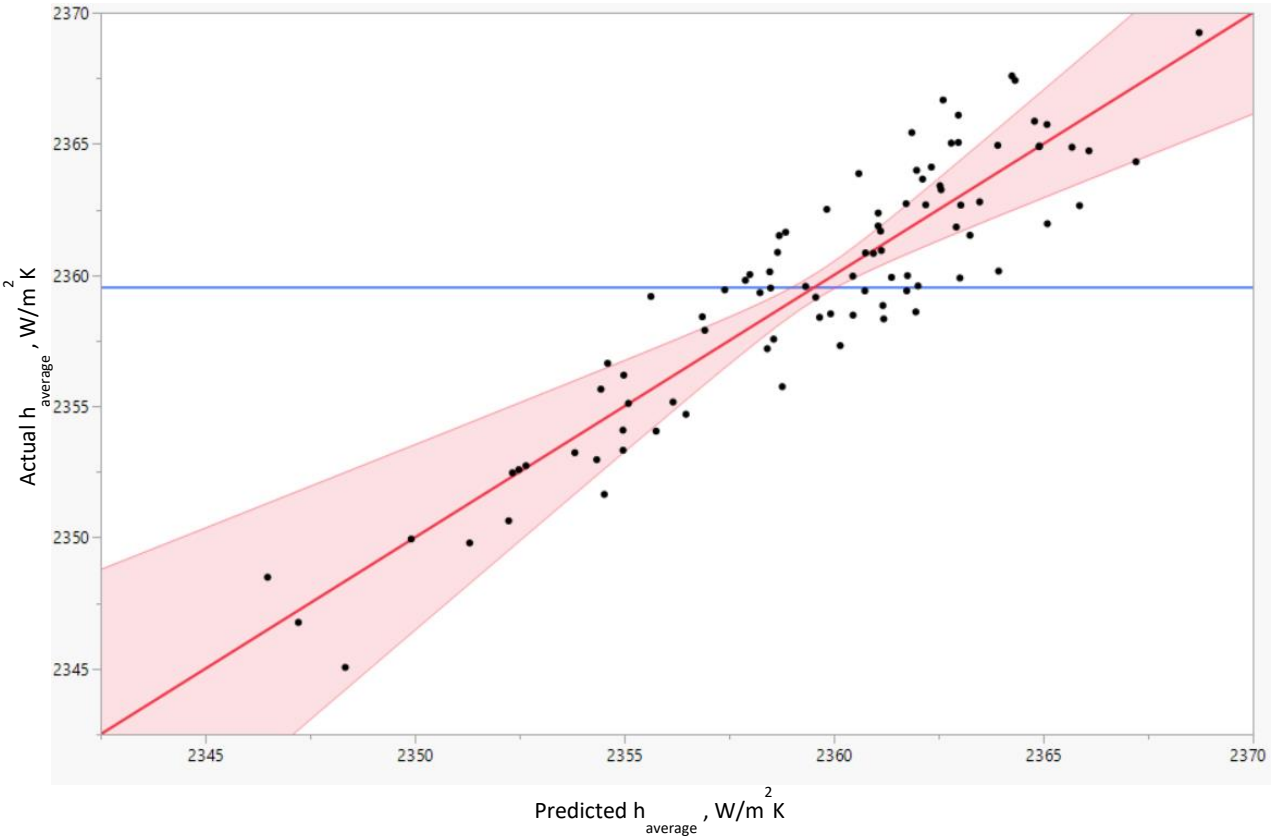

Figure 39 Least squares regression line, R^2=0.84

The average heat transfer coefficient in the domain was analyzed against each parameter. Figure 40 shows that as the chord length increases, there is an enhancement in thermal performance. It should be noted that the lower magnitude increment in average heat transfer coefficient value, which is 50 W/m^{2}K higher than the baseline 2350 W/m^{2}K, is due to relatively smaller Re. The same behavior is also seen in Figure 41, where the change of A is depicted. As A and chord length distance vectors are both starting from the origin, increasing A also contributes to the true chord of the hydrofoil, enhancing the

overall thermal performance. The slopes of the best line arrows in both figures are almost identical. Figure 42 shows the dependency on the leading edge angle, α. As the hydrofoil origin was kept constant, due to symmetricity of the flow channel no matter the sign of the leading edge angles, the magnitude of enhancement does not change, leading to almost parabolic-like behavior. Average heat transfer coefficient increases with an increasing absolute value of leading edge angle. Based on the information shown in the last three figures, the ranges of the chord length, leading edge angle, and A/chord ratio should be kept at the feasible maximums during the optimization cycle in order to capture higher thermal performance regions of the design space.

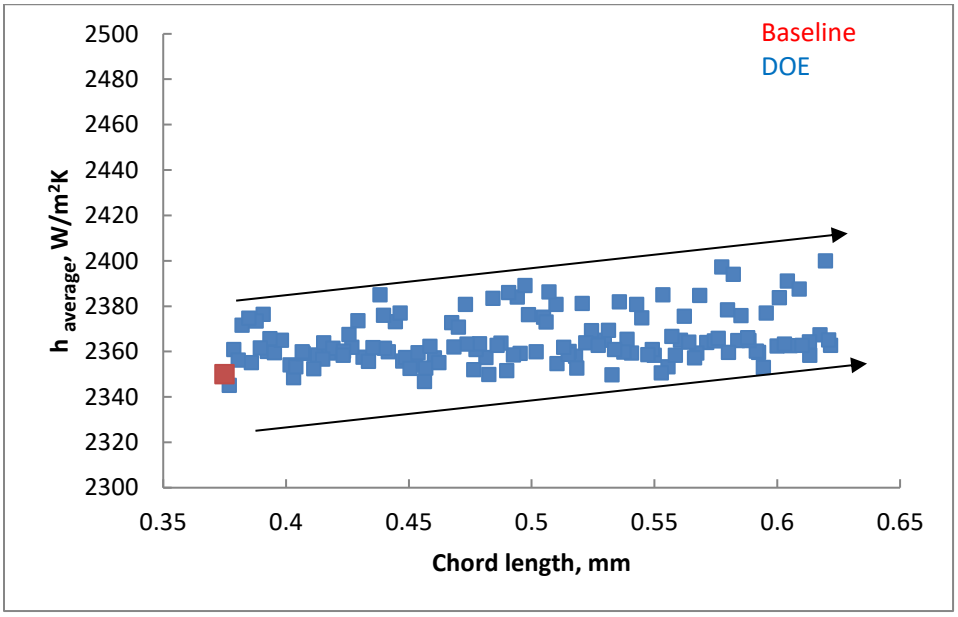

Figure 40 Change of $h_{average}$ with chord length

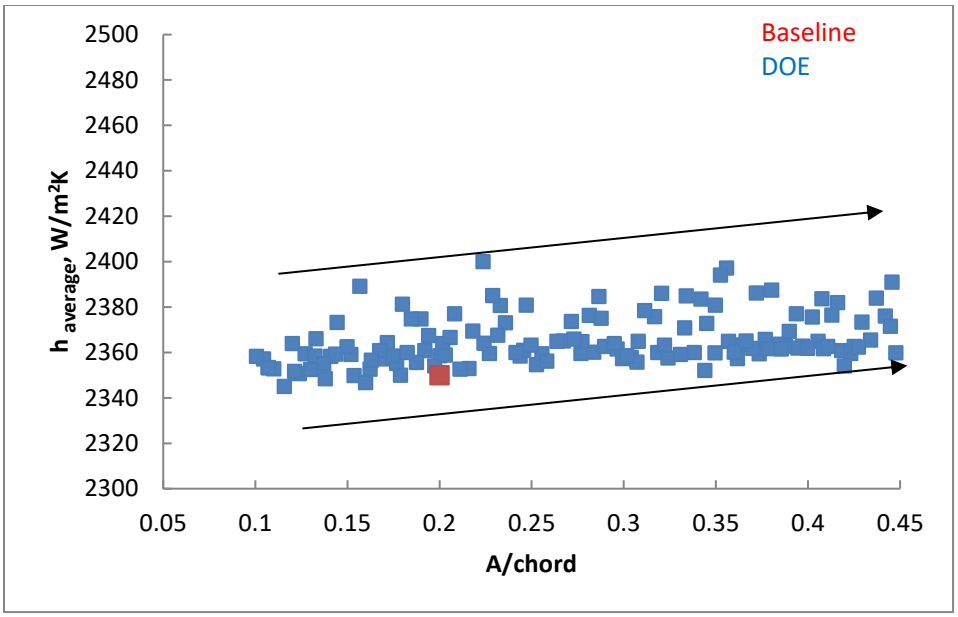

Figure 41 Change of $h_{average}$ with A/chord ratio

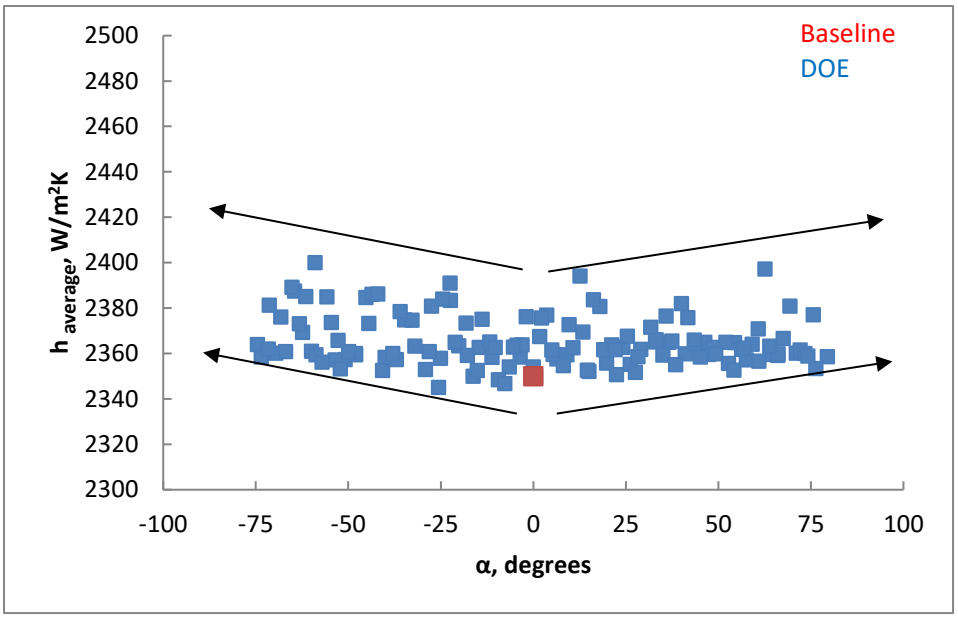

Figure 42 Change of $h_{average}$ with leading edge angle

Based on Figure 43, there is no apparent trend between A/B ratio and average heat transfer coefficient. Solutions that have relatively higher heat transfer coefficients are populated within the envelope of 0.8 to 1.6 in terms of A/B ratio. The range is skewed towards higher A value, which confirms the fact that higher true chord length favors heat transfer.

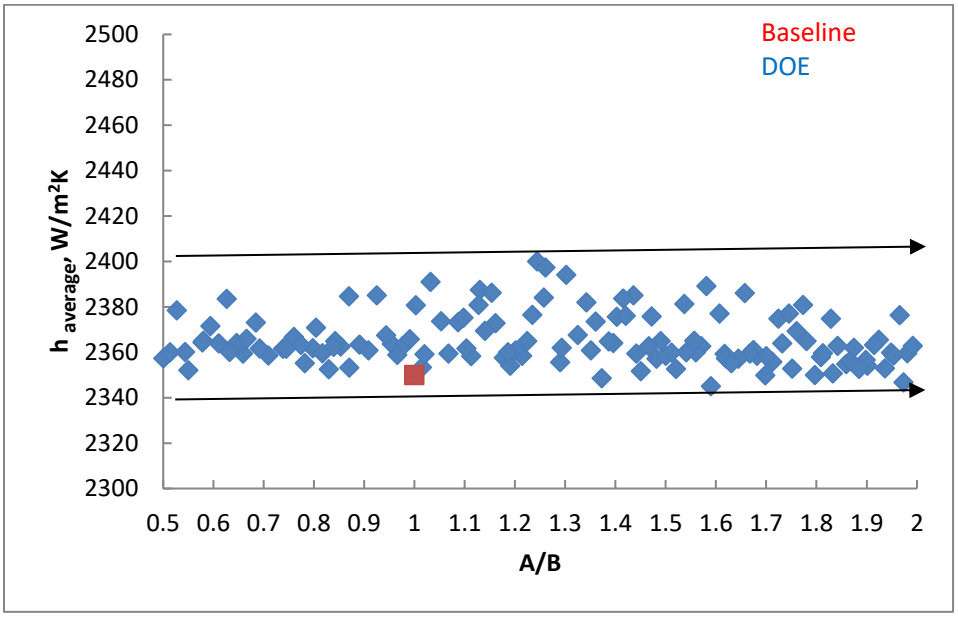

Figure 43 Change of $h_{average}$ with A/B ratio

Figure 44 depicts the relationship between the second slope of the polynomials, k_2, and average heat transfer coefficient. Note that the plot shows the k_2 values for the polynomial residing at the first quadrant of the coordinate system; hence they are positive. The slight positive slope is apparent from the collected data claiming that better solutions are available at higher k_2. This was expected as the steeper slope tends to make the pin fin thicker in the vertical direction creating higher velocity regions. Considering that the pressure drop across the channel was not included in this study and predicting higher hydrodynamic losses at higher slope values played the primary role in keeping the limits of slope range in

a relatively moderate value, such as 15 radians. Figure 45 shows Y_{end} effect on heat transfer. As Y_{end} changes, the trailing edge of the hydrofoil deviates from the y=0 line forcing asymmetric flow in the channel, claiming that higher the deviation from horizontal axis higher the heat transfer performance. This is also due to the fact that all the hydrofoils have the same origin locations. Limited by the width of the channel, 1.5 mm, it is predicted that close the trailing edge gets to the side of walls of the channel pressure drop might substantially increase at constant Re number due to the creation of smaller cross-sectional areas. Therefore, Y_{end} /chord ratio was set such that Y_{end} value does not pass the coordinates of the quarter of the channel width.

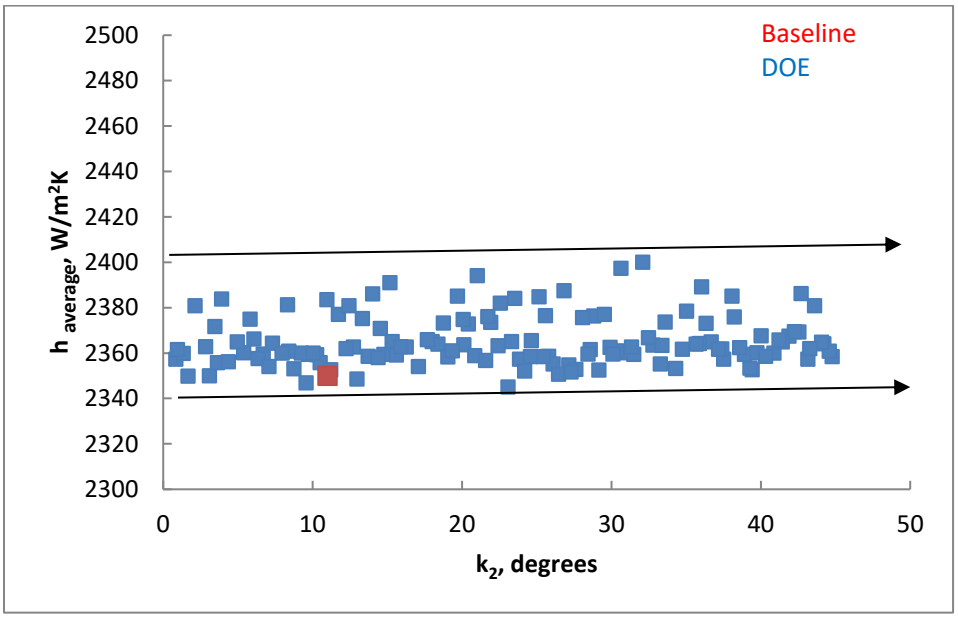

Figure 44 Change of $h_{average}$ with k_2 slope

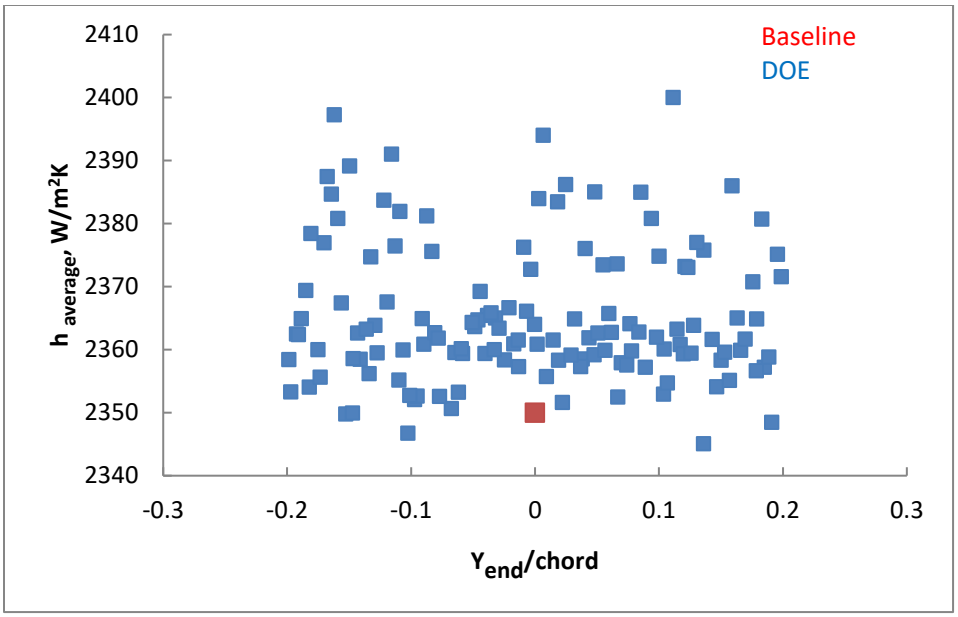

Figure 45 Change of $h_{average}$ with Y_{end}/chord ratio

4.2. Optimization with baseline single hydrofoil

Single hydrofoil has been optimized implementing GA algorithm using below constraints and objectives:

Constraints:

- Origin=0
- 0.375 mm < *Chord* < 0.625 mm
- 0.1 < *A/chord* < 0.45
- 0.5 < *A/B* < 2.0
- $-80^0 < \alpha < 80^0$
- -0.2 < Y_{end}/*chord* < 0.2
- $-45^0 < k_2 < 45^0$

Objectives:

- ✓ Maximize the average heat transfer coefficient on the heater area, Figure 22.
- ✓ Minimize the pressure drop across the channel

Boundary conditions:

- ❖ Fluid medium: HFE 7000
- ❖ $Re_{channel}$=204
- ❖ q''= 66803 W/m^2

Overall, 648 converged members were obtained. Figure 46 depicts the results in terms of pressure drop across the channel and the average heat transfer coefficient. There is one outlier that was not included in the analysis of the data. The representative Pareto front also included to assist in identifying the good performing members. The maximum pressure drop of the populated members was recorded to be around 200 Pa, where the baseline is 135 Pa. Heat transfer coefficient increases up to 2420 W/m^2K, where the baseline is 2350 W/m^2K. However, the data population is denser in the range that is less than 2400 W/m^2K. The same is true for the range of 135 Pa to 165 Pa in terms of pressure drop. Figure 47 shows the data located in the densely populated area of Figure 46.

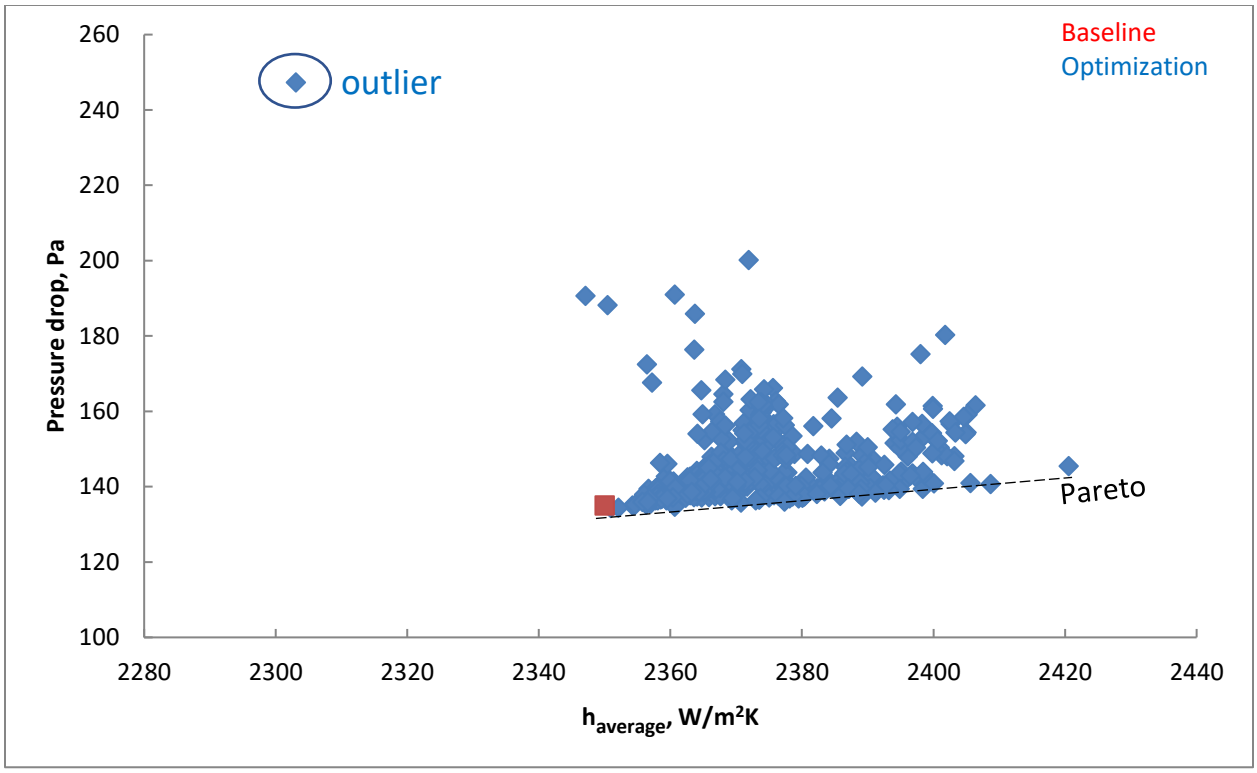

Figure 46 Pareto front of the optimization with a single hydrofoil.

The criteria used in selecting the best member were pressure drop together with the maximum temperature on the heater area. The members that are picked for further inspection are shown in Figure 47 based on the member ID number. The maximum heater temperature difference between each of these members and the baseline is ranging from 0.8 to 1.4^{0}C. It is worth to note that this value was not always positive among the members and which were not considered to be selected for further investigation. Figure 48 has the geometries associated with the data points selected from Figure 47. In general, all selected members have bigger and wider fins compared to the baseline, specifically at higher chord and A values. Member 62 and 420 have similar shapes and more streamlined compared to 266, whereas 266 has the lowest chord out of all three. Even though based on the table in Figure 48, member 62 is the best performing fin, it was not selected as the best member due to the fact it is located in the less dense area

of the optimized population and has the largest geometry. Member 420 is thinner version of 62 and has almost the same thermal and hydraulic performance as member 266. Considering the Re number used as boundary condition is relatively lower, the geometry having the smallest chord length, member 266, was selected for further investigation, predicting that it will result in lower pressure drop at higher Re numbers compared to other members. Additionally, compared to member 420, member 266 is not that streamlined and may induce additional unsteadiness in higher mass flow rates enhancing heat transfer.

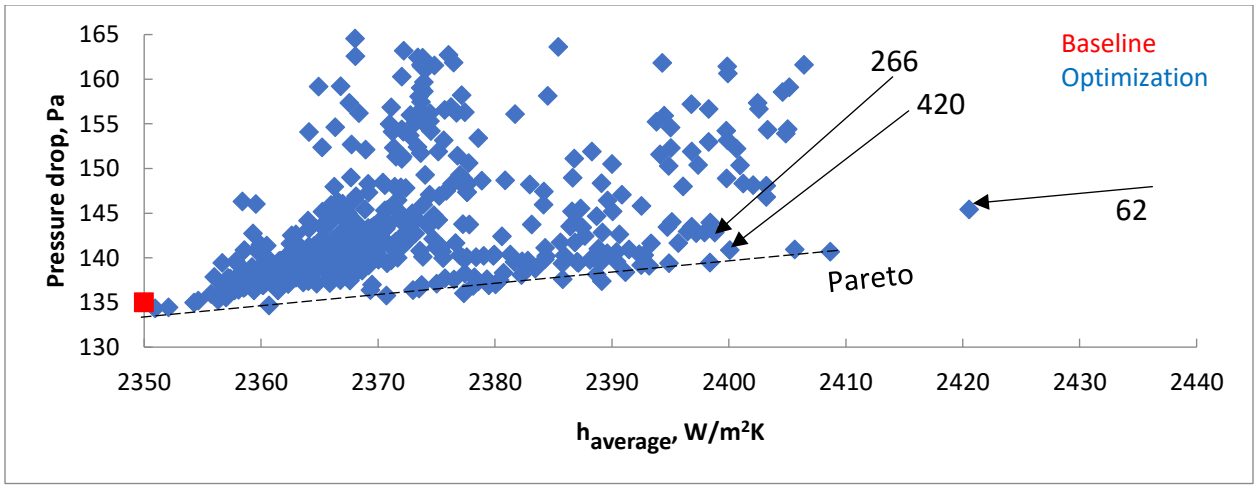

Figure 47 Detailed description of denser data population.

	$h_{average}$, W/m_2K	T_{max}, ^{0}C	Pressure drop, Pa
baseline	2350	58.4	135
62	2420	57	145
266	2400	57.7	143
420	2402	57.6	140

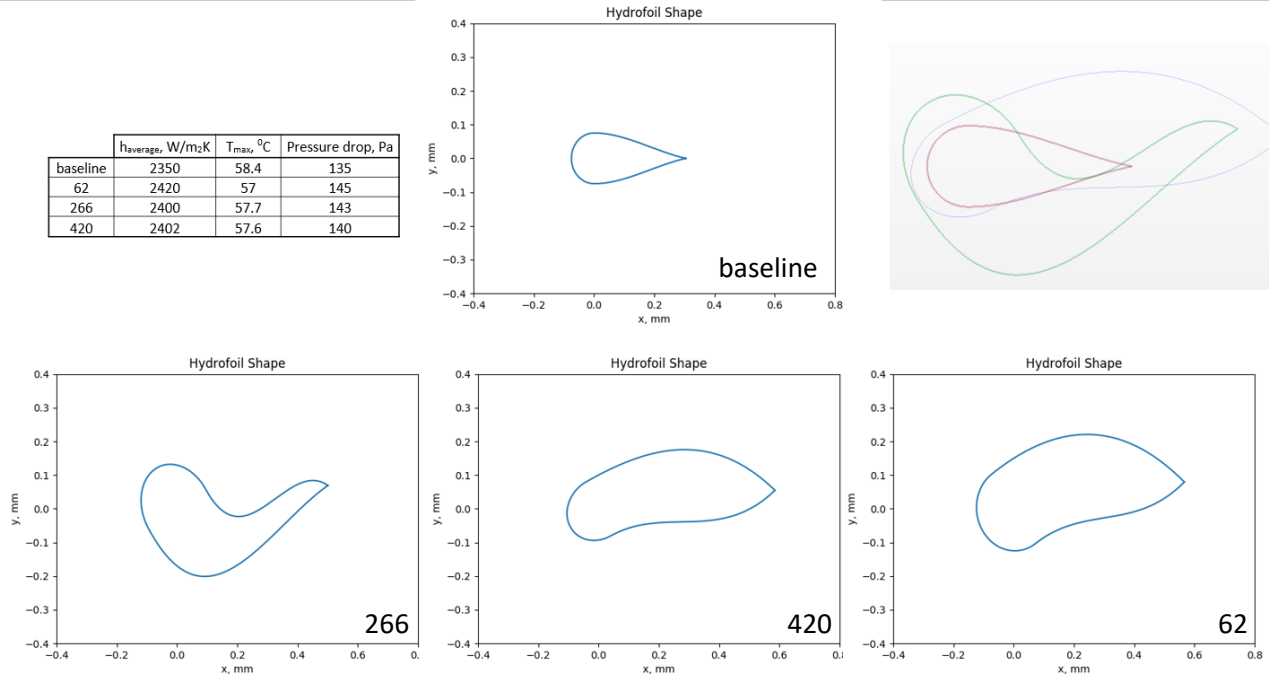

Figure 48 Best performing geometries compared to baseline

Member 266 will be called bird design from now on in the text. Additional conjugate heat transfer has been performed under three different Re numbers while keeping the heat flux constant among the cases. The performance advantage of the bird design increased as the Re number increases as seen in Figure 49. One reason is that the frontal area of the bird design is larger than the baseline hydrofoil encouraging the horseshoe vortex to cover larger area resulting in improved local heat transfer coefficient. Also, local unsteadiness is visible at the downstream of the bird design. The turbulent kinetic energy profile also shows stronger profiles at all Re numbers for the bird design, Figure 51.

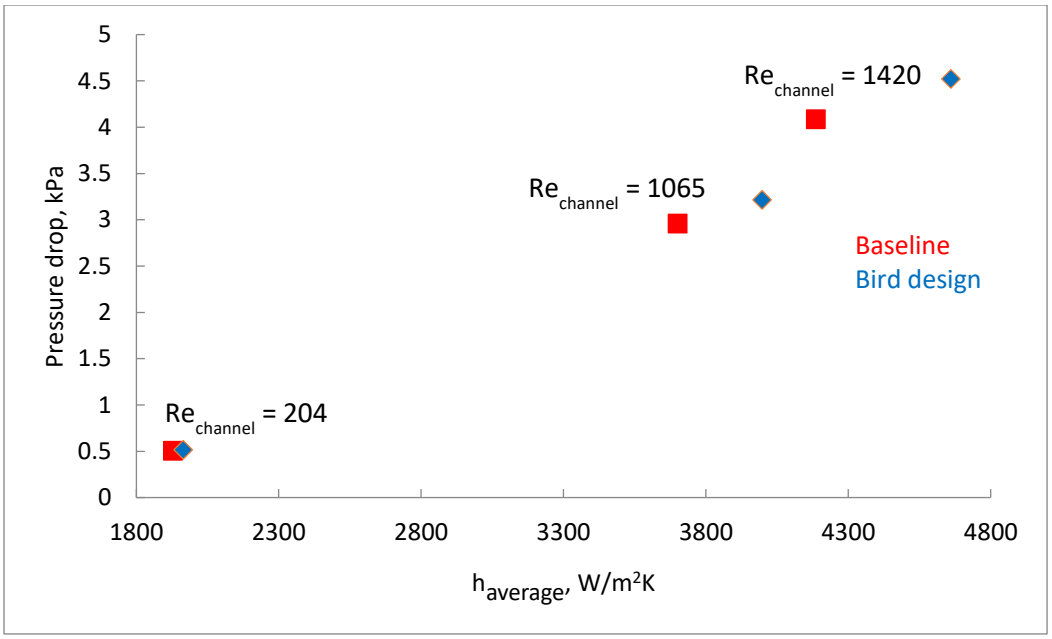

Figure 49 Average heat transfer coefficient from CHT simulations.

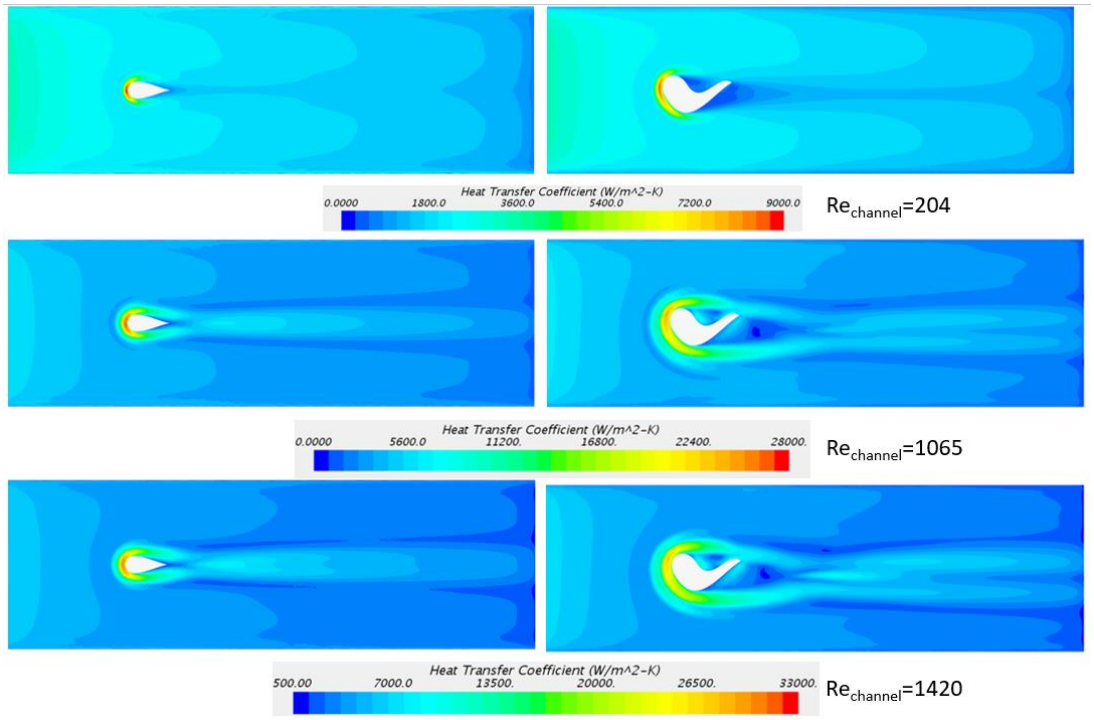

Figure 50 Local heat transfer coefficient on the heater surface at different Re numbers.

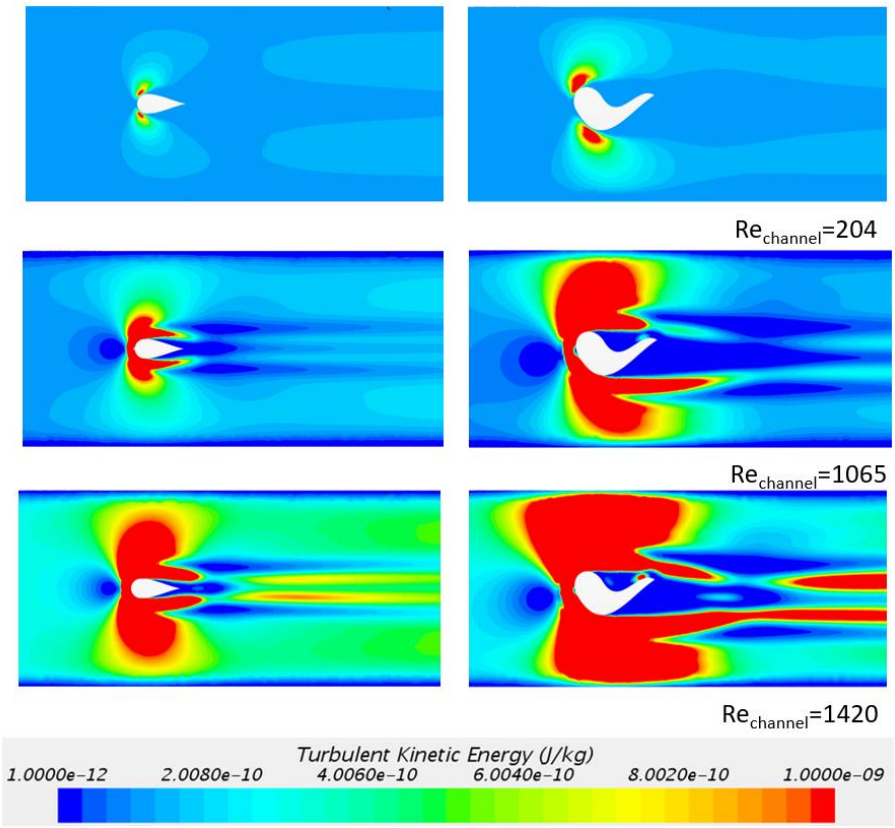

Figure 51 Turbulent kinetic energy at the plane next to the heater

4.3. Optimization with baseline hydrofoil and a satellite

This section is discussing the effect of additional satellite in the channel with single hydrofoil the same as baseline. The parameterization method has been discussed in detail in section 3.1. The optimization is expected to locate satellite such that the hydrodynamic and thermal performance is enhanced. The boundary conditions and objectives used are identical to the ones in section 4.2. Additional satellite hydrofoil was also parametrized in the same manner as the main hydrofoil in the channel, see section 3.1. Note that the main hydrofoil is not optimized in this cycle, leaving only satellite geometry constraints. The ranges of the satellite hydrofoil geometry parameters were selected so that it would not be larger than the main hydrofoil. Satellites origin is also parametrized here to ensure that optimization

sweeps the location around the main hydrofoil based on the given offset dimension. The details of the setup are as below:

Constraints:

- 0.1mm <*Offset_sat*< 0.4 mm
- *Origin_sat* is based on the offset input
- 0.1875 mm < *Chord_sat*< 0.375 mm
- 0.1 < *A_sat/chord_sat* < 0.45
- 0.5 < *A/B* < 2.0
- $-45^0 < \alpha < 45^0$
- $-15^0 < \gamma < 15^0$
- Y_{end_sat} is computed within the parametrization using above parameters such that it will always lie on the satellite center orbit, see section 3.1.
- $0 < k_2 < 45^0$
- 1 <*sat_center*< 199, defining the location of the satellite center based on matrix including *x* and *y* coordinates of the satellite orbit.

Objectives:

- ✓ Maximize the average heat transfer coefficient on the heater area, Figure 22.
- ✓ Minimize the pressure drop across the channel

Boundary conditions:

- Fluid medium: HFE 7000
- $Re_{channel}$=204
- q''= 66803 W/m^2

544 converged members were recorded and plotted in Figure 52, showing the space covered by the optimization. Unlike the previous optimization, the members to the left of the baseline are quite a few. These members were excluded from best member selection due to poor thermal and hydraulic performance.

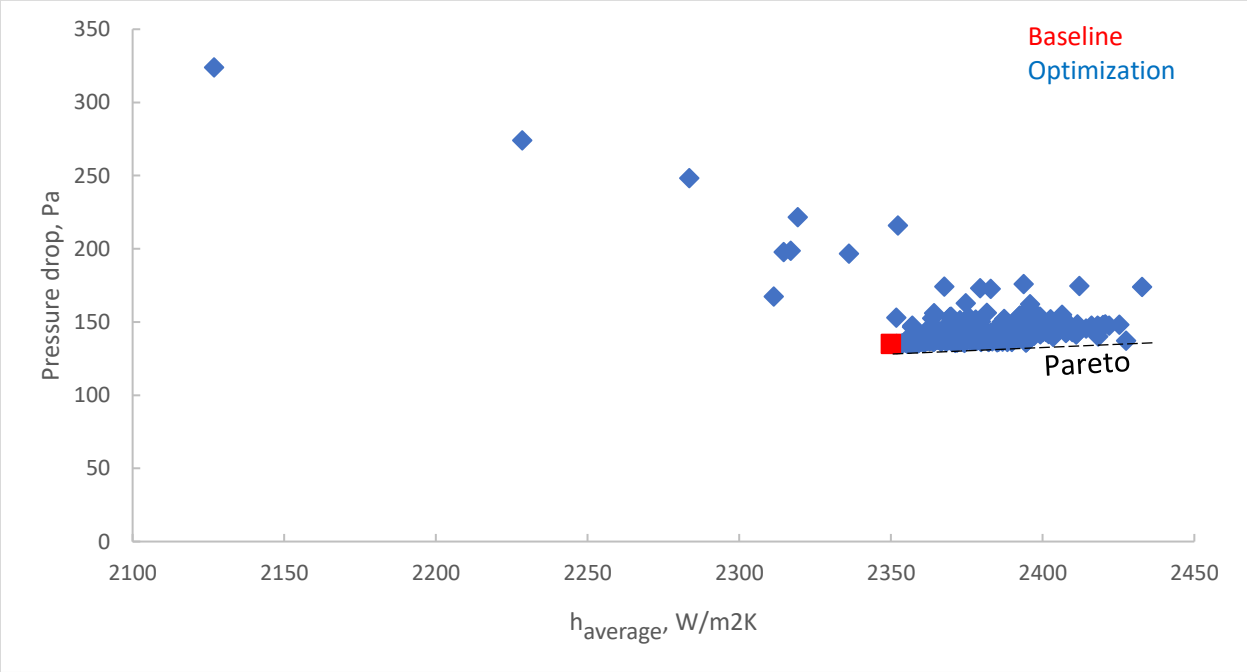

Figure 52 Optimization space for the single hydrofoil with a satellite.

Figure 53 shows all the member in the optimization space that has at least improved thermal performance. Member 340 has the best thermal performance with an acceptable pressure drop. It is

located further away from the area having a denser data population, however when the neighboring members are analyzed, the evolution of the geometries is apparent claiming that is should not be an outlier. Member 32 has a thin satellite located around the leading edge of the hydrofoil, re-directing the flow towards the sidewalls of the channel which is why pressure drop high. The consecutive member located next 32, member 411, has a thicker satellite located very close to the trailing edge of the hydrofoil. This satellite creates a smaller cross-sectional area between the hydrofoil and itself, increasing the high speed region. Also, the separation region on the main hydrofoil side, where the satellite is located, is suppressed due to the above mentioned high-speed flow region that is confined between two hydrofoils. The advantage of this kind of behavior in terms of thermal and hydraulic performance is recognized by the optimization which leads to member 340. The main difference between member 411 and 340 is the dimension of the satellite. Same type boundary layer separation suppression could be performed using more streamlined and thinner satellite geometry. Also, the length of the satellite is slightly increased from member 411 to 340, extending region of the confined channel with high velocity. Member 135 is the derivation of 32 and not that successful trial as the pressure drop increased substantially via directing the flow towards sidewalls and creating longer blockage perpendicular to the flow direction. Overall it could be stated that satellites located closer to the leading edge of the hydrofoil do not provide good hydraulic performance and are expected to increase pumping power at higher Re numbers substantially. On the other hand, satellites that is located downstream of the mid chord of the hydrofoil may have hydrodynamically favorable characteristics. Therefore, member 340 was selected for further conjugate studies. The summary of the results of conjugate studies is presented in section 4.5.

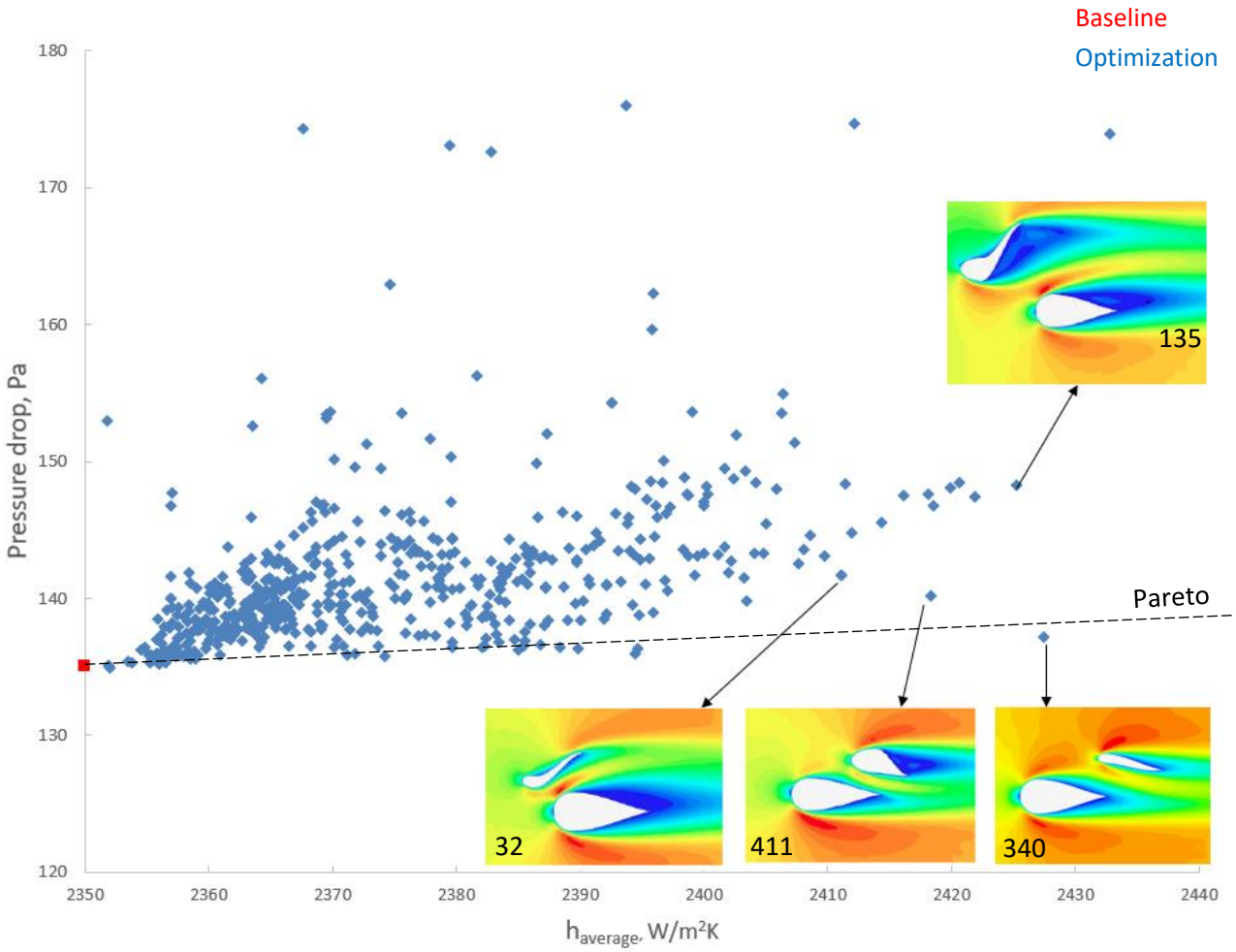

Figure 53 Improved members.

4.4. Optimization with bird-design hydrofoil and a satellite

The same approach discussed in section 4.3 was applied to the bird design. The main hydrofoil is the best member selected in section 4.2 with identical geometrical parameters, which will be held constant during the optimization. Satellite parametrization and boundary conditions are also identical to the one described in section 4.3. The overall statement of the optimization problem is described below again:

Constraints:

- 0.1mm <*Offset_sat*< 0.4 mm
- *Origin_sat* is based on the offset input
- 0.1875 mm < *Chord_sat*< 0.375 mm
- 0.1 < *A_sat/chord_sat* < 0.45
- 0.5 < *A/B* < 2.0
- $-45^0 < \alpha < 45^0$
- $-15^0 < \gamma < 15^0$
- Y_{end_sat} is computed within the parametrization using above parameters such that it will always lie on the satellite center orbit, see section 3.1.
- $0 < k_2 < 45^0$
- 1 <*sat_center*< 199, defining the location of the satellite center based on matrix including *x* and *y* coordinates of the satellite orbit.

Objectives:

- ✓ Maximize the average heat transfer coefficient on the heater area, Figure 22.
- ✓ Minimize the pressure drop across the channel

Boundary conditions:

- ❖ Fluid medium: HFE 7000

- $Re_{channel}$=204
- q''= 66803 W/m^2

Figure 54 shows the optimization space obtained from 572 converged members. The bird design baseline, obtained in section 4.2., is included in the plot in green color. It could be observed from the plot that the bird design baseline is also residing very close to the Pareto front claiming its thermal and hydraulic performance is better than almost half of the members. There were also few members to the left of the baseline in the optimization space for single hydrofoil; however, the count of those members is substantially high here. One of the main reasons behind it is the fact that bird design has larger geometrical dimensions compared to the single hydrofoil design. Larger the fin geometry lesser the locations for satellites on the satellite orbit that would lead to higher thermal and hydraulic performance. Figure 55 depicts all the improved members compared to a single hydrofoil baseline and bird design baseline. Five members have been selected randomly in the better performing region to understand the evolution of the satellite geometries. It is obvious from members 118, 251, 365, and 226 that for higher thermal performance, the satellite needs to be located around the leading edge of the main pin fin. The common characteristics between the latter four members is the direction of the incoming cross flow towards the side wall of the channel while creating a high speed flow region between the main fin and satellite. The same type of behavior was also seen in the previous optimization cycle, Figure 53. The satellite shown in member 21, however, forces slightly different flow behavior. It suppresses the separation on one side of the main fin and does so via creating high-speed flow region between itself and the main fin. The length of this high-speed flow region is elongated over the chord length of the main fin, making it a good candidate for local heat transfer also. Considering all five members shown have

comparable hydrodynamic performances and predicted advantages of member 21, it was selected for further conjugate heat transfer analysis.

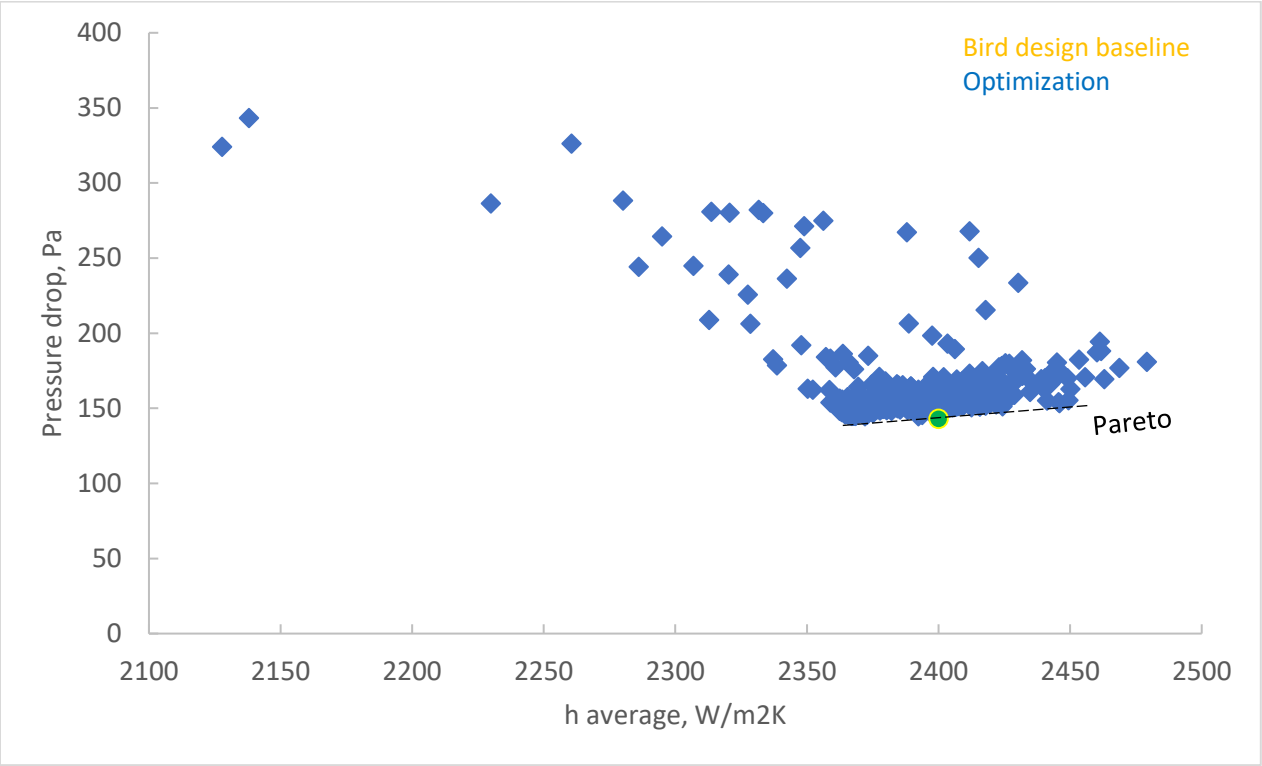

Figure 54 Optimization space for the bird design with satellite.

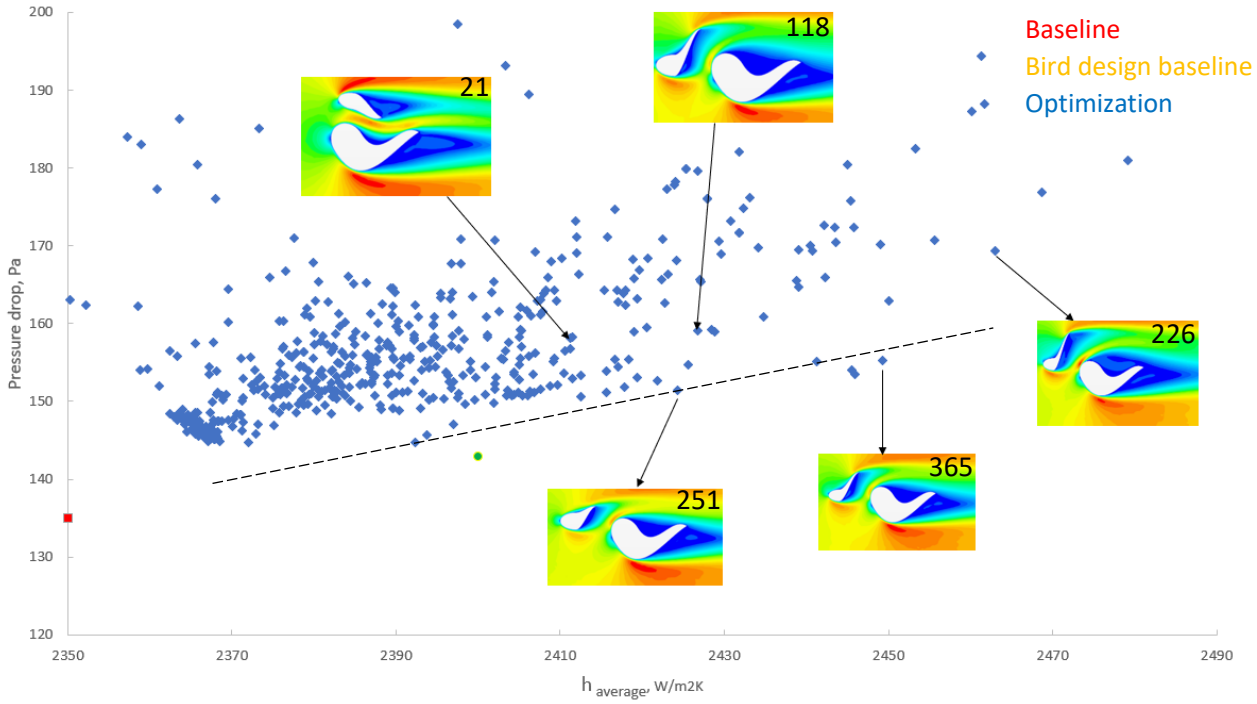

Figure 55 Improved members

4.5. Overall comparison of the average thermal performance

This section discusses the results of the conjugate heat transfer model implementing the best geometries selected through section 4.2 to 4.3. The main aim is to determine if the convective thermal performance of the channels would still be sustained together with conduction through the neighboring solids. The conjugate setup identical to experiments, discussed in section 2.2., has been used during the simulation. Three different Re numbers, based on the channel hydraulic diameter, have been analyzed. The heat flux was kept constant at q''=66803 W/m^2 as in optimization cycles.

Figure 56, Figure 57, Figure 58 includes the contours for local heat transfer coefficient, local temperature, and local turbulent kinetic energies for three different Re numbers. For a lower Re of 204, Figure 56, the main difference creator is the horseshoe vortex around the leading edge of the fins. The

local heat transfer coefficient plot apparently shows this mainly for the cases of single baseline hydrofoil and baseline hydrofoil with a satellite. However, for the case with bird design and a satellite local heat transfer coefficient, improvement is happening along the chord of the main fin. Also, the latter case is the best performing case out all four cases, which could be confirmed on local temperature and turbulent kinetic energy plots. Comparing the high-temperature region towards the trailing edge of the heater among four cases, it could be claimed that the addition of satellite to the baseline hydrofoil has a minor effect, whereas bird design decreases this region substantially. The addition of a satellite to the bird design resulted in further cooling effect as seen in the plot. Turbulent kinetic energy distributions were significantly improved in the designs, including bird design, whereas for two cases including baseline hydrofoil only local values are enhanced with an addition of the satellite. Figure 57 and Figure 58 how the geometries perform in higher Re numbers of 1065 and 1420, respectively. For the designs, without a satellite the only difference is the horseshoe vortex size which is enhanced compared to Figure 56. However, the additional flow passages between the satellite and the main fin are more apparent at high Re number and potential disturbance of the flow even after the fins are more visible. This shows itself in the lower temperature gradients closer to the trailing edge of the heater also, for both high Re numbers. The turbulent kinetic energy plots confirm the heat transfer potential of the bird design with a satellite in high Re numbers, due to higher area covered with strong flow mixing. At Re number of 1065 bird design with a satellite has approximately 4.6 times higher average turbulent kinetic energy compared to baseline hydrofoil whereas for a single bird design, this number is 3.3. The magnitude of the mixing increase in the baseline hydrofoil cases is almost negligible.

Figure 59 shows the area where average and maximum data are shown in Figure 60, Figure 61, Figure 62, and Figure 63 were taken. The area encompasses the immediate neighborhood of the fin which

is why data provided emphasizes the improvements due to geometry changes only. Note that 98.1% of the area where the average is taken is constant as the relative coverage by the hydrofoil fins is 1.9% for bird design with a satellite. Figure 60 shows the average temperature changes in terms of geometry and Re number. The bird design cases have an average temperature below 35^0C whereas cases including baseline hydrofoil is above this value, for Re of 1065. This behavior is repeated for the other Re numbers also. Maximum temperatures are higher for the fins without a satellite compared to fins with satellites where the lowest value is observed at bird design with a satellite case, see Figure 61. The same design has the highest average and maximum heat transfer coefficient as shown in Figure 62 and Figure 63. For instance, there is a 28.1 % increase in the average heat transfer coefficient in the channel containing bird design with a satellite compared to baseline hydrofoil, whereas the pressure drop increase is only 15%. The average thermal and hydraulic performance increase is 16% and 7% in the bird design without a satellite compared to baseline hydrofoil, for Re of 1065. There is only 5% average heat transfer coefficient gain due to the addition of a satellite to the baseline hydrofoil where the pressure drop increase is only 0.6%. The trade-off between performance parameters benefits the increase in the average heat transfer coefficient among all the cases implementing the bird design and addition of satellites.

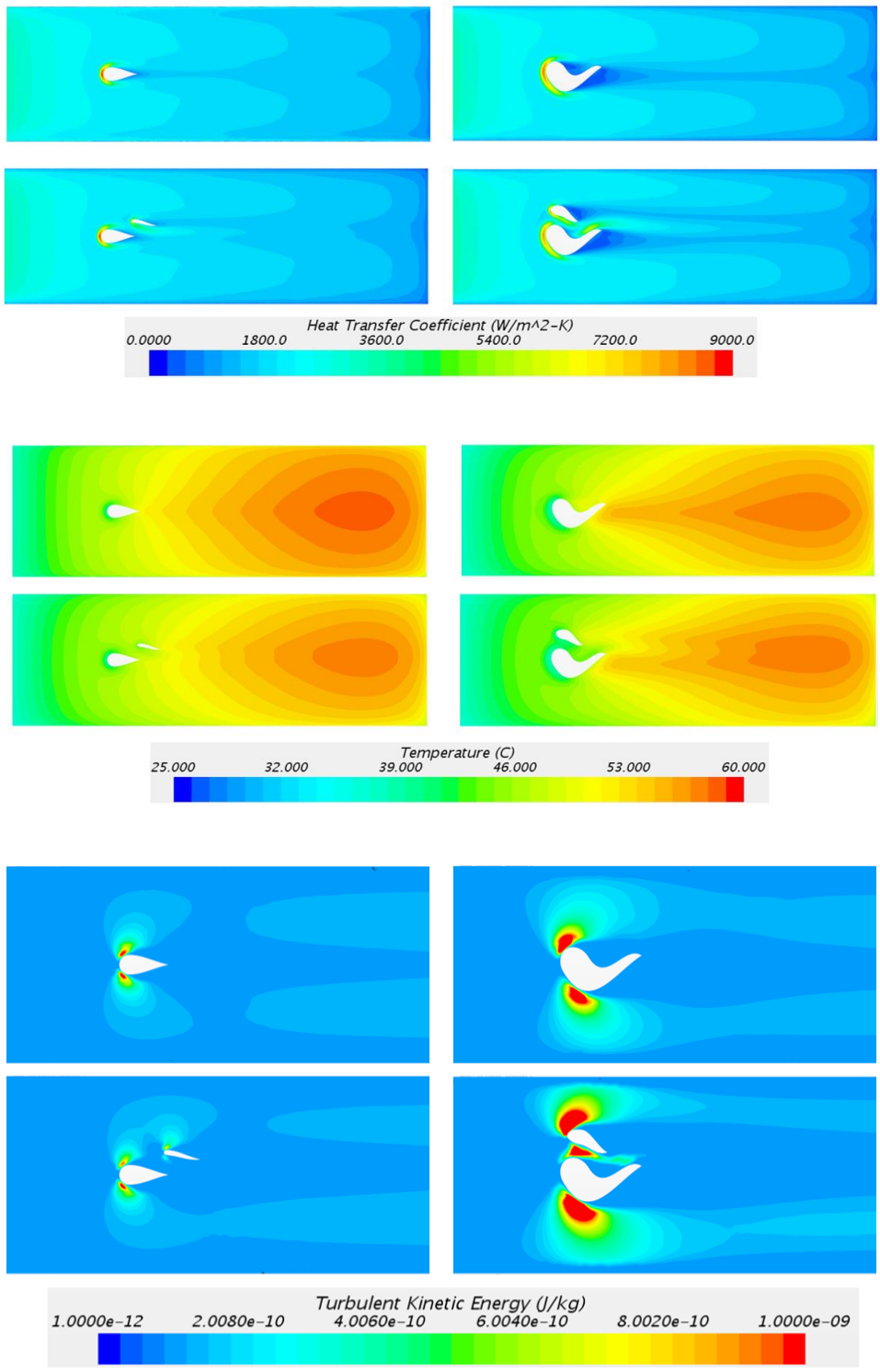

Figure 56 Local heat transfer coefficient, temperature and TKE contours for $Re_{channel}$=204

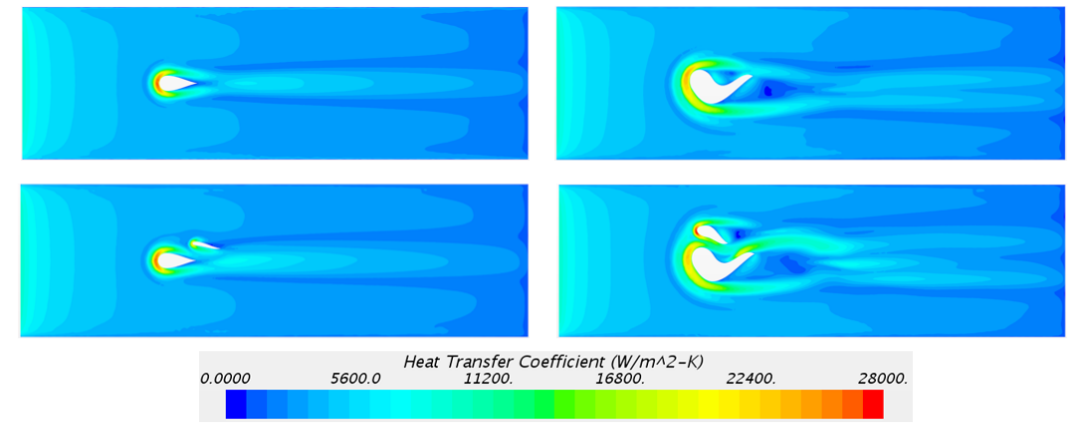

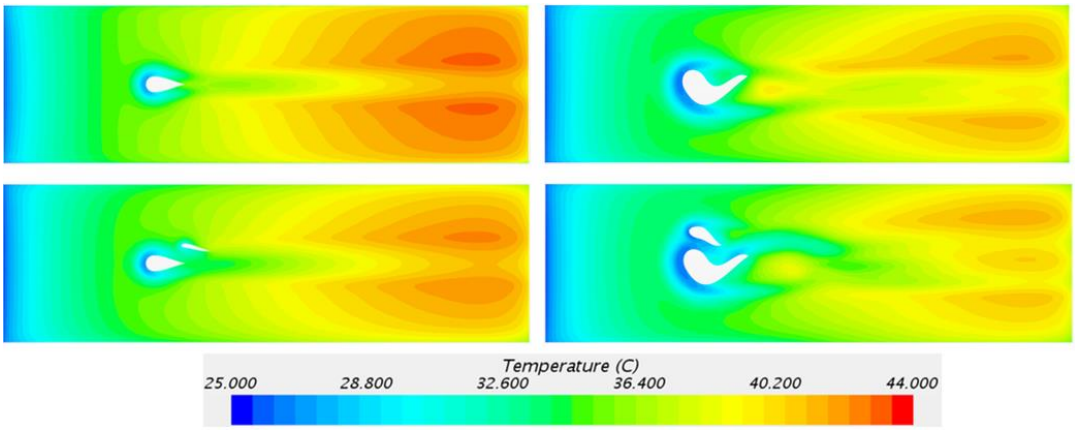

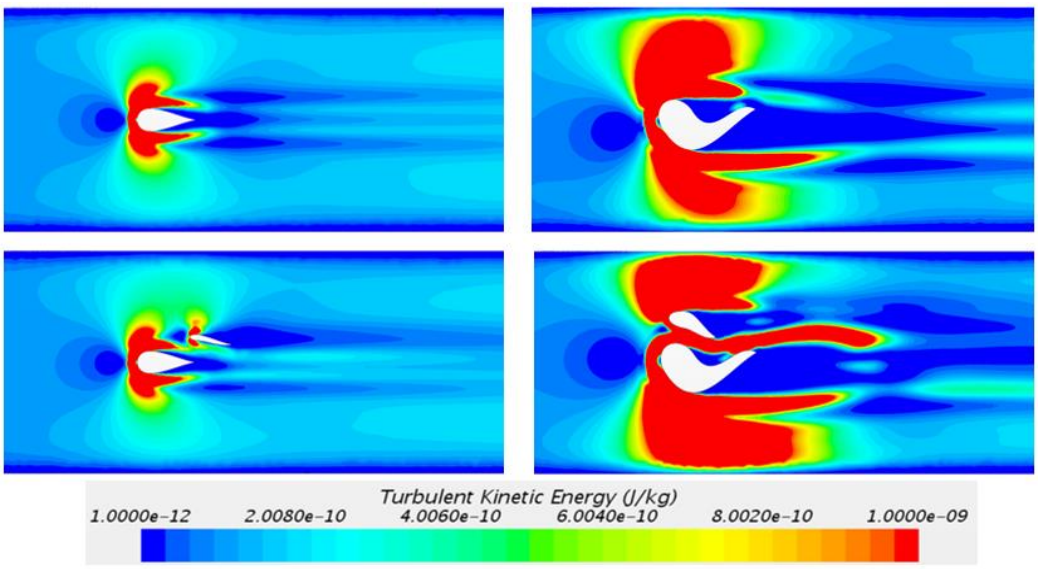

Figure 57 Local heat transfer coefficient, temperature and TKE contours for $Re_{channel}$=1065

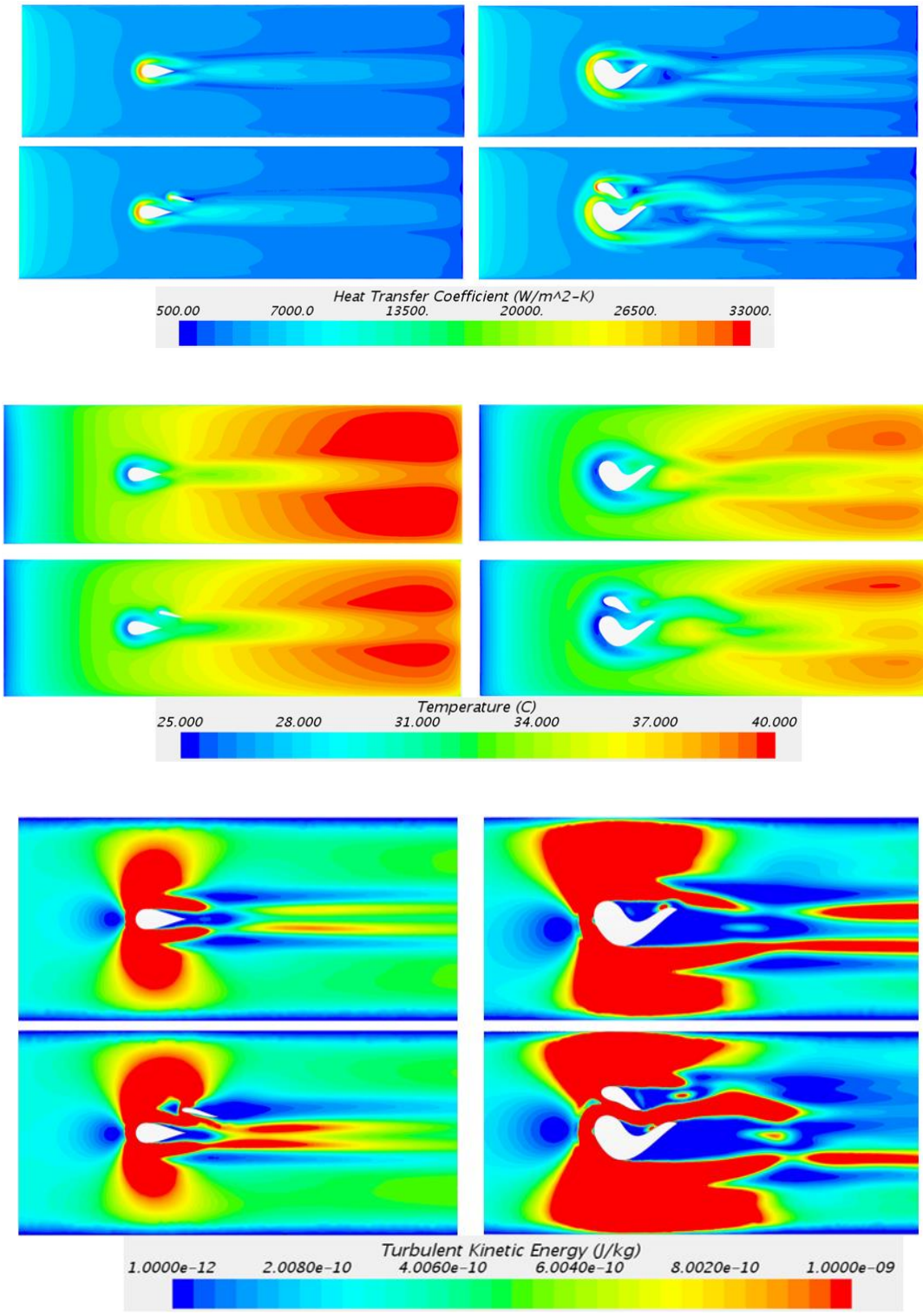

Figure 58 Local heat transfer coefficient, temperature and TKE contours for $Re_{channel}$=1420

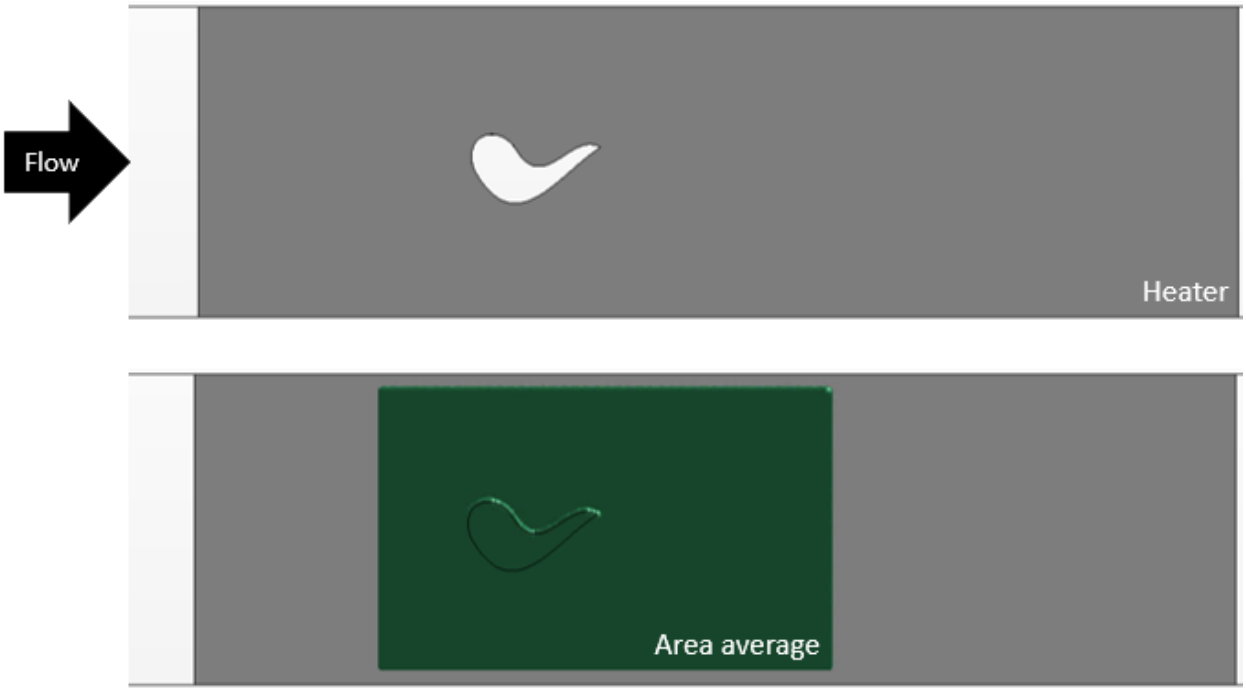

Figure 59 Area used for the data extraction.

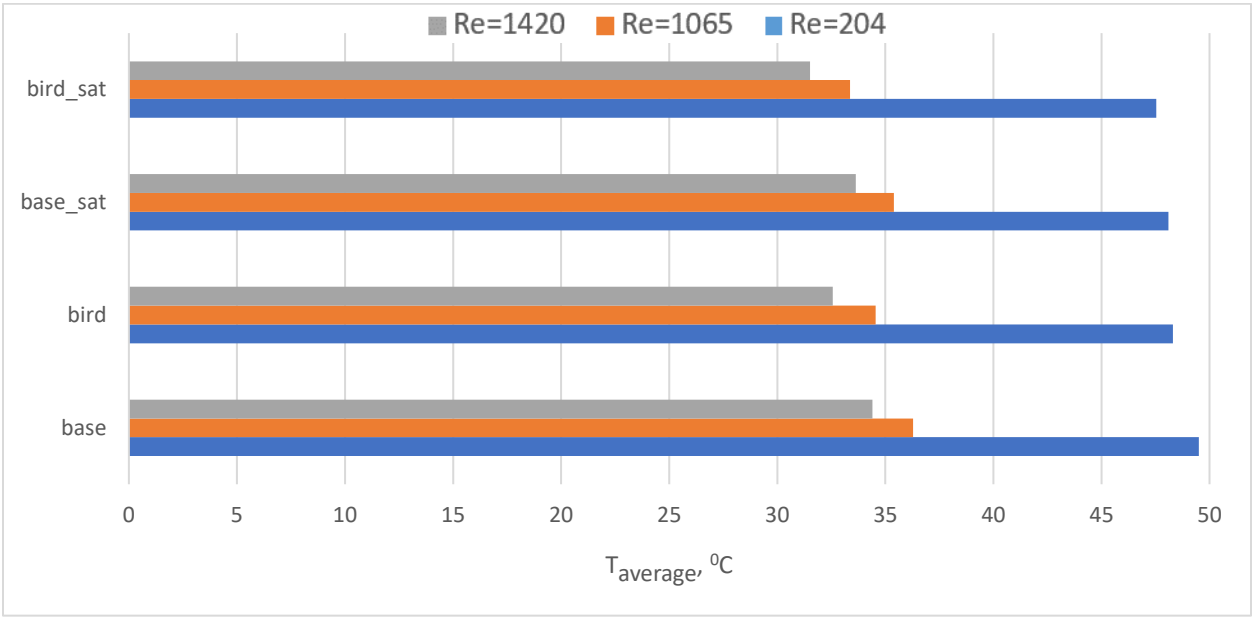

Figure 60 Variation of average temperature based on $Re_{channel}$

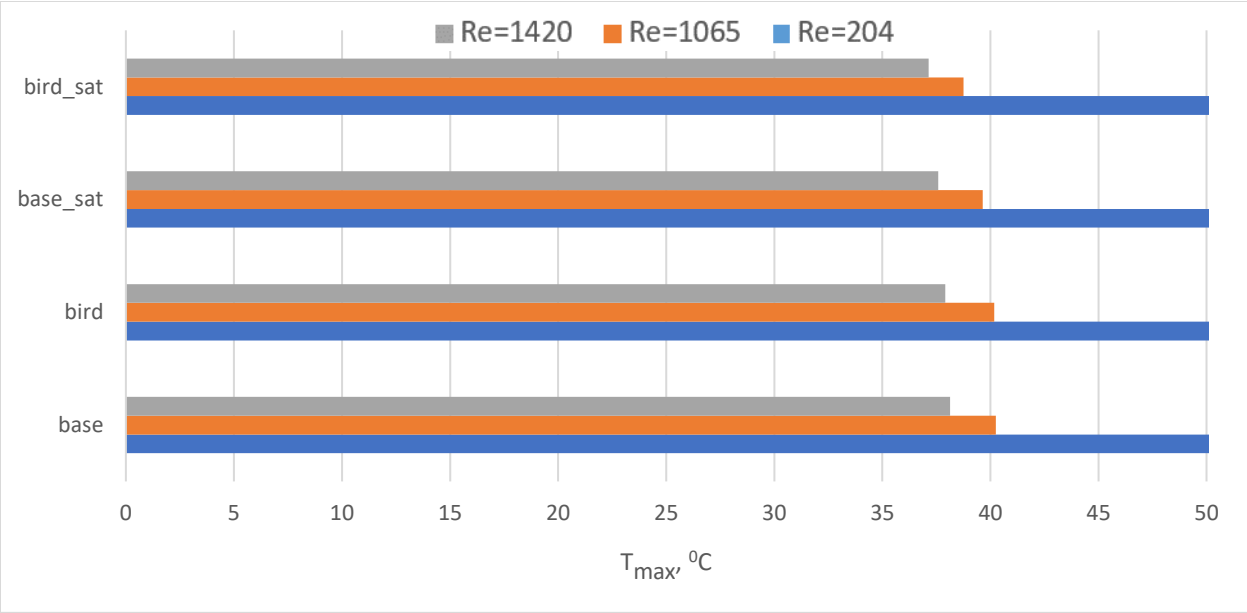

Figure 61 Variation of maximum temperature based on $Re_{channel}$

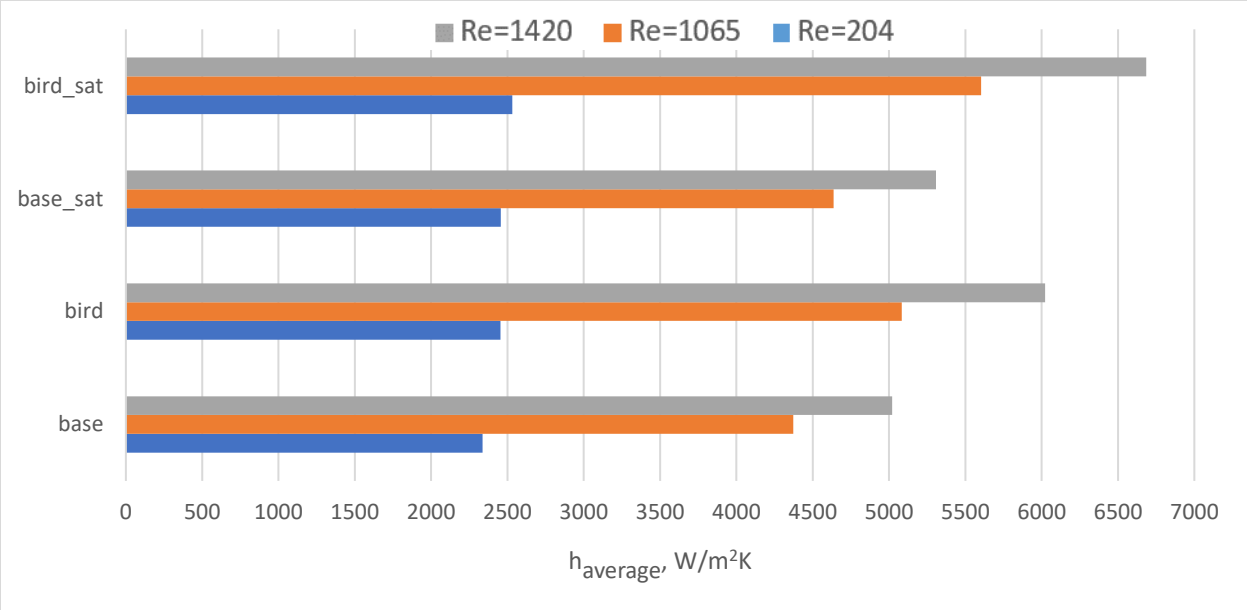

Figure 62 Variation of average heat transfer coefficient based on $Re_{channel}$

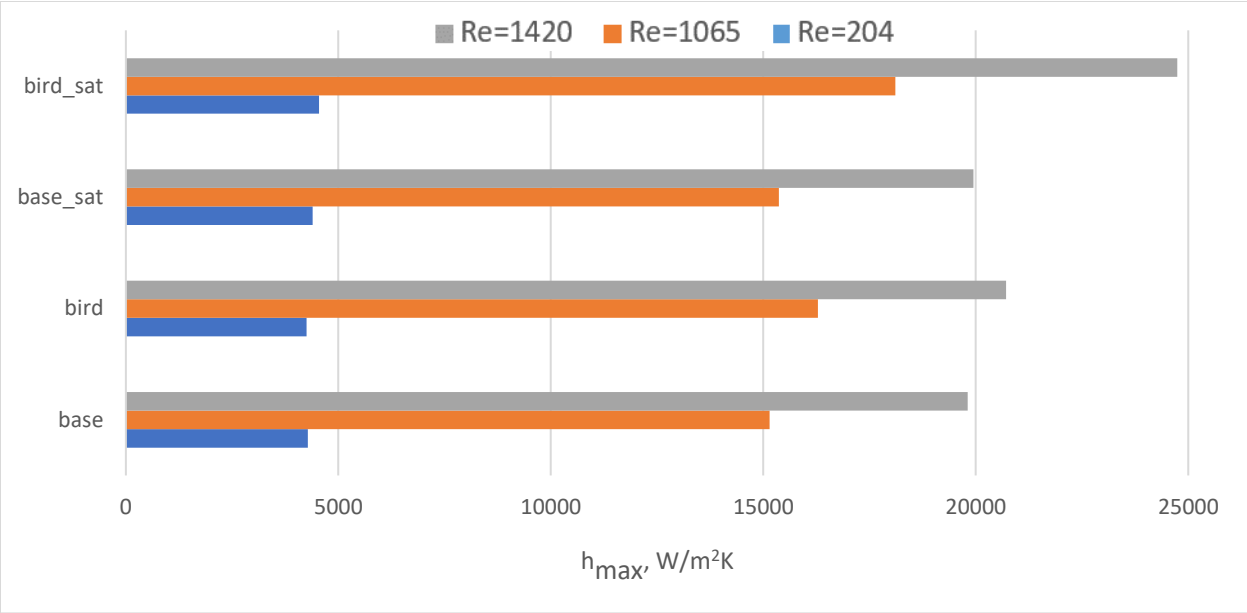

Figure 63 Variation of maximum heat transfer coefficient based on $Re_{channel}$

4.6. Local heat transfer optimization

Experiments, discussed in section 2.2., were evolving around the local temperature measurements behind the hydrofoil. Considering that the studies on optimizing pin fins to maximize local heat transfer in micro heat sinks are scarce, further optimization studies are conducted and presented below. To be compatible with experiments RTD locations used in the experimental setup were considered, as seen in Figure 64. The design selected to perform the optimization is identical to the bird design and satellite configuration selected in section 4.4. Therefore, the RTD2 location used in experiments is no longer valid as the main fin covers that area. Hence, RTD3 and RTD6 locations were selected for optimization purposes, as RTD3 is aligned with the center of the channel where RTD6 is located away from it. The geometrical positions of RTDs relative to channel are also identical to experiments, see section 2.2.

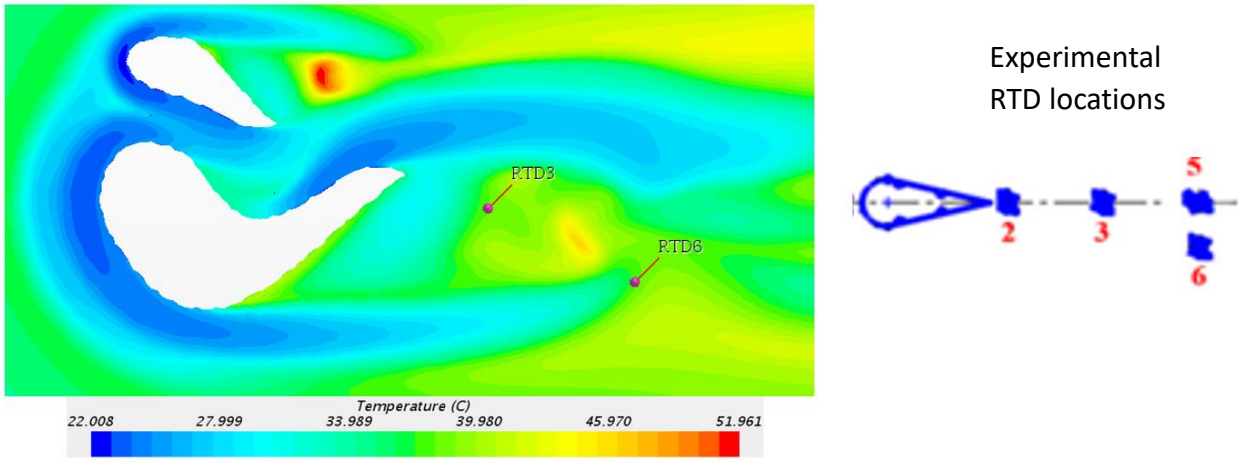

Figure 64 Location of RTDs used in optimization. Temperature plots for $Re_{channel}$=1065.

Two sets of optimizations were performed, for $Re_{channel}$ =204 and 1065. The detailed boundary conditions, constraints and objectives are presented below:

Constraints:

- 0.1mm <*Offset_sat*< 0.4 mm
- *Origin_sat* is based on the offset input
- 0.1875 mm < *Chord_sat*< 0.375 mm
- 0.1 < *A_sat/chord_sat* < 0.45
- 0.5 < *A/B* < 2.0
- $-45^0 < \alpha < 45^0$
- $-15^0 < \gamma < 15^0$
- Y_{end_sat} is computed within the parametrization using above parameters such that it will always lie on the satellite center orbit, see section 3.1.

- $0 < k_2 < 45^0$
- $1 < sat\_center < 199$, defining the location of the satellite center based on matrix including *x* and *y* coordinates of the satellite orbit.

Objectives:

- ✓ Maximize the local heat transfer coefficient on RTD3
- ✓ Maximize the local heat transfer coefficient on RTD6
- ✓ Minimize the pressure drop across the channel

Boundary conditions:

- ❖ Fluid medium: HFE 7000
- ❖ $Re_{channel}$=204 Case 1
- ❖ $Re_{channel}$=1065 Case 2
- ❖ q''= 66803 W/m^2

Figure 65 shows the optimization space for low Re number case. 461 converged members are used to populate the data shown. Pareto front approximately shows a better trade-off solution in terms of RTD temperature. Each data point is colored based on the pressure drop characteristics. Following Figure 66 shows improved members in terms of RTD temperature. Appropriate designs are selected from this plot based on the pressure drop values. When the specific design characteristics such as pumping power, heat dissipation, and maximum operating local temperature, of a system or application, is available, the trade-off solutions could be picked from this plot which is making it very advantageous. Notice that the red points are all equal or above the baseline in terms of the pressure drop value. As this is a general study, few designs with improved thermal and hydraulic performance were selected, are

shown with respect to the geometries in Figure 67. It has to be mentioned that the study is using a section of the flow channel without any conjugation with solids; the temperature readings of the RTD are very high compared to section 2.2. Figure 27 also confirms that the magnitude of the conjugate effects are high at this mass flow rate. Overall, most of the improved members seems to have similar geometries, cases 199, 202 and 301 in Figure 67. It is apparent that there are slight differences in the satellite geometry and its relative location to the main fin which is driving various pressure drop values. Nevertheless, the improvement in the local temperatures is more than 30^0C for RTD3, where RTD6 temperature is 3^0C lower than the baseline. In member 189 and 202, the temperatures of RTDs are trading off and are subject to design requirements for selection. Considering the magnitude of conjugate effects at this Re number, implementation of such geometries in actual setups would lead to even lower temperatures as additional paths for heat flow will be introduced together with solids.

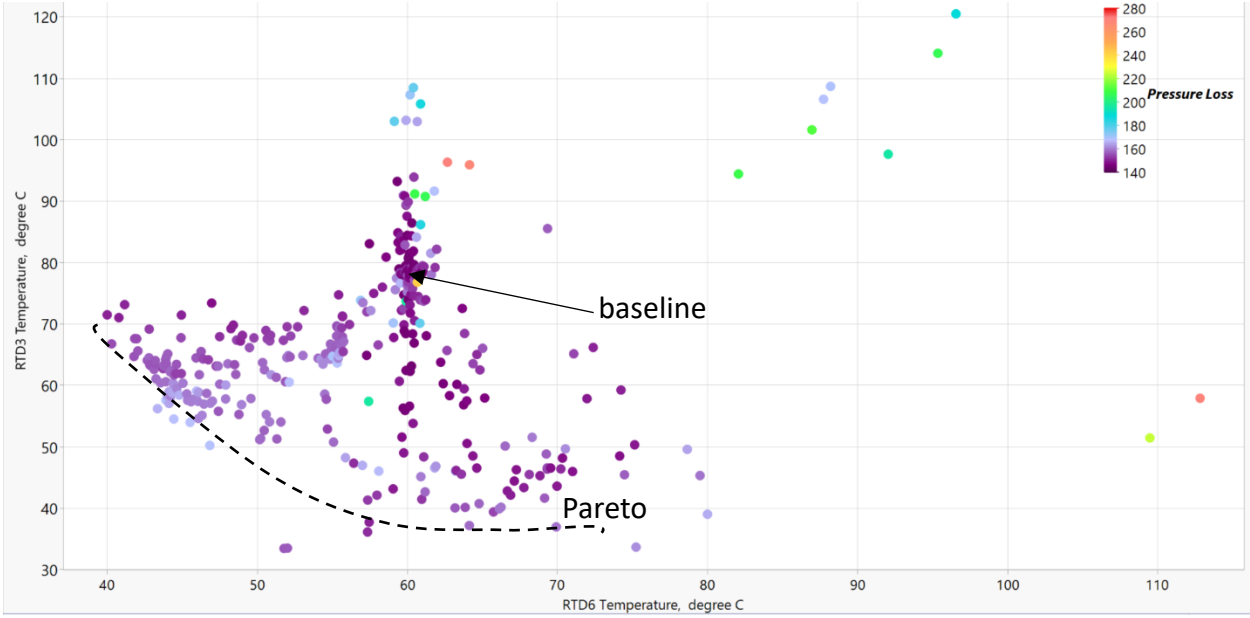

Figure 65 Optimization space, Case 1.

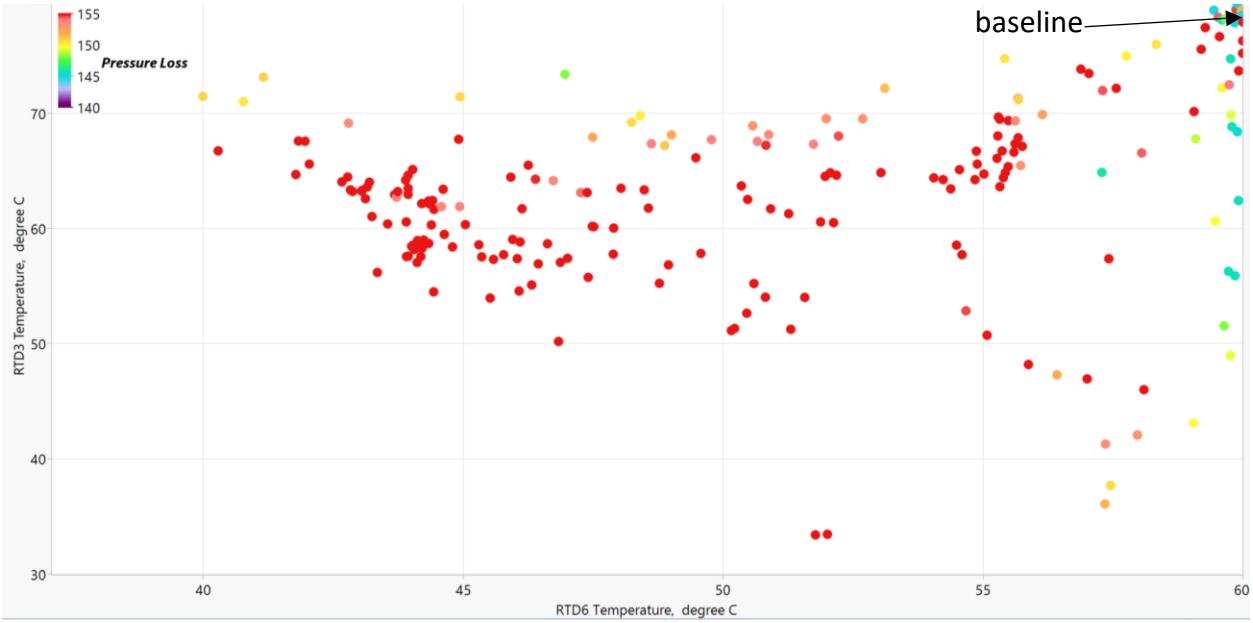

Figure 66 Improved members in terms of RTD temperature, Case 1.

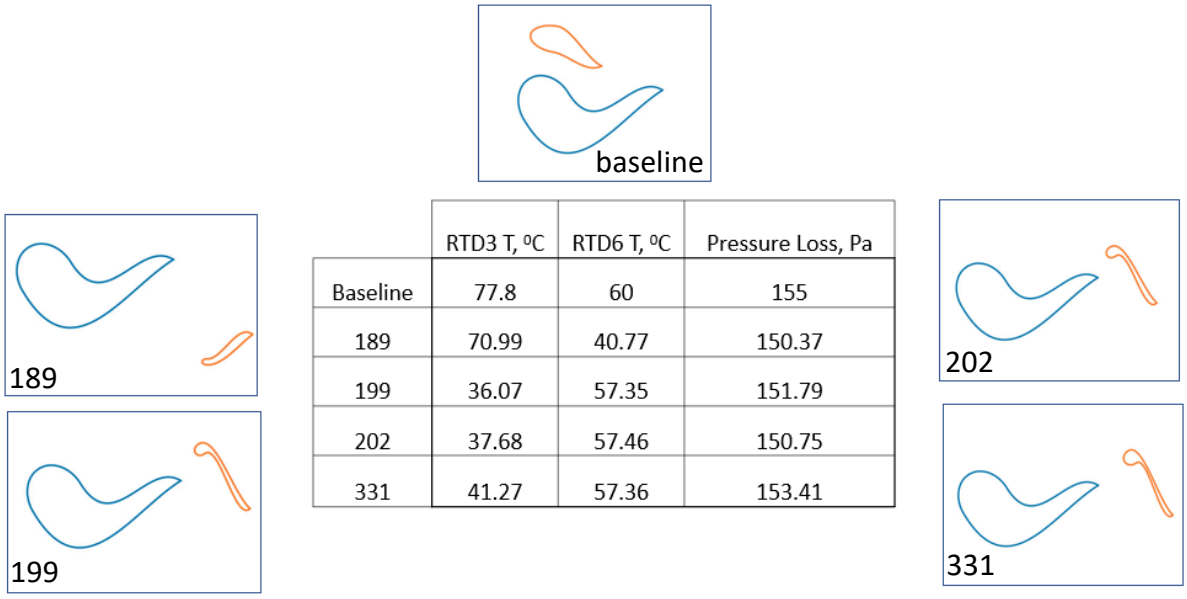

	RTD3 T, ºC	RTD6 T, ºC	Pressure Loss, Pa
Baseline	77.8	60	155
189	70.99	40.77	150.37
199	36.07	57.35	151.79
202	37.68	57.46	150.75
331	41.27	57.36	153.41

Figure 67 Comparison between selected members, Case 1

The evolution of the geometries in the higher Re numbers was investigated in the optimization utilizing boundary conditions of Case 2. 494 converged members are used to populate data, Figure 68. The Pareto front steepness is decreased compared to Case 1. Improved members in terms of RTD temperature are shown in Figure 69. This plot's pressure drop legend has a maximum equal to the baseline meaning all the designs marked by red dots has the same or worse hydraulic performance than baseline. Few members that have improved hydraulic performance were selected from Figure 69. Figure 70 summarizes the read RTD temperatures and pressure drops of these cases together with corresponding geometries. Note that, the RTD temperatures, in this case, is very close to the ones discussed in section 2.2., both numerically and experimentally. The reason behind this is the decay in conjugate effects on convective heat transfer. This also increases the confidence in the implementation of such geometries directly in experimental setups without further numerical conjugate heat transfer studies. The decrease in RTD temperatures is around 8^0C in average for all the cases. The increase in the offset between the main fin and the satellite is apparent in most cases, which is due to increased mass flow rate compared to Case 1. The trade-off between RTD temperatures between cases 115 and 231, 469 and 492. Notice that the lower RTD3 temperature corresponds to lower pressure drop values. To summarize, member 469 could be selected for further analysis and experimental investigation as it provides 11^0C difference for RTD3 temperature, 6.3^0C difference for RTD6 temperature with 12% pressure drop compared to baseline.

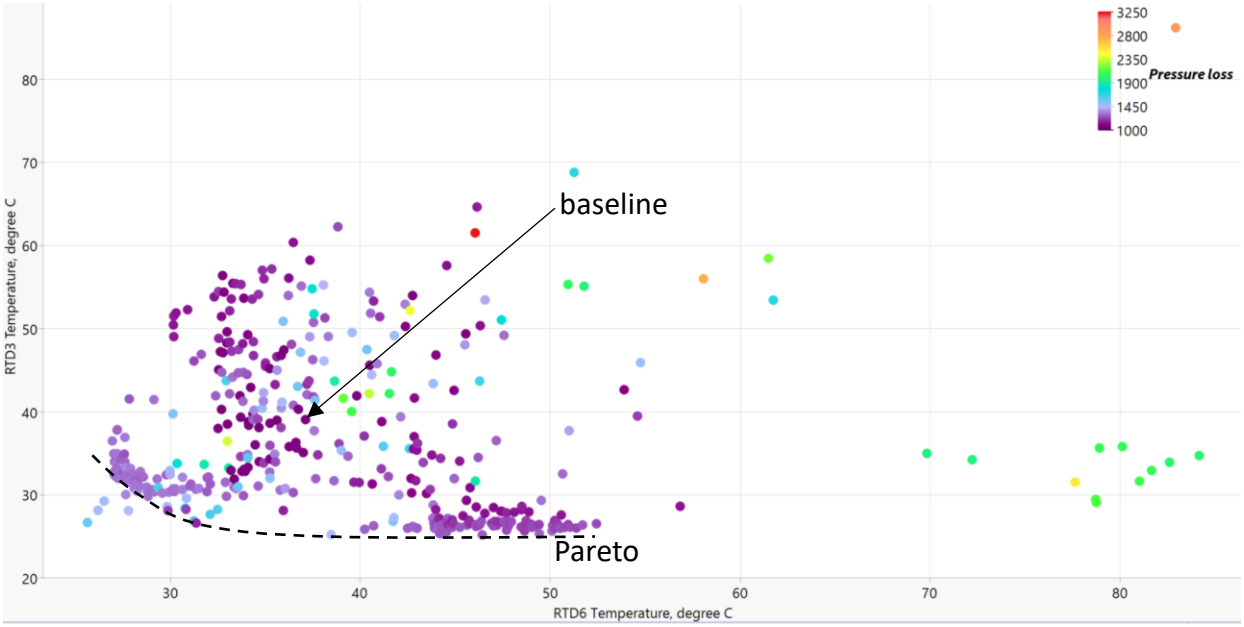

Figure 68 Optimization space, Case 2

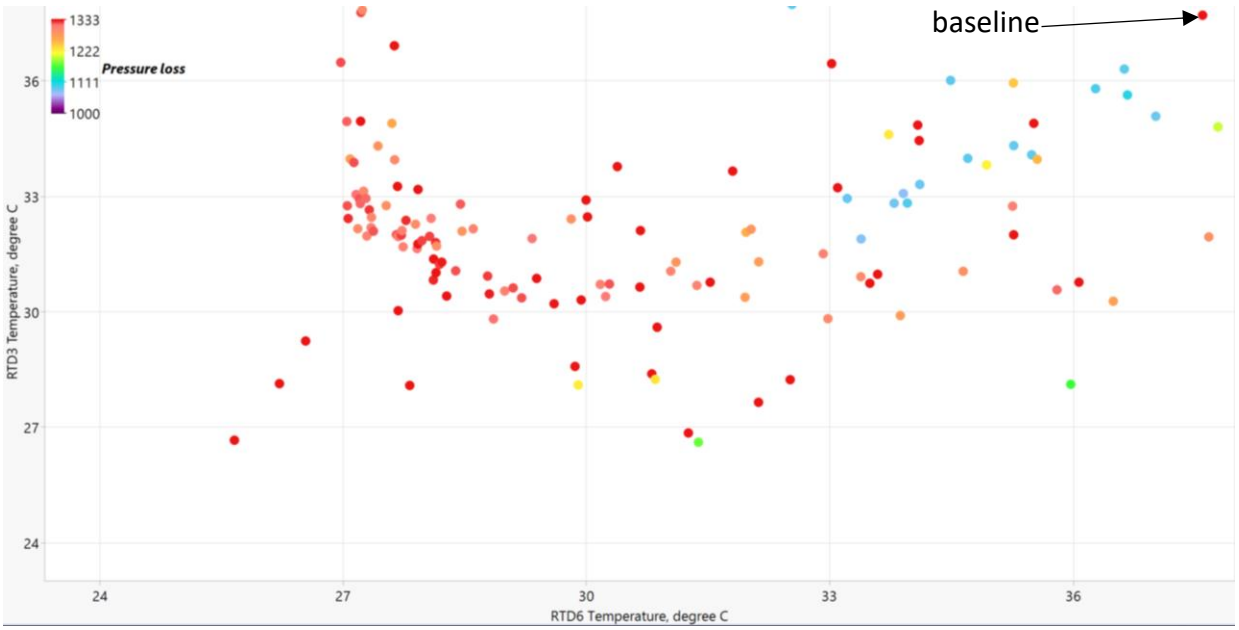

Figure 69 Improved member, Case 2.

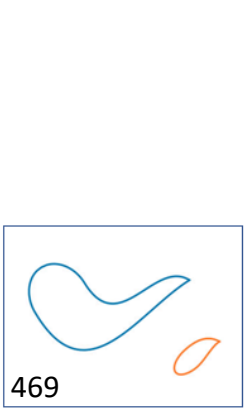

	RTD3 T, ºC	RTD6 T, ºC	Pressure Loss, Pa
Baseline	37.7	37.6	1333
115	28.10	29.90	1226.91
231	29.81	28.86	1317.65
469	26.61	31.38	1177.63
492	31.96	27.29	1306.18

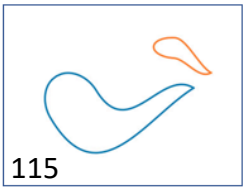

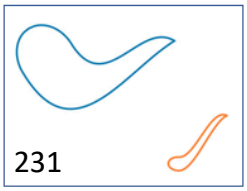

Figure 70 Comparison between selected members, Case 2.

CHAPTER 5. SUMMARY

5.1. Numerical Validation and its Importance

The importance of conjugate numerical modeling of micro heat sinks is caused by the miniature dimensions of the micro heat sinks and limited data acquisition ability. Mainly, average or few local temperatures could be measured during the experiments via implementing RTDs. The majority of the experimental data explaining heat transfer phenomena in the micro heat sink are obtained by applying various assumptions. Numerical modeling is crucial in verifying these assumptions and providing additional local behavior of the flow and heat transfer in the channel. The reliability of the conjugate numerical heat transfer models is identified based on the comparison with experimental results, which was within the acceptable range in this study. Validated numerical models revealed oversimplifications regarding the heat loss and local heat transfer coefficient calculations during the post-processing phase of the experimental data. The models provided additional information on the heat flow within the micro heat sink devices and stratification of the thermal boundary layer relative to the leading edge of the heater. Especially, Pr and Nu number variations resulted from temperature-dependent properties of HFE 7000 and HFE 7300 were discussed. The effect of conjugate effects on the thermal performance of the heat sinks was dependent on the operating Re numbers. These effects were decaying with increasing Re number irrespective of the solid thermal conductivity where solid thermal conductivity effects had dominance over convective heat transfer for low Re numbers. This behavior would be very useful in designing the micro heat sink flow channels with limited pumping power availabilities when minimum conjugate effects are desired. Also, various turbulence models were implemented and based on the deviation from experimental results, it could be stated that the lag EB turbulence model is very good at capturing flow and local heat transfer phenomena at various Re numbers. Gamma Re-theta transitional

model provides very similar flow patterns to experimentally obtained ones via μPIV, whereas it is less accurate than lag EB method in predicted surface temperatures. In lower Re numbers, where the turbulence is mainly local in the flow channel, both models provide acceptable predictions whereas at higher Re number only lag EB method is more effective.

5.2. Pin Fin Optimization

Most of the literature is evolving around traditional pin fin geometries entrenched in the micro heat sinks. The urgency for optimized fin geometries is apparent. This study provides a trade-off space between the thermal and hydraulic performance of the micro heat sinks under various thermal and hydraulic boundary conditions, covering multiple pin fin geometries derived from hydrofoil. It has been shown that better pin fin solutions are available, enhancing the heat transfer while keeping the pumping requirement within the acceptable range. The baseline for the studies were low Re number experimental data. Bird design fins are proposed increasing heat transfer coefficient 5%, where pressure drop increase is no more than 6%. Additional satellites included in the configuration and further optimization resulted in approximately 8% increase in heat transfer while the pressure drop increment was still 6%. This proved that the optimization cycles are an inseparable part of effective micro heat sink design together with experiments when single phase heat transfer is concerned. Further local heat transfer optimizations were performed at low and high Re numbers. The obtained pin fin configurations were different implying the importance of the Re number in optimizations. The heat transfer sensitivity against the chord, leading edge diameter and leading edge angle was reported. Finally, novel bird design with and without satellite was obtained with better thermal performance characteristics.

5.3. Future Work

Noting that the studies performed in this study are mainly evolving around the validated numerical models, few recommendations are made below based on space of pin fin geometries, obtained from local and global optimizations:

- ✓ The recommended pin fin geometries could be fabricated within the micro heat sinks, and predicted behavior by the optimizations could be verified via experiments.
- ✓ The performance of the micro heat sinks with bird design pin fins in flow boiling heat transfer should be investigated experimentally as current flow boiling numerical models are not providing reliable results.
- ✓ Optimization space could be used to train Artificial Intelligence, AI, codes and AI provided geometries could be investigated experimentally. Also, the performance of genetic algorithms could be compared to available AI techniques.

APPENDIX A:
DAKOTA RUN SETUPS—DESIGN OF COMPUTER EXPERIMENTS

```
environment,
tabular_data
tabular_data_file = 'DOE_results.dat'
method,
id_method '1'
dace LHS
samples = 150
model,
single
variables
id_variables = 'V1'
continuous_design = 6
descriptors
initial_point
lower_bounds
upper_bounds
scale_type = 'auto'
interface,
system
analysis_drivers = 'opt_driver.sh'
parameters_file = 'param'
results_file = 'rs'
file_tag
file_save
asynchronous
evaluation_concurrency = 1
responses
id_responses = 'R1'
descriptors = 'HTC_Ave'
num_objective_functions = 1
no gradients
no hessians
```

APPENDIX B:
DAKOTA RUN SETUPS—MULTI OBJECTIVE GENETIC ALGORITHM SETUP

```
method,
id_method '1'
#id_method = 'moga'
moga
output silent
seed = 12983
final_solution = 3
population_size = 10
max_function_evaluations = 1000
initialization_type unique_random
crossover_type shuffle_random
num_offspring = 2 num_parents = 2
crossover_rate = 0.8
mutation_type replace_uniform
mutation_rate = 0.3
fitness_type domination_count
replacement_type below_limit = 6
shrinkage_percentage = 0.9
niching_type distance = 10*0.01
convergence_type metric_tracker
percent_change = 0.05 num_generations = 50
```

APPENDIX C:
PYTHON CODE DEVELOPED FOR PARAMETRIZATION OF THE HYDROFOILS

```
import numpy as np
import math
import csv
import pylab as pl


## Defining x and y arrays for .csv file #
pts=50 #int(input("number_of_points_for_elipse "))
Pts_pol=50 #int(input("number_of_points_for_polynomials "))
A= 0.0001187 #float(input("a "))
a=-A
b= 0.0002789 #float(input("b "))
alpha=16.84325
origin=0.0 #float(input("origin "))
chord=0.00038 #0.000625 #float(input("chord "))
k2_ss=-29.7694000 #float(input("k2_ss" ))
k2_ps=29.76940 #float(input("k2_ps" ))
yend=0.0000583
sf=0.00031 #scale factor for satellite origin location
s1_x=123
s1_y=123
s2_x=92
s2_y=92

#total number needed for half-elipse
Pts_elps=2*pts

#calculating the marching step
step= 1*a/pts


x=np.zeros((2*pts+1,1))
y=np.zeros((2*pts+1,1))

for i in range (0, pts):
x[i,0]=origin+i*step
y[i,0]=((1-(x[i,0]/a)**2)*(b**2))**(1/2)

x[pts,0]=origin+a
y[pts,0]=origin
```

```
for j in range (pts+1, Pts_elps+1):
x[j,0]=origin+(-j+pts+pts)*step
y[j,0]=-1*((1-(x[j,0]/a)**2)*(b**2))**(1/2)



#matrices containing elipse coordinates
X_elps=np.zeros((2*pts+1,1))
Y_elps=np.zeros((2*pts+1,1))

for i in range (0, Pts_elps+1):
X_elps[i,0]=x[i,0]*math.cos(math.radians(alpha))-y[i,0]*math.sin(math.radians(alpha))
Y_elps[i,0]=y[i,0]*math.cos(math.radians(alpha))+x[i,0]*math.sin(math.radians(alpha))



############################ADDING POLYNOMIALS_SS################################

k1_ss= math.atan((Y_elps[1,0]-Y_elps[0,0])/(X_elps[1,0]-X_elps[0,0]))

ak1_ss=math.tan(k1_ss)
ak2_ss=math.tan(math.radians(k2_ss))


x2= chord - (origin-X_elps.min())
y2= yend
x1=X_elps[0,0]
y1=Y_elps[0,0]


a3=((ak1_ss+ak2_ss)*(x1-x2)-2*y1+2*y2)/((x1-x2)**3)
a2=(-ak1_ss*(x1-x2)*(x1+2*x2)+ak2_ss*(-2*(x1**2)+x1*x2+x2**2)+3*(x1+x2)*(y1-y2))/((x1-x2)**3)
a1=(ak2_ss*x1*(x1-x2)*(x1+2*x2)-x2*(ak1_ss*(-2*(x1**2)+x1*x2+x2**2)+6*x1*(y1-y2)))/((x1-x2)**3)
a0=(x2*(x1*(-x1+x2)*(ak2_ss*x1+ak1_ss*x2)-x2*(-3*x1+x2)*y1)+((x1**2)*(x1-3*x2)*y2))/((x1-x2)**3)

X_poly_ss=np.zeros((Pts_pol,1))
Y_poly_ss=np.zeros((Pts_pol,1))

step_poly=(X_elps[0,0]-x2)/Pts_pol

X_poly_ss[0,0]=x2
```

```
for i in range (0, Pts_pol):
X_poly_ss[i,0]=X_poly_ss[0,0]+i*step_poly
Y_poly_ss[i,0]=a3*(X_poly_ss[i,0]**3)+a2*(X_poly_ss[i,0]**2)+a1*X_poly_ss[i,0]+a0


############################ADDING POLYNOMIALS_PS################################

x1=X_elps[Pts_elps,0]
y1=Y_elps[Pts_elps,0]
x1s=X_elps[Pts_elps-1,0]
y1s=Y_elps[Pts_elps-1,0]
k1_ps= math.atan((y1-y1s)/(x1-x1s))

ak1_ps=math.tan(k1_ps)
ak2_ps=math.tan(math.radians(k2_ps))

a3=((ak1_ps+ak2_ps)*(x1-x2)-2*y1+2*y2)/((x1-x2)**3)
a2=(-ak1_ps*(x1-x2)*(x1+2*x2)+ak2_ps*(-2*(x1**2)+x1*x2+x2**2)+3*(x1+x2)*(y1-y2))/((x1-x2)**3)
a1=(ak2_ps*x1*(x1-x2)*(x1+2*x2)-x2*(ak1_ps*(-2*(x1**2)+x1*x2+x2**2)+6*x1*(y1-y2)))/((x1-x2)**3)
a0=(x2*(x1*(-x1+x2)*(ak2_ps*x1+ak1_ps*x2)-x2*(-3*x1+x2)*y1)+((x1**2)*(x1-3*x2)*y2))/((x1-x2)**3)

X_poly_ps=np.zeros((Pts_pol,1))
Y_poly_ps=np.zeros((Pts_pol,1))

step_poly=(x1-x2)/Pts_pol
X_poly_ps[0,0]=x2

for i in range (0, Pts_pol):
X_poly_ps[i,0]=X_poly_ps[0,0]+i*step_poly
Y_poly_ps[i,0]=a3*(X_poly_ps[i,0]**3)+a2*(X_poly_ps[i,0]**2)+a1*X_poly_ps[i,0]+a0

########## Summarizing the coordinates for hydrofoil pin-fin #################

T=Pts_elps+2*Pts_pol #total points that included in hydrofoil

X_H=np.zeros((T,1))
Y_H=np.zeros((T,1))

for i in range(0,T-Pts_elps-Pts_pol):
X_H[i,0]=X_poly_ss[i,0]
Y_H[i,0]=Y_poly_ss[i,0]
```

```
for i in range(T-Pts_elps-Pts_pol, T-Pts_pol):
X_H[i,0]=X_elps[i-Pts_pol,0]
Y_H[i,0]=Y_elps[i-Pts_pol,0]

for i in range(T-Pts_pol, T):
X_H[i,0]=X_poly_ps[Pts_pol+Pts_elps-1-i,0]
Y_H[i,0]=Y_poly_ps[Pts_pol+Pts_elps-1-i,0]


X_H_in_mm=X_H*1000
Y_H_in_mm=Y_H*1000

F=np.zeros((T,3)) #final array including x and y coordinates for hydrofoil

for i in range(0,T):
F[i,0]=X_H[i,0]
for j in range(0,T):
F[j,1]=Y_H[j,0]
for k in range(0,T):
F[k,2]=0.0
with open("new_file.csv", "w") as my_csv:
csvWriter = csv.writer(my_csv,delimiter=",", lineterminator='\n')
csvWriter.writerows(F)

################################################################################
###################### OFFSETTING and ORIGIN FOR SATELLITES ####################
################################################################################
O_Sat_X=np.zeros((T-2,1))
O_Sat_Y=np.zeros((T-2,1))
Offset_slope=np.zeros((T-2,1))

j=0
for i in range(1,T-1):
Offset_slope[j,0]=math.atan((Y_H[i+1,0]-Y_H[i-1,0])/(X_H[i+1,0]-X_H[i-1,0]))
j=j+1

for i in range(1,T-1):
DeltaX=X_H[i+1,0] - X_H[i-1,0]
DeltaY=Y_H[i+1,0] - Y_H[i-1,0]

if DeltaX>0.0 and DeltaY>0.0:
O_Sat_X[i-1,0]=X_H[i,0]+sf*math.sin(Offset_slope[i-1,0])
```

```
O_Sat_Y[i-1,0]=Y_H[i,0]-sf*math.cos(Offset_slope[i-1,0])
elif DeltaX<0.0 and DeltaY>0.0:
O_Sat_X[i-1,0]=X_H[i,0]-sf*math.sin(Offset_slope[i-1,0])
O_Sat_Y[i-1,0]=Y_H[i,0]+sf*math.cos(Offset_slope[i-1,0])

elif DeltaX<0.0 and DeltaY<0.0:
O_Sat_X[i-1,0]=X_H[i,0]-sf*math.sin(Offset_slope[i-1,0])
O_Sat_Y[i-1,0]=Y_H[i,0]+sf*math.cos(Offset_slope[i-1,0])

elif DeltaX>0.0 and DeltaY<0.0:
O_Sat_X[i-1,0]=X_H[i,0]+sf*math.sin(Offset_slope[i-1,0])
O_Sat_Y[i-1,0]=Y_H[i,0]-sf*math.cos(Offset_slope[i-1,0])


s1_x_origin=O_Sat_X[s1_x,0]
s1_y_origin=O_Sat_Y[s1_y,0]
s2_x_origin=O_Sat_X[s2_x,0]
s2_y_origin=O_Sat_Y[s2_y,0]


OX=O_Sat_X*1000
OY=O_Sat_Y*1000

############################## SATELLITE 1 ####################################

## Defining x and y arrays for .csv file #
pts=100 #int(input("number_of_points_for_elipse "))
Pts_pol=50 #int(input("number_of_points_for_polynomials "))
A= 0.0000338 #float(input("a "))
a=-A
b= 0.0000794 #float(input("b "))
alpha=21.95085
gamma=4.13928
chord=0.00024 #0.000625 #float(input("chord "))
k2_ss=-29.7694000 #float(input("k2_ss" ))
k2_ps=29.76940 #float(input("k2_ps" ))

#total number needed for half-elipse
Pts_elps=2*pts

#calculating the marching step
step= a/pts
```

```
x=np.zeros((2*pts+1,1))
y=np.zeros((2*pts+1,1))

for i in range (0, pts):
x[i,0]=s1_x_origin+i*step
y[i,0]=((1-((x[i,0]-s1_x_origin)/a)**2)*(b**2))**(1/2)+s1_y_origin

x[pts,0]=s1_x_origin+a
y[pts,0]=s1_y_origin

for j in range (pts+1, Pts_elps+1):
x[j,0]=s1_x_origin+(-j+pts+pts)*step
y[j,0]=-1*((1-((x[j,0]-s1_x_origin)/a)**2)*(b**2))**(1/2)+s1_y_origin

X_elps=np.zeros((2*pts+1,1))
Y_elps=np.zeros((2*pts+1,1))

for i in range (0, Pts_elps+1):
X_elps[i,0]=x[i,0]*math.cos(math.radians(alpha))-y[i,0]*math.sin(math.radians(alpha))
Y_elps[i,0]=y[i,0]*math.cos(math.radians(alpha))+x[i,0]*math.sin(math.radians(alpha))

#ADDING POLYNOMIALS
k1_ss= math.atan((Y_elps[1,0]-Y_elps[0,0])/(X_elps[1,0]-X_elps[0,0]))
ak1_ss=math.tan(k1_ss)
ak2_ss=math.tan(math.radians(k2_ss))
x2= chord*math.cos(math.radians(alpha))+X_elps.min()

#########y_end_definition#############################################################
g=(np.abs(O_Sat_X-x2)).argmin()
egim=math.atan((O_Sat_Y[g,0]-O_Sat_Y[s1_y,0])/(O_Sat_X[g,0]-O_Sat_X[s1_x,0]))
yend=(x2-O_Sat_X[s1_x,0])*math.tan(egim+math.radians(gamma))+O_Sat_Y[s1_y,0]
if np.sign(O_Sat_Y[s1_y,0])==np.sign(O_Sat_Y[g,0]):
y2=yend
elif np.sign(O_Sat_Y[s1_y,0])!=np.sign(O_Sat_Y[g,0]):
y2=-yend
#####################################################################################


x1=X_elps[0,0]
y1=Y_elps[0,0]
a3=((ak1_ss+ak2_ss)*(x1-x2)-2*y1+2*y2)/((x1-x2)**3)
```

```
a2=(-ak1_ss*(x1-x2)*(x1+2*x2)+ak2_ss*(-2*(x1**2)+x1*x2+x2**2)+3*(x1+x2)*(y1-y2))/((x1-x2)**3)
a1=(ak2_ss*x1*(x1-x2)*(x1+2*x2)-x2*(ak1_ss*(-2*(x1**2)+x1*x2+x2**2)+6*x1*(y1-y2)))/((x1-x2)**3)
a0=(x2*(x1*(-x1+x2)*(ak2_ss*x1+ak1_ss*x2)-x2*(-3*x1+x2)*y1)+((x1**2)*(x1-3*x2)*y2))/((x1-x2)**3)
X_poly_ss=np.zeros((Pts_pol,1))
Y_poly_ss=np.zeros((Pts_pol,1))
step_poly=(X_elps[0,0]-x2)/Pts_pol
X_poly_ss[0,0]=x2

for i in range (0, Pts_pol):
X_poly_ss[i,0]=X_poly_ss[0,0]+i*step_poly
Y_poly_ss[i,0]=a3*(X_poly_ss[i,0]**3)+a2*(X_poly_ss[i,0]**2)+a1*X_poly_ss[i,0]+a0

x1=X_elps[Pts_elps,0]
y1=Y_elps[Pts_elps,0]
x1s=X_elps[Pts_elps-1,0]
y1s=Y_elps[Pts_elps-1,0]
k1_ps= math.atan((y1-y1s)/(x1-x1s))
ak1_ps=math.tan(k1_ps)
ak2_ps=math.tan(math.radians(k2_ps))
a3=((ak1_ps+ak2_ps)*(x1-x2)-2*y1+2*y2)/((x1-x2)**3)
a2=(-ak1_ps*(x1-x2)*(x1+2*x2)+ak2_ps*(-2*(x1**2)+x1*x2+x2**2)+3*(x1+x2)*(y1-y2))/((x1-x2)**3)
a1=(ak2_ps*x1*(x1-x2)*(x1+2*x2)-x2*(ak1_ps*(-2*(x1**2)+x1*x2+x2**2)+6*x1*(y1-y2)))/((x1-x2)**3)
a0=(x2*(x1*(-x1+x2)*(ak2_ps*x1+ak1_ps*x2)-x2*(-3*x1+x2)*y1)+((x1**2)*(x1-3*x2)*y2))/((x1-x2)**3)
X_poly_ps=np.zeros((Pts_pol,1))
Y_poly_ps=np.zeros((Pts_pol,1))
step_poly=(x1-x2)/Pts_pol
X_poly_ps[0,0]=x2

for i in range (0, Pts_pol):
X_poly_ps[i,0]=X_poly_ps[0,0]+i*step_poly
Y_poly_ps[i,0]=a3*(X_poly_ps[i,0]**3)+a2*(X_poly_ps[i,0]**2)+a1*X_poly_ps[i,0]+a0

T=Pts_elps+2*Pts_pol #total points that included in hydrofoil
X_H=np.zeros((T,1))
Y_H=np.zeros((T,1))
for i in range(0,T-Pts_elps-Pts_pol):
X_H[i,0]=X_poly_ss[i,0]
Y_H[i,0]=Y_poly_ss[i,0]

for i in range(T-Pts_elps-Pts_pol, T-Pts_pol):
X_H[i,0]=X_elps[i-Pts_pol,0]
Y_H[i,0]=Y_elps[i-Pts_pol,0]
```

```
for i in range(T-Pts_pol, T):
X_H[i,0]=X_poly_ps[Pts_pol+Pts_elps-1-i,0]
Y_H[i,0]=Y_poly_ps[Pts_pol+Pts_elps-1-i,0]
s1_X_H_in_mm=X_H*1000
s1_Y_H_in_mm=Y_H*1000

Fs1=np.zeros((T,3)) #final array including x and y coordinates for hydrofoil

for i in range(0,T):
Fs1[i,0]=X_H[i,0]
for j in range(0,T):
Fs1[j,1]=Y_H[j,0]
for k in range(0,T):
Fs1[k,2]=0.0

with open("new_file1.csv", "w") as my_csv:
csvWriter = csv.writer(my_csv,delimiter=",", lineterminator='\n')
csvWriter.writerows(Fs1)
############################## SATELLITE 2 ####################################

## Defining x and y arrays for .csv file #
pts=100 #int(input("number_of_points_for_elipse "))
Pts_pol=50 #int(input("number_of_points_for_polynomials "))
A= 0.0000322 #float(input("a "))
a=-A
b= 0.0000757 #float(input("b "))
alpha=9.42989
gamma=-7.84889
chord=0.00014 #0.000625 #float(input("chord "))
k2_ss=-29.7694000 #float(input("k2_ss" ))
k2_ps=29.76940 #float(input("k2_ps" ))
#total number needed for half-elipse
Pts_elps=2*pts

#calculating the marching step
step= 1*a/pts

x=np.zeros((2*pts+1,1))
y=np.zeros((2*pts+1,1))

for i in range (0, pts):
```

```
x[i,0]=s2_x_origin+i*step
y[i,0]=((1-((x[i,0]-s2_x_origin)/a)**2)*(b**2))**(1/2)+s2_y_origin

x[pts,0]=s2_x_origin+a
y[pts,0]=s2_y_origin


for j in range (pts+1, Pts_elps+1):
x[j,0]=s2_x_origin+(-j+pts+pts)*step
y[j,0]=-1*((1-((x[j,0]-s2_x_origin)/a)**2)*(b**2))**(1/2)+s2_y_origin

#matrices containing elipse coordinates
X_elps=np.zeros((2*pts+1,1))
Y_elps=np.zeros((2*pts+1,1))

for i in range (0, Pts_elps+1):
X_elps[i,0]=x[i,0]*math.cos(math.radians(alpha))-y[i,0]*math.sin(math.radians(alpha))
Y_elps[i,0]=y[i,0]*math.cos(math.radians(alpha))+x[i,0]*math.sin(math.radians(alpha))

#ADDING POLYNOMIALS
k1_ss= math.atan((Y_elps[1,0]-Y_elps[0,0])/(X_elps[1,0]-X_elps[0,0]))
ak1_ss=math.tan(k1_ss)
ak2_ss=math.tan(math.radians(k2_ss))
x2= chord*math.cos(math.radians(alpha))+X_elps.min()

##########y_end_definition#############################################################
z=(np.abs(O_Sat_X-x2)).argmin()
egim=math.atan((O_Sat_Y[z,0]-O_Sat_Y[s2_y,0])/(O_Sat_X[z,0]-O_Sat_X[s2_x,0]))
yend=(x2-O_Sat_X[s2_x,0])*math.tan(egim+math.radians(gamma))+O_Sat_Y[s2_y,0]
if np.sign(O_Sat_Y[s2_y,0])==np.sign(O_Sat_Y[z,0]):
y2=yend
elif np.sign(O_Sat_Y[s2_y,0])!=np.sign(O_Sat_Y[z,0]):
y2=-yend

x1=X_elps[0,0]
y1=Y_elps[0,0]
a3=((ak1_ss+ak2_ss)*(x1-x2)-2*y1+2*y2)/((x1-x2)**3)
a2=(-ak1_ss*(x1-x2)*(x1+2*x2)+ak2_ss*(-2*(x1**2)+x1*x2+x2**2)+3*(x1+x2)*(y1-y2))/((x1-x2)**3)
a1=(ak2_ss*x1*(x1-x2)*(x1+2*x2)-x2*(ak1_ss*(-2*(x1**2)+x1*x2+x2**2)+6*x1*(y1-y2)))/((x1-x2)**3)
a0=(x2*(x1*(-x1+x2)*(ak2_ss*x1+ak1_ss*x2)-x2*(-3*x1+x2)*y1)+((x1**2)*(x1-3*x2)*y2))/((x1-x2)**3)
X_poly_ss=np.zeros((Pts_pol,1))
Y_poly_ss=np.zeros((Pts_pol,1))
```

```
step_poly=(X_elps[0,0]-x2)/Pts_pol
X_poly_ss[0,0]=x2

for i in range (0, Pts_pol):
X_poly_ss[i,0]=X_poly_ss[0,0]+i*step_poly
Y_poly_ss[i,0]=a3*(X_poly_ss[i,0]**3)+a2*(X_poly_ss[i,0]**2)+a1*X_poly_ss[i,0]+a0

x1=X_elps[Pts_elps,0]
y1=Y_elps[Pts_elps,0]
x1s=X_elps[Pts_elps-1,0]
y1s=Y_elps[Pts_elps-1,0]
k1_ps= math.atan((y1-y1s)/(x1-x1s))
ak1_ps=math.tan(k1_ps)
ak2_ps=math.tan(math.radians(k2_ps))
a3=((ak1_ps+ak2_ps)*(x1-x2)-2*y1+2*y2)/((x1-x2)**3)
a2=(-ak1_ps*(x1-x2)*(x1+2*x2)+ak2_ps*(-2*(x1**2)+x1*x2+x2**2)+3*(x1+x2)*(y1-y2))/((x1-x2)**3)
a1=(ak2_ps*x1*(x1-x2)*(x1+2*x2)-x2*(ak1_ps*(-2*(x1**2)+x1*x2+x2**2)+6*x1*(y1-y2)))/((x1-x2)**3)
a0=(x2*(x1*(-x1+x2)*(ak2_ps*x1+ak1_ps*x2)-x2*(-3*x1+x2)*y1)+((x1**2)*(x1-3*x2)*y2))/((x1-x2)**3)
X_poly_ps=np.zeros((Pts_pol,1))
Y_poly_ps=np.zeros((Pts_pol,1))
step_poly=(x1-x2)/Pts_pol
X_poly_ps[0,0]=x2

for i in range (0, Pts_pol):
X_poly_ps[i,0]=X_poly_ps[0,0]+i*step_poly
Y_poly_ps[i,0]=a3*(X_poly_ps[i,0]**3)+a2*(X_poly_ps[i,0]**2)+a1*X_poly_ps[i,0]+a0

T=Pts_elps+2*Pts_pol #total points that included in hydrofoil
X_H=np.zeros((T,1))
Y_H=np.zeros((T,1))
for i in range(0,T-Pts_elps-Pts_pol):
X_H[i,0]=X_poly_ss[i,0]
Y_H[i,0]=Y_poly_ss[i,0]

for i in range(T-Pts_elps-Pts_pol, T-Pts_pol):
X_H[i,0]=X_elps[i-Pts_pol,0]
Y_H[i,0]=Y_elps[i-Pts_pol,0]

for i in range(T-Pts_pol, T):
X_H[i,0]=X_poly_ps[Pts_pol+Pts_elps-1-i,0]
Y_H[i,0]=Y_poly_ps[Pts_pol+Pts_elps-1-i,0]
```

```
s2_X_H_in_mm=X_H*1000
s2_Y_H_in_mm=Y_H*1000

Fs2=np.zeros((T,3)) #final array including x and y coordinates for hydrofoil

for i in range(0,T):
Fs2[i,0]=X_H[i,0]
for j in range(0,T):
Fs2[j,1]=Y_H[j,0]
for k in range(0,T):
Fs2[k,2]=0.0

with open("new_file2.csv", "w") as my_csv:
csvWriter = csv.writer(my_csv,delimiter=",", lineterminator='\n')
csvWriter.writerows(Fs2)

pl.figure(figsize=(7,7), dpi=1500)
pl.plot(X_H_in_mm,Y_H_in_mm)
#pl.plot(s1_X_H_in_mm,s1_Y_H_in_mm)
#pl.plot(OX,OY)
pl.plot(s1_X_H_in_mm,s1_Y_H_in_mm)
pl.plot(s2_X_H_in_mm,s2_Y_H_in_mm)
pl.title('Hydrofoil Shape')
pl.xlim(-1.0,1.0)
pl.ylim(-1.0,1.0)
pl.xlabel('x, mm')
pl.ylabel('y, mm')
pl.savefig('Case ' + str(chord) +' ' +str(a) +' ' +str(b) +' ' +str(k2_ss) +' ' +str(k2_ps) +' ' +str(alpha) +'.png')
```

REFERENCES

[1] D. B. Tuckerman and R. F. W. Pease, “High-performance heat sinking for VLSI,‖ IEEE Electron Device Letters, vol. 2, no. 5, pp. 126–129, May 1981.

[2] S. G. Kandlikar, “History, Advances, and Challenges in Liquid Flow and Flow Boiling Heat Transfer in Microchannels: A Critical Review,” ASME J. Heat Transf., vol. 134, no. 3, pp. 034001–1, 2012.

[3] Peng, X. F., Peterson, G. P., and Wang, B. X., “Frictional Flow Characteristics of Water Flowing Through Rectangular Microchannels,” Exp. Heat Transfer, 7(4), pp. 249–264, 1994.

[4] Peng, X. F., Peterson, G. P., and Wang, B. X., “Heat Transfer Characteristics of Water Flowing Through Microchannels,” Exp. Heat Transfer, 7(4), pp.350-380, 1994.

[5] S. S. Mehendale, A. M. Jacobi, and R. K. Shah, “Fluid Flow and Heat Transfer at Micro and Meso Scales With Application to Heat Exchanger Design,” Appl. Mech. Rev., vol. 53, no. 7, p. 175, 2000.

[6] Steinke, M. E., and Kandlikar, S. G., 2006, “Single-Phase Liquid Friction Factors in Microchannels,” Int. J. Therm. Sci., 45(11), pp. 1073–1083.

[7] Lee, P.-S., Garimella, V., and Dong, L., 2005, “Investigation of Heat Transfer in Rectangular Microchannels,” Int. J. Heat Mass Transfer, 48(9), pp. 1688–1704.

[8] H.E. Hegab, A. Bari, T. Ameel, “Friction and convection studies of R134a in microchennels within the transition and turbulent flow regimes”, Exp. Heat Transfer 15 (2002) 245–259

[9] M. Richter, P. Woias, D. Weiß, “Microchannels for applications in liquid dosing and flow-rate measurements”, Sensors Actuators A 62 (1997) 480–483.

[10] T.M. Harms, M.J. Kazmierczak, F.M. Gerner, A. Holke, H.T. Hen- derson, J. Pilchowski, K. Baker, “Experimental investigation of heat transfer and pressure drop through deep microchannels in a silicon substrate”, Proceedings of ASME Heat Transfer Division, in: ASME HTD, vol. 351-1, 1997, pp. 347–357.

[11] T.M. Harms, M.J. Kazmierczak, F.M. Gerner, “Developing convective heat transfer in deep rectangular microchannels”, Internat. J. Heat Fluid Flow 20 (1999) 149–157.

[12] R.L. Webb, M. Zhang, “Heat transfer and friction in small diameters channels”, Microscale Termophys. Engrg. 2 (1998) 189–202.

[13] D.A. Pfund, A. Shekarriz, A. Popescu, J.R. Welty, “Pressure drops measurements in microchannels”, Proceedings of MEMS, ASME DSC, vol. 66, 1998, pp. 193–198.

[14] B. Xu, K.T. Ooi, N.T. Wong, W.K. Choi, “Experimental investigation of flow friction for liquid flow in microchannels”, Internat. Comm. Heat Mass Transfer 27 (2000) 1165–1176.

[15] S.M. Flockhart, R.S. Dhariwal, “Experimental and numerical investigation into the flow characteristics of channels etched in silicon”, J. Fluid Engrg. 120 (1998) 291–295

[16] P. Gao, S. Le Person, M. Favre-Marinet, Scale effects on hydrody- namics and heat transfer in two-dimensional mini and microchannels, Internat. J. Thermal Sci. 41 (2002) 1017–1027.

[17] G.R. Warrier, V.K. Dhir, L.A. Momoda, "Heat transfer and pressure drop in narrow rectangular channels", Exp. Thermal Fluid Sci. 26 (2002) 53–64.

[18] J. Judy, D. Maynes, B.W.Webb, "Characterization of frictional pressure drop for liquid flows through microchannels", Internat. J. Heat Mass Transfer

[19] H.Y. Wu, P. Cheng, "Friction factors in smooth trapezoidal silicon microchannels with different aspect ratios", Internat. J. Heat Mass Transfer

[20] T.M. Harms, M.J. Kazmierczak, F.M. Gerner, "Developing convective heat transfer in deep rectangular microchannels", Internat. J. Heat Fluid Flow 20 (1999) 149–157.

[21] H.Y.Wu, P. Cheng, "An experimental study of convective heat transfer in silicon microchannels with different surface conditions", Internat. J. Heat Mass Transfer 46 (2003) 2547–2556

[22] Balaras C.A., "Review of augmentation techniques for heat transfer surfaces in single-phase heat exchangers", Energy (Oxford), vol. 15, no. 10, pp 899-906, 1990

[23] Bergles A.E., Jensen M.K., and B. Shome, "The literature on enhancement convective heat and mass transfer", Enhanced heat transfer, vol.4 pp1-6, 1994

[24] M. E. Steinke and S. G. Kandlikar, "Review of single-phase heat transfer enhancement techniques for application in microchannels, minichannels and microdevices," International Journal of Heat and Technology, vol. 22, no. 2. pp. 3–11, 2004.

[25] W. Q. Tao, Y. L. He, Q. W. Wang, Z. G. Qu, and F. Q. Song, "A unified analysis on enhancing single phase convective heat transfer with field synergy principle," Int. J. Heat Mass Transf., vol. 45, no. 24, pp. 4871–4879, 2002

[26] Colgan, E. G., Furman, B., Gaynes, M., Graham, W., Labianca, N., Magerlein, J. H., Polastre, R. J., Rothwell, M. B., Bezama, R. J., Choudhary, R., Marston, K., Toy, H., Wakil, J., Zitz, J., and Schmidt, R., "A Practical Implementation of Silicon Microchannel Coolers for High Power Chips," Proc. 21st An- nual IEEE Semiconductor Thermal Measurement and Management Symposium, March 15–17, 2005, San Jose, CA, pp. 1–7

[27] Steinke, M. E., and Kandlikar, S. G., 2006, "Single-Phase Liquid Heat Transfer in Plain and Enhanced Microchannels," Paper No. ICNMM2006- 96227, ASME Fourth International Conference on Nanochannels, Micro- channels and Minichannels, June 19–21, Limerick, Ireland, 2006B, pp. 943–951.

[28] A. Koşar and Y. Peles, "Thermal-Hydraulic Performance of MEMS-based Pin Fin Heat Sink," J. Heat Transfer, vol. 128, no. 2, p. 121, 2006.

[29] Lee, Y., Lee, P., and Chou, S., Enhanced Microchannel Heat Sinks Using Oblique Fins, Proceedings of ASME IPACK2009–89059, San Francisco, CA, 2009.

[30] Tsuzuki, N., Kato, Y., Nikitin, K., and Ishizuka, T., 2009, "Advanced Micro- channel Heat Exchanger With S-Shaped Fins," J. Nucl. Sci. Technol., 46(5), pp. 403–412.

[31] Y. Wang, F. Houshmand, D. Elcock, and Y. Peles, “Convective heat transfer and mixing enhancement in a microchannel with a pillar,” Int. J. Heat Mass Transf., vol. 62, no. 1, pp. 553–561, 2013.

[32] X. Yu, C. Woodcock, J. Plawsky, and Y. Peles, “An investigation of convective heat transfer in microchannel with Piranha Pin Fin,” Int. J. Heat Mass Transf., vol. 103, pp. 1125–1132, 2016.

[33] Vanapalli, S., Ter Brake, H. J. M., Jansen, H. V., Burger, J. F., Holland, H. J., Veenstra, T. T., and Elwenspoek, M. C., “Pressure Drop of Laminar Gas Flows in a Microchannel Containing Various Pillar Matrices”, Journal of Micromechanics and Microengineering, vol. 17, pp. 1381–1386, 2007.

[34] A. Koşar and Y. Peles, “Boiling heat transfer in a hydrofoil-based micro pin fin heat sink,” Int. J. Heat Mass Transf., vol. 50, no. 5–6, pp. 1018–1034, 2007.

[35] Moriyama, K., Inoue, A., and Ohira, H., 1992, “Thermohydraulic Characteristics of Two-Phase Flow in Extremely Narrow Channels (the Frictional Pres- sure Drop and Void Fraction of Adiabatic Two-Component Two-Phase Flow),” Heat Transfer–Jpn. Res., 21(8), pp. 823–837.

[36] Serizawa, A., Feng, Z., and Kawara, Z., 2002, “Two-Phase Flow in Microchannels,” Exp. Therm. Fluid Sci., 26(6–7), pp. 703–714.

[37] Hetsroni, G., Mosyak, A., and Segal, Z., 2000, “Nonuniform Temperature Distribution in Electronic Devices Cooled by Flow in Parallel Microchannels,” IEEE Trans. Compon. Packag. Technol., 24(1), pp. 16–23.

[38] Bertsch, S. S., Groll, E. A., and Garimella, S. V., 2008, “Review and Comparative Analysis of Studies on Saturated Flow Boiling in Small Channels,” Nanoscale Microscale Thermophys. Eng., 12(2), pp. 187–227.

[39] Ribatski, G., Wojtan, L., and Thome, J. R., 2006, “An Analysis of Experimental Data and Prediction Methods for Two-Phase Frictional Pressure Drop and Flow Boiling Heat Transfer in Micro-Scale Channels,” Exp. Therm. Fluid Sci., 31(1), pp. 1–19.

[40] Shiferaw, D., Huo, X., Karayiannis, T. G., and Kenning, D. B. R., 2007, “Examination of Heat Transfer Correlations and a Model for Flow Boiling of R134a in Small Diameter Tubes,” Int. J. Heat Mass Transfer, 50(25–26), pp. 5177–5193.

[41] Sun, L., and Mishima, K., 2009, “An Evaluation of Prediction Methods for Saturated Flow Boiling Heat Transfer in Mini-Channels,” Int. J. Heat Mass Transfer, 52(23–24), pp. 5323–5329.

[42] A. Koşar, C.-J. Kuo, and Y. Peles, “Suppression of Boiling Flow Oscillations in Parallel Microchannels by Inlet Restrictors,” J. Heat Transfer, vol. 128, no. 3, p. 251, 2006.

[43] Kandlikar, S. G., 2003, “Methods for Stabilizing Flow in Channels and Systems Thereof,” US Patent Application No. 20090266436.

[44] Kandlikar, S. G., Kuan, W. K., Willistein, D. A., and Borrelli, J., 2006, “Stabilization of Flow Boiling in Microchannels Using Pressure Drop Elements and Fabricated Nucleation Sites,” ASME J. Heat Transfer, 128(4), pp. 389–396.

[45] C.B. Tibirica, G. Ribatski, Flow boiling in micro-scale channels — synthesized literature review, Int. J. Refrig. 36 (2013) 301–324.

[46] S. Krishnamurthy, Y. Peles, “Flow boiling heat transfer on micro pin fins entrenched in a microchannel”, J. Heat Transfer 132 (Apr. 2010).

[47] S. Krishnamurthy, Y. Peles, “Flow boiling of water in a circular staggered micro- pin fin heat sink”, Int. J. Heat Mass Transfer 51 (2008) 1349–1364.

[48] Y. Lie, J. Ke, W. Chang, T. Cheng, T. Lin, “Saturated flow boiling heat transfer and associated bubble characteristics of FC-72 on a heated micro-pin-finned silicon chip”, Int. J. Heat Mass Transfer 50 (2007) 3862–3876.

[49] D. McNeil, A. Raeisi, P. Kew, P. Bobbili, “A comparison of flow boiling heat- transfer in in-line mini pin fin and plane channel flows”, Appl. Therm. Eng. 30 (2010) 2412–2425.

[50] A. Koşar, C.-J. Kuo, and Y. Peles, “Reduced Pressure Boiling Heat Transfer in Rectangular Microchannels With Interconnected Reentrant Cavities,” J. Heat Transfer, vol. 127, no. 10, p. 1106, 2005.

[51] C. Woodcock, X. Yu, J. Plawsky, and Y. Peles, “Piranha Pin Fin (PPF) - Advanced flow boiling microstructures with low surface tension dielectric fluids,” Int. J. Heat Mass Transf., vol. 90, pp. 591–604, 2015.

[52] W. Nakayama, M. Behnia, D. Soodphakdee, “Management of uncertainty in microchannels heat transfer”. Paper presented at the Microscale Thermophysical Engineering Workshop, Kyongju, Korea, August 1998

[53] Kiran K. Ambatipudi, Muhammad M. Ra, “Analysis of Conjugate Heat Transfer in Microchannel Heat Sinks,” Numer. Heat Transf. Appl., vol. 37, no. 7, pp. 711–731, 2000.

[54] W. Qu and I. Mudawar, “Experimental and numerical study of pressure drop and heat transfer in a single-phase micro-channel heat sink,” Int. J. Heat Mass Transf., vol. 45, no. 12, pp. 2549–2565, 2002.

[55] Zhuo Li, Wen-Quan Tao and Ya-Ling He, “A Numerical Study of Laminar Convective Heat Transfer in Microchannel With Non-Circular Cross-Section” ASME 3rd International Conference on Microchannels and Minichannels, 2005

[56] H.K. Versteeg, W. Malalasekera, “An Introduction to Computational Fluid Dynamics. The Finite volume Method” Second edition, Pearson Prentice Hall, 2007

[57] W. K. S. Chiu, C. J. Richards, and Y. Jaluria, “Experimental and Numerical Study of Conjugate Heat Transfer in a Horizontal Channel Heated From Below,” J. Heat Transfer, vol. 123, no. 4, p. 688, 2001.

[58] D. Lelea, S. Nishio, K. Takano, “The experimental research on microtube heat transfer and fluid flow of distilled water”, Int. J. Heat Mass Transfer 47 (2004) 2817–2830.

[59] G. Gamrat, M. Favre-Marinet, and D. Asendrych, “Conduction and entrance effects on laminar liquid flow and heat transfer in rectangular microchannels,” Int. J. Heat Mass Transf., vol. 48, no. 14, pp. 2943–2954, 2005.

[60] P. Rosa, T. G. Karayiannis, and M. W. Collins, “Single-phase heat transfer in microchannels: The importance of scaling effects,” Appl. Therm. Eng., vol. 29, no. 17–18, pp. 3447–3468, 2009.

[61] M. M. Mansoor, K.-C. Wong, and M. Siddique, “Numerical investigation of fluid flow and heat transfer under high heat flux using rectangular microchannels,” Int. Commun. Heat Mass Transf., vol. 39, no. 2, pp. 291–297, 2012.

[62] Shah, R. K., and London, A. L., “Laminar Flow Forced Convection in Ducts: A Source Book for Compact Heat Exchanger Analytical Data”, Academic, New York, p. 477.

[63] D. C. Knupp, R. M. Cotta, and C. P. Naveira-Cotta, “Heat Transfer in Microchannels with Upstream–Downstream Regions Coupling and Wall Conjugation Effects,” Numer. Heat Transf. Part B Fundam., vol. 64, no. 5, pp. 365–387, 2013.

[64] D. C. Knupp, R. M. Cotta, C. P. Naveira-Cotta, and S. Kaka, “Transient conjugated heat transfer in microchannels: Integral transforms with single domain formulation,” Int. J. Therm. Sci., vol. 88, pp. 248–257, 2015.

[65] H. S. Gaikwad, P. K. Mondal, and S. Wongwises, “Non-linear drag induced entropy generation analysis in a microporous channel: The effect of conjugate heat transfer,” Int. J. Heat Mass Transf., vol. 108, pp. 2217–2228, 2017.

[66] M. Dehghan, M. S. Valipour, and S. Saedodin, “Conjugate Heat Transfer Inside Microchannels Filled with Porous Media: An Exact Solution,” J. Thermophys. Heat Transf., vol. 30, no. 4, pp. 814–824, 2016.

[67] M. Dehghan, M. S. Valipour, and S. Saedodin, “Microchannels enhanced by porous materials: Heat transfer enhancement or pressure drop increment,” Energy Convers. Manag., vol. 110, pp. 22–32, 2016.

[68] A. G. Fedorov and R. Viskanta, “Three-dimensional conjugate heat transfer in the microchannel heat sink for electronic packaging,” Int. J. Heat Mass Transf., vol. 43, pp. 399–415, 2000.

[69] J. Li, G. P. Peterson, and P. Cheng, “Three-dimensional analysis of heat transfer in a micro-heat sink with single phase flow,” Int. J. Heat Mass Transf., vol. 47, no. 19–20, pp. 4215–4231, 2004.

[70] X.F. Peng, G.P. Peterson, “The effect of thermofluid and geometrical parameters on convection of liquids through rectangular microchannels”, Int. J. Heat Mass Transfer 38 (1995) 755–758.

[71] M. Richter, P. Woias, D. Weiß, “Microchannels for applications in liquid dosing and flow-rate measurements”, Sens. Actuators A62 pp 480–483, 1997.

[72] C.P. Tso, S.P. Mahulikar, “Experimental verification of the role of Brinkman number in microchannels using local parameters”, Int. J. Heat Mass Transfer., vol. 42 pp 1837–1849, 1999.

[73] K. . Toh, X. . Chen, and J. . Chai, “Numerical computation of fluid flow and heat transfer in microchannels,” Int. J. Heat Mass Transf., vol. 45, no. 26, pp. 5133–5141, 2002.

[74] J. T. Liu, X. F. Peng, and B. X. Wang, “Variable-property effect on liquid flow and heat transfer in microchannels,” Chem. Eng. J., vol. 141, no. 1–3, pp. 346–353, 2008.

[75] Z. Li, X. Huai, Y. Tao, and H. Chen, “Effects of thermal property variations on the liquid flow and heat transfer in microchannel heat sinks,” Appl. Therm. Eng., vol. 27, no. 17–18, pp. 2803–2814, 2007.

[76] G. L. Morini, “Viscous heating in liquid flows in micro-channels,” Int. J. Heat Mass Transf., vol. 48, no. 17, pp. 3637–3647, 2005.

[77] D. Liu and S. V. Garimella, “Analysis and optimization of the thermal performance of microchannel heat sinks,” Int. J. Numer. Methods Heat Fluid Flow, vol. 15, no. 1, pp. 7–26, 2005.

[78] S. J. KIM, “Methods for Thermal Optimization of Microchannel Heat Sinks,” Heat Transf. Eng., vol. 25, no. 1, pp. 37–49, 2004.

[79] Khan, W.A., Yovanovich, M.M., & Culham, J.R., “Optimization of microchannel heat sinks using entropy generation minimization method”, Twenty-Second Annual IEEE Semiconductor Thermal Measurement And Management Symposium, 78-86, 2006.

[80] T. Bello-Ochende, J. P. Meyer, and F. U. Ighalo, “Combined Numerical Optimization and Constructal Theory for the Design of Microchannel Heat Sinks,” Numer. Heat Transf. Part A Appl., vol. 58, no. 11, pp. 882–899, 2010.

[81] G. Xie, Y. Liu, B. Sunden, and W. Zhang, “Computational Study and Optimization of Laminar Heat Transfer and Pressure Loss of Double-Layer Microchannels for Chip Liquid Cooling,” J. Therm. Sci. Eng. Appl., vol. 5, no. 1, p. 011004, 2013.

[82] G. M. Normah, J. T. Oh, B. C. Nguyen, K. Il Choi, and A. Robiah, “Comparison of the optimized thermal performance of square and circular ammonia-cooled microchannel heat sink with genetic algorithm,” Energy Convers. Manag., vol. 102, pp. 59–65, 2015.

[83] M. Rahimi-Gorji, O. Pourmehran, M. Hatami, and D. D. Ganji, “Statistical optimization of microchannel heat sink (MCHS) geometry cooled by different nanofluids using RSM analysis,” Eur. Phys. J. Plus, vol. 130, no. 2, pp. 1–21, 2015.

[84] S. R. Reddy, A. Abdoli, G. S. Dulikravich, C. C. Pacheco, G. Vasquez, R. Jha, M. J. Colaco, and H. R. B. Orlande, “Multi-Objective Optimization of Micro Pin-Fin Arrays for Cooling of High Heat Flux Electronics with a Hot Spot,” Heat Transf. Eng., vol. 38, no. 14–15, pp. 1–12, 2016.

[85] Yaser Hadad, Bharath Ramakrishnan, Reza Pejman, Srikanth Rangarajan, Paul R. Chiarot, Arvind Pattamatta, Bahgat Sammakia, “Three-objective shape optimization and parametric study of a micro-channel heat sink with discrete non-uniform heat flux boundary conditions”,Applied Thermal Engineering, Volume 150, 2019, Pages 720-737

[86] Yogesh K. Prajapati, “Influence of fin height on heat transfer and fluid flow characteristics of rectangular microchannel heat sink”, International Journal of Heat and Mass Transfer, Volume 137, 2019, Pages 1041-1052

[87] Nor Haziq Naqiuddin, Lip Huat Saw, Ming Chian Yew, Farazila Yusof, Hiew Mun Poon, Zuansi Cai, Hui San Thiam, “Numerical investigation for optimizing segmented micro-channel heat sink by Taguchi-Grey method”, Applied Energy, Volume 222, 2018, Pages 437-450

[88] Connor B. Dokken, Brian M. Fronk, “Optimization of 3D printed liquid cooled heat sink designs using a micro-genetic algorithm with bit array representation”, Applied Thermal Engineering, Volume 143, 2018, Pages 316-325

[89] Yunfei Yan, Hongyu Yan, Siyou Yin, Li Zhang, Lixian Li, “Single/multi-objective optimizations on hydraulic and thermal management in micro-channel heat sink with bionic Y-shaped fractal network by genetic algorithm coupled with numerical simulation”, International Journal of Heat and Mass Transfer,Volume 129, 2019, Pages 468-479

[90] Xiaojun Shi, Shan Li, Yingjie Mu, Bangtao Yin, “Geometry parameters optimization for a microchannel heat sink with secondary flow channel”, International Communications in Heat and Mass Transfer, Volume 104, 2019, Pages 89-100

[91] Hui Tan, Longwen Wu, Mingyang Wang, Zihao Yang, Pingan Du, “Heat transfer improvement in microchannel heat sink by topology design and optimization for high heat flux chip cooling”, International Journal of Heat and Mass Transfer, Volume 129, 2019, Pages 681-689

[92] D.D. Ma, G.D. Xia, W. Wang, Y.T. Jia, Y.C. Yang, “Study on thermal performance of microchannel heat sinks with periodic jetting and throttling structures in sidewalls”, Applied Thermal Engineering, Volume 158, 2019

[93] Y. Wang and Y. Peles, “An Experimental Study of Passive and Active Heat Transfer Enhancement in Microchannels,” J. Heat Transfer, vol. 136, no. 3, p. 031901, 2013.

[94] Star CCM+® Theory Guide

[95] C. H. K. Williamson and G. L. Brown, “A Series in 1/sqrt(Re) to Represent the Strouhal - Reynolds Number Relationship of the Cylinder Wake,” J. Fluids Struct., vol. 12, pp. 1073–1085, 1998

[96] P.J.Roache, “Perspective: A Method For Uniform Reporting of Grid Refinement Studies”, Journals of Fluids Engineering, , Vol. 116/405, September 1994.

[97] Kiran K. Ambatipudi, Muhammad M. Ra, “Analysis of Conjugate Heat Transfer in Microchannel Heat Sinks,” Numerical Heat Transf. Appl., vol. 37, no. 7, pp. 711–731, 2000.

[98] L. He and M. L. G. Oldfield, “Unsteady Conjugate Heat Transfer Modeling,” J. Turbomach., vol. 133, no. 3, p. 031022, 2011.

[99] Parahovnik A, Wang Y, Peles Y. “Transient Local Resolution of Flow Boiling in a Microchannel With a Streamlined Pin Fin” ASME. International Conference on Nanochannels, Microchannels, and Minichannels, ASME 2018 16th International Conference on Nanochannels, Microchannels, and Minichannels

[100] A. Kopanidis, A. Theodorakakos, E. Gavaises, D. Bouris, “3D numerical simulation of flow and conjugate heat transfer through a pore scale model of high porosity open cell metal foam”, International Journal of Heat and Mass Transfer,Volume 3, Issues 11–12

[101] Corey Woodcock, Chisela Ng'oma, Michael Sweet, Yingying Wang, Yoav Peles, Joel Plawsky, “Ultra-high heat flux dissipation with Piranha Pin Fins”, International Journal of Heat and Mass Transfer, Volume 128, 2019

[102] Kays, W.M, M. E. Crawford and B. wiegand, “Convective Heat and Mass Transfer”, 4th edition, McGraw-Hill Higher Education, Boston, 2005

[103] Iman, R. & M. Shortencarier 1984, “A FORTRAN 77 program and user's guide for the generation of Latin Hypercube and random samples for use with computers models”, NUREG/CR-3624, U.S. Nuclear Regulatory Commission.

[104] McKay M., Beckman, R., Conover, W. A, “Comparison of Three Methods for Selecting Values of Input Variables in the Analysis of Output from a Computer Code”, Technometrics, vol 21, no. 2, May 1979.

[105] DAKOTA User’s Guide